Natural convective flow between isothermal concentric spheres
by Shiu-hau Yin

A dissertation submitted to the Graduate Faculty in partial fulfillment of the requirements for the degree of DOCTOR OF PHILOSOPHY in Aerospace and Mechanical Engineering
Montana State University
© Copyright by Shiu-hau Yin (1972)

Abstract:
Natural convective flow of air and water between isothermal concentric spheres was experimentally investigated. Different visualization techniques were utilized for each specified fluid. A special visualization technique was developed for water as the working medium in this study. The visualization of the flow pattern was accomplished by introducing a well mixed and prepared solution of distilled water containing a very minute amount of liquid "Ajax" detergent into the annulus and transversely illuminating vertical diameter.

For air in the gap, smoke was introduced. A qualitative description of the flow patterns obtained for each spherical combination studied is presented, and these descriptions are supplemented by photographs of the flow. Motion pictures of each distinctive type of flow pattern found to occur in this investigation were also obtained.

For air as the working fluid, distinct steady and unsteady patterns were obtained for various diameter ratios ranging from 1.40 to 2.17 and for Grashof numbers (based on gap thickness) ranging from 7.0 x 103 to 1.2 x 106. The flow patterns at the lower Grashof numbers qualitatively agree with those obtained in previous studies. The inception of instabilities characterized by periodic interior contractions or three-dimensional spiral flow in the spherical annuli was compared to the case of horizontal cylindrical annuli.

For water as working fluid, the most common basic flow pattern, the steady dog-face type, occured in the three largest diameter ratios investigated. This kind of flow pattern has never been observed before, but it does correlate quite well with the temperature profiles obtained in the heat transfer study. A formation of tertiary flow in the weak shear layer between two secondary cells occurred for the diameter ratio of 1.78 (L/Di=0.39) at high Grashof numbers. As the Grashof number was increased above certain transition points, an unsteady dog—face type flow, or a three-dimensional spiral flow, was observed. In this study, the diameter ratio ranged from 1.09 to 2.17 and the Grashof number based on gap thickness ranged from 1.7 x IO^3 to 1.4 x 10^7.

A tabular form of the experimental results for each test fluid is presented to provide categorization of the fluid-flow behavior within the available ranges of independent variables.

NATURAL CONVECTIVE FLOW BETWEEN ISOTHERMAL CONCENTRIC SPHERES

by

SHIU-HAU YIN

A dissertation submitted to the Graduate Faculty
in partial fulfillment of the requirements for the degree

of

DOCTOR OF PHILOSOPHY

in

Aerospace and Mechanical Engineering

Approved:

F M Bishop
Head, Major Department

J A B
Chairman, Examining Committee

Henry L. Parsons
Graduate Dean

MONTANA STATE UNIVERSITY
Bozeman, Montana

March, 1972

ACKNOWLEDGEMENT

The author wishes to express his sincere thanks and appreciation to all those who have aided in this work. Special thanks are due to Dr. J. A. Scanlan, Dr. E. H. Bishop, and Dr. R. E. Powe for their advice, guidance, and encouragement. Thanks also go to Mr. Gordon Williamson for his assistance in constructing the entire apparatus. The writer is especially appreciative of the patience and understanding of his wife, Sandra.

The work reported in this thesis was supported by the Atomic Energy Commission under Contract Number AT(45-1)-2214.

TABLE OF CONTENTS

Chapter	Page
VITA	ii
ACKNOWLEDGEMENT	iii
LIST OF TABLES	v
LIST OF FIGURES	vi
ABSTRACT	x
NOMENCLATURE	xi
I. INTRODUCTION	1
II. LITERATURE REVIEW	4
III. EXPERIMENTAL SYSTEM	17
APPARATUS	17
PROCEDURE	34
IV. EXPERIMENTAL RESULTS AND DISCUSSION	39
FLOW PATTERN DESCRIPTIONS	41
SUMMARY OF EXPERIMENTAL RESULTS	86
DISCUSSION OF RESULTS	94
V. CONCLUSIONS AND RECOMMENDATIONS	103
APPENDIX I. GOVERNING DIFFERENTIAL EQUATIONS	107
APPENDIX II. EQUIPMENT LIST	112
APPENDIX III. COMPUTER PROGRAMS	115
BIBLIOGRAPHY	126

LIST OF TABLES

Table		Page
1.	Gap Working Fluid and Associated Geometric Combinations	38
2.	Summary of Results for Air as the Gap Working Fluid	89
3.	Summary of Results for Water as the Gap Working Fluid	92

LIST OF FIGURES

Figure		Page
1.	Assembled Apparatus with Water Cooling System	18
2.	Schematic Diagram of Experimental System (Water as Gap Fluid)	19
3.	Schematic Diagram of Experimental System (Air as Gap Fluid)	20
4.	Interior of Inner Sphere	22
5.	Glass Hemispheres	24
6.	Installation of Inner Sphere Inside the Glass Sphere	25
7.	Particles in Water within the Spherical Annulus before Heating	31
8.	Steady Crescent Eddy Pattern for $D_o/D_i = 2.17$, $L/D_i = 0.59$, $N_{GR_L} = 72{,}000$, $N_{RA_L} = 51{,}000$	42
9.	Photograph Showing Onset of Steady Kidney-Shaped Eddy Pattern for $D_o/D_i = 2.17$, $L/D_i = 0.59$, $N_{GR_L} = 166{,}500$, $N_{RA_L} = 118{,}000$	44
10.	Steady Kidney-Shaped Eddy Pattern for $D_o/D_i = 2.17$ $L/D_i = 0.59$, $N_{GR_L} = 295{,}800$, $N_{RA_L} = 209{,}600$	45
11.	Steady Kidney-Shaped Eddy Pattern for $D_o/D_i = 2.17$, $L/D_i = 0.59$, $N_{GR_L} = 555{,}000$, $N_{RA_L} = 393{,}000$	47
12.	Steady Modified Kidney-Shaped Eddy Pattern for $D_o/D_i = 2.17$, $L/D_i = 0.59$, $N_{GR_L} = 1{,}056{,}000$, $N_{RA_L} = 746{,}000$	48
13.	Steady Crescent Eddy Pattern for $D_o/D_i = 1.78$, $L/D_i = 0.39$, $N_{GR_L} = 93{,}100$, $N_{RA_L} = 66{,}000$	50

Figure Page

14. Steady Kidney-Shaped Eddy Pattern for $D_o/D_i = 1.78$, $L/D_i = 0.39$, $N_{GR_L} = 194{,}000$, $N_{RA_L} = 137{,}400$ 51

15. Photograph of Flow Pattern for $D_o/D_i = 1.78$, $L/D_i = 0.39$, $N_{GR_L} = 246{,}700$, $N_{RA_L} = 174{,}600$ 53

16. Photograph of Flow Pattern for $D_o/D_i = 1.78$, $L/D_i = 0.39$, $N_{GR_L} = 275{,}000$, $N_{RA_L} = 194{,}600$ 54

17. Periodic Interior Contraction Flow for $D_o/D_i = 1.78$, $L/D_i = 0.39$, $N_{GR_L} = 323{,}000$, $N_{RA_L} = 228{,}400$ 55

18. Sketch of Flow Pattern for $D_o/D_i = 1.40$, $L/D_i = 0.20$, $N_{GR_L} = 8{,}400$, $N_{RA_L} = 5{,}950$ 57

19. Photograph of Flow Pattern for $D_o/D_i = 1.40$, $L/D_i = 0.20$, $N_{GR_L} = 8{,}400$, $N_{RA_L} = 5{,}950$ 58

20. Steady Crescent Eddy Pattern for $D_o/D_i = 1.40$, $L/D_i = 0.20$ $N_{GR_L} = 25{,}000$, $N_{RA_L} = 17{,}700$ 59

21. Photograph of Flow Pattern for $D_o/D_i = 1.40$, $L/D_i = 0.20$, $N_{GR_L} = 99{,}300$, $N_{RA_L} = 70{,}000$ 61

22. Photograph Showing Counter Rotating Cells in Upper Region of Annulus for $D_o/D_i = 1.40$, $L/D_i = 0.20$, $N_{GR_L} = 103{,}800$, $N_{RA_L} = 73{,}200$ 63

23. Photograph Showing Counter Rotating Cells in Upper Region of Annulus for $D_o/D_i = 1.40$, $L/D_i = 0.20$, $N_{GR_L} = 103{,}800$, $N_{RA_L} = 73{,}200$ 64

24. Three-Dimensional Spiral Motion in Upper Gap Region for $D_o/D_i = 1.40$, $L/D_i = 0.20$, $N_{GR_L} = 103{,}800$, $N_{RA_L} = 73{,}200$ 65

Figure Page

25. Sketch of Steady Dog-Face Pattern for D_o/D_i = 2.17, L/D_i = 0.59, N_{GR_L} = 248,800, N_{RA_L} = 2,812,000 67

26. Steady Dog-Face Pattern for D_o/D_i = 2.17, L/D_i = 0.59, N_{GR_L} = 248,800, N_{RA_L} = 2,812,000 68

27. Steady Dog-Face Pattern (Upper Portion) for D_o/D_i = 2.17, L/D_i = 0.59, N_{GR_L} = 248,800, N_{RA_L} = 2,812,000 . 69

28. Photograph of Flow Pattern for D_o/D_i = 2.17, L/D_i = 0.59, N_{GR_L} = 1,345,000, N_{RA_L} = 12,554,000 71

29. Steady Dog-Face Pattern for D_o/D_i = 1.78, L/D_i = 0.39, N_{GR_L} = 404,000, N_{RA_L} = 3,992,000 73

30. Sketch of Tertiary Flow Pattern for D_o/D_i = 1.78, L/D_i = 0.39, N_{GR_L} = 1,688,000, N_{RA_L} = 14,170,000 75

31. Tertiary Flow Pattern (Upper Portion) for D_o/D_i = 1.78, L/D_i = 0.39, N_{GR_L} = 1,688,000, N_{RA_L} = 14,170,000 . . . 76

32. Tertiary Flow Pattern (Upper Portion) for D_o/D_i = 1.78, L/D_i = 0.39, N_{GR_L} = 1,688,000, N_{RA_L} = 14,170,000 77

33. Steady Dog-Face Pattern (Upper Portion) for D_o/D_i = 1.40, L/D_i = 0.20, N_{GR_L} = 117,000, N_{RA_L} = 1,115,000 78

34. Photograph of Flow Pattern (Upper Portion) for D_o/D_i = 1.40, L/D_i = 0.20, N_{GR_L} = 1,224,000, N_{RA_L} = 8,322,000 80

35. Three-Dimensional Spiral Motion in Upper Gap Region for D_o/D_i = 1.40, L/D_i = 0.20, N_{GR_L} = 2,497,000, N_{RA_L} = 14,946,000 82

Figure Page

36. Photograph of Flow Pattern (Upper Portion) for D_o/D_i = 1.09, L/D_i = 0.04, N_{GR_L} = 1,840, N_{RA_L} = 18,300 . . . 84

37. Photograph of Flow Pattern (Lower Portion) for D_o/D_i = 1.09, L/D_i = 0.04, N_{GR_L} = 1,840, N_{RA_L} = 18,300 . . . 85

38. Temperature Profiles for Water, D_o/D_i = 1.40, L/D_i = 0.20, N_{GR_L} = 1,217,000, N_{RA_L} = 7,923,000 99

39. Sketch of Steady Dog-Face Pattern for D_o/D_i = 1.40, L/D_i = 0.20, N_{GR_L} = 1,217,000, N_{RA_L} = 7,923,000 . . . 100

ABSTRACT

Natural convective flow of air and water between isothermal concentric spheres was experimentally investigated. Different visualization techniques were utilized for each specified fluid. A special visualization technique was developed for water as the working medium in this study. The visualization of the flow pattern was accomplished by introducing a well mixed and prepared solution of distilled water containing a very minute amount of liquid "Ajax" detergent into the annulus and transversely illuminating vertical diameter. For air in the gap, smoke was introduced. A qualitative description of the flow patterns obtained for each spherical combination studied is presented, and these descriptions are supplemented by photographs of the flow. Motion pictures of each distinctive type of flow pattern found to occur in this investigation were also obtained.

For air as the working fluid, distinct steady and unsteady patterns were obtained for various diameter ratios ranging from 1.40 to 2.17 and for Grashof numbers (based on gap thickness) ranging from 7.0×10^3 to 1.2×10^6. The flow patterns at the lower Grashof numbers qualitatively agree with those obtained in previous studies. The inception of instabilities characterized by periodic interior contractions or three-dimensional spiral flow in the spherical annuli was compared to the case of horizontal cylindrical annuli.

For water as working fluid, the most common basic flow pattern, the steady dog-face type, occured in the three largest diameter ratios investigated. This kind of flow pattern has never been observed before, but it does correlate quite well with the temperature profiles obtained in the heat transfer study. A formation of tertiary flow in the weak shear layer between two secondary cells occurred for the diameter ratio of 1.78 (L/D_i=0.39) at high Grashof numbers. As the Grashof number was increased above certain transition points, an unsteady dog-face type flow, or a three-dimensional spiral flow, was observed. In this study, the diameter ratio ranged from 1.09 to 2.17 and the Grashof number based on gap thickness ranged from 1.7×10^3 to 1.4×10^7.

A tabular form of the experimental results for each test fluid is presented to provide categorization of the fluid-flow behavior within the available ranges of independent variables.

NOMENCLATURE

Symbol	Description
a, b	Characteristic physical dimensions
C_p	Fluid specific heat at constant pressure
D	Diameter
g	Acceleration of gravity, 32.174 ft/sec^2
H	Height of vertical plate
k	Fluid thermal conductivity
L	Distance between plates; gap thickness (difference between outer and inner spherical radii)
N_D	Characteristic physical dimension ratio
N_{GR_a}	Grashof number, $\rho^2 g\beta(T_i - T_o)a^3/\mu^2$, a is replaced by any desired characteristic dimension
N_{PR}	Prandtl number, $C_p\mu/k$
N_{RA_a}	Rayleigh number, $\rho^2 g\beta(T_i - T_o)a^3 C_p/\mu k$
r	Radial coordinate
r_{avg}	Average radius, $r_{avg} = (r_i + r_o)/2$
T	Temperature
ΔT	Temperature difference between inner and outer spheres, $T_i - T_o$
α	Thermal Diffusivity, $k/\rho C_p$
β	Thermal expansion coefficient
ϕ	Angular coordinate measured from upward vertical axis

Symbol	Description
μ	Dynamic viscosity of the fluid
ρ	Fluid density

Subscripts

am	Arithmetic mean
i	Refers to inner sphere
L	Based on distance between plates or gap thickness
o	Refers to outer sphere
vm	Volume weighted mean

CHAPTER I

INTRODUCTION

In recent years, a considerable amount of interest has developed in the subject of natural convection from a body to its finite enclosure. This particular heat transfer and fluid mechanics problem is becoming increasingly important in certain areas such as nuclear design, aircraft cabin design, and electronic instrumentation packaging. However, only relatively little information has been reported in this area.

Since 1964, an important beginning in this broad area has been made in the study of natural convection between concentric isothermal spheres. The first investigation, using air as the gap fluid, was carried out by Bishop, Kolflat, Mack, and Scanlan [1]. Utilizing the techniques reported in [2], they described the flow patterns observed visually and photographically. Heat transfer data, temperature distributions, and additional comments on the flow patterns were presented by Bishop et al [3]. An analytical prediction of both thermal and flow fields by Mack and Hardee [4] is valid only for low Rayleigh numbers. The most recent studies are those of Scanlan, Bishop, and Powe [5], and Weber, Powe, Bishop, and Scanlan [6]. They extended the existing heat transfer data and temperature distributions of Bishop et al [3] ($N_{PR} \sim 0.7$) to include Prandtl numbers up to 4184 by using water and two silicone fluids as

working media for both concentric and vertically eccentric cases.

Unfortunately, most of these previous studies are restricted to the heat transfer rates and temperature fields; there is little information available concerning the flow field of this specific geometrical configuration. In order to fully understand the convection process, both thermal and flow phenomena must be known. Therefore, the purpose of the current investigation is to attempt to alleviate the problem of the serious lack of knowledge of the flow behavior in this particular geometry. The attempts made in this current study are to extend the existing data of Bishop et al [1] to a higher impressed temperature difference with air as the working fluid and to establish further study of this configuration with water as the gap fluid.

The flow process resulting from the density change caused by a temperature gradient within the gravitational force field between concentric isothermal spheres can be represented by a mathematical model which includes a set of simultaneous, non-linear, coupled, partial differential equations subject to the associated boundary conditions. The analytic treatment of this problem is very difficult. This is due to the following reasons: (1) the non-linearity of the governing equations, (2) the invalidity of the general boundary layer approximations in this case, and (3) the lack of information of boundary conditions, especially when the flow field is not steady and

therefore not necessarily symmetrical about a vertical axis through the center of the spheres. These equations are shown in Appendix I.

The purposes of the present experimental investigation concerning the flow phenomena between concentric isothermal spheres are:

(1) To obtain criteria for predicting the fluid-flow behavior within the gap as the radial distance and the temperature difference between spheres are varied. Both air and water are used as the enclosed fluids. These criteria will allow prediction of the type of flow which will occur under a variety of conditions.

(2) To study the mechanism which determines when and how the onset of instability in the flow field occurs.

Furthermore, the results of this present work should contribute to a greater understanding of the natural convection process between isothermal spheres by correlating these with the existing data concerning heat transfer rates and temperature profiles. Also, the information described in this dissertation may be used as a guide to validate future analytical and numerical studies of natural convective flows in this spherical geometry.

CHAPTER II

LITERATURE REVIEW

Natural convection from a surface to its infinite surroundings has been studied by a number of investigators, and a rather large number of papers are available in the literature on this subject. The more recent contributions have been made relative to natural convection within enclosed spaces. However, there is still only a limited amount of information available concerning natural convective flow phenomena within confined spaces.

Good reviews of the early work concerned with the natural convection process can be found in several textbooks such as Jakob [7], Eckert and Drake [8], and Gröber, Erk, and Grigull [9]. Two things are generally agreed upon in the literature on natural convection. One is that the natural convection process is dominated by both fluid-flow and heat transfer considerations. Second is that the natural convection process within confined spaces, defined by two characteristic dimensions, can be characterized by the following dimensionless parameters:

$$N_{GR_a} = \frac{\rho^2 g\, \beta \Delta T a^3}{\mu^2} \tag{2-1}$$

$$N_{PR} = \frac{Cp\, \mu}{k} \tag{2-2}$$

and

$$N_D = \frac{a}{b} \tag{2-3}$$

(Actually there are two more parameters, $\frac{g\beta a}{Cp}$ and $\beta\Delta T$, but these usually are not needed.) In these equations "a" and "b" are characteristic dimensions, ΔT is a suitably defined temperature difference, N_{GR_a} is the Grashof number based on dimension "a", N_{PR} is the Prandtl number, and N_D is a dimensionless ratio of the characteristic dimensions. All the fluid properties are normally evaluated at either an arithmetic mean temperature or a volume-weighted mean temperature. An additional dimensionless group, the Rayleigh number (N_{RA_a}), has been found convenient in certain cases to replace the Grashof number. The Rayleigh number is the product of the Prandtl and Grashof numbers:

$$N_{RA_a} = N_{PR} \cdot N_{GR_a} = \frac{\rho g \beta \Delta T a^3}{\alpha \mu} \qquad (2\text{-}4)$$

In the present review, specific attention is directed toward natural convective flows between a body and its finite enclosure. For the case with small gap thickness and large radius of curvature, the spherical geometry can be approximated by a plane wall enclosure. Therefore a short review of the literature in this area is also presented for completeness. For clarity, the discussion is presented in three separated parts based on different geometrical configurations. These are (1) parallel plates and rectangular enclosures, (2) concentric cylindrical annuli, and (3) spherical annuli.

PARALLEL PLATES AND RECTANGULAR ENCLOSURES

Usually no convective motion occurs in a fluid which is enclosed between two parallel horizontal plates with the upper plate maintained at a higher temperature than the lower. In a normal fluid for which the density decreases with temperature, such a temperature field will yield a stable situation in which the less dense layers are located above the denser fluid. Heat is transferred from the upper plate to the lower plate by conduction, and a linear temperature distribution is expected. However, when the lower plate is at the higher temperature, resulting in the less dense layer at the bottom, an unstable situation will be produced. Nevertheless, there is no convective flow before the critical Rayleigh number of 1,705 (based on the gap thickness) is reached. Upon exceeding this value the flow field will be a cellular structure with more or less regular hexagonal cells, in which the flow moves upward in the center and returns downward near the sides or vice versa depending upon the properties of the fluid. This flow situation is maintained up to a Rayleigh number of around 45,000. Above this value of Rayleigh number the flow changes to irregular turbulent. Chandra [10] found that the value of the critical Rayleigh number changes depending upon the layer thickness. It was reported by Schmidt and Saunders [11] that the length of the horizontal side of a cell was twice the layer depth. The more recent

work is that of Leontiev and Kirdyashkin [12]. They did an experimental study of flow patterns and temperature fields with 96% ethyl alcohol as the test liquid. To visualize the flow, well-wettable aluminum particles 5-20 microns in size were placed in the alcohol. They reported that polygonal structure of the flow in a horizontal layer was observed for Rayleigh numbers $N_{RA_L} < 95{,}000$. The flow in a polygonal cell is laminar with a motion of radial flow from the bounding sides of the polygon to the center. At $N_{RA_L} \sim 10^5$, the polygonal structure of the liquid flow ceases completely and transforms into a roller structure.

Natural convection across a closed cavity between vertical boundaries at different temperatures was studied by Batchelor [13]. He investigated this problem in three cases; (1) small Rayleigh numbers ($N_{RA_L} < 10^3$) with H/L (ratio of cavity height to width) approximately unity, (2) general Rayleigh numbers with large H/L's, (3) large Rayleigh numbers with general H/L's. An analytical solution for the first case was found by utilizing a method of expanding the stream function and temperature in power series in terms of the Rayleigh number. He also obtained the solution for the last two cases by making drastic idealizations. He predicted transition to turbulent flow at $N_{RA_L} = 13{,}700$ for air in the second case, and at $N_{GR_L} = 10^9 (H/L)^{-3}$ for air (perhaps for other fluids also) in the last

case.

Using the same configuration, both experimental and numerical investigations were performed by Elder [14, 15]. The flow was made visible in his experimental study by using aluminum powder suspended in the fluid. The velocity measurements were made either by direct observation or from time photographs, in which the streak-length is proportional to the velocity. A steady secondary flow was observed in the interior region of the flow for $N_{RA_L} \sim 10^5$. Further, it was found that the secondary flows, when of sufficient amplitude, were able to generate other steady flows, called tertiary flows. Both photographs and sketches of the flow patterns were presented for various gap widths and Rayleigh numbers. In addition, the velocity profiles were also plotted for the half height along the gap at various Rayleigh numbers. His numerical solution was checked with the thermal and flow field data of Eckert and Carlson [16], and this comparison did show that both results are comparable.

Wilkes and Churchill [17] applied numerical techniques to a long rectangular channel with air as the enclosed fluid. The streamlines were obtained for Grashof numbers up to 10^5 and for various height-to-width ratios.

CONCENTRIC CYLINDRICAL ANNULI

Another geometry which appears to yield flow results applicable to the study of concentric spheres is concentric cylindrical annuli. Several investigations using this configuration in natural convection have been carried out experimentally, analytically, and numerically. These studies cover a wide range of diameter ratios, Grashof numbers, and various gap fluids.

Liu, Mueller, and Landis [18] carried out an experimental study utilizing air, water, and Dow silicone fluid No. 200 as the working media. Five sets of concentric tubes, having diameter ratios (D_o/D_i) ranging from 1.154 to 7.500, were used in their study. Different observation techniques were used for various working fluids in the gap. For air, tobacco smoke was introduced into the gap; in water, a blue-dye-water mixture was slowly injected under isothermal conditions. A small quantity of neutrally buoyant polyethylene particles added to the silicone fluid permitted visual and photographic observations. General descriptions and sketches of the flow patterns which were observed were presented.

A numerical solution to the problem of natural convective flow, with air as the medium, in cylindrical annuli was also reported in the form of plots of the stream function for the range of $2 \leq D_o/D_i \leq 57$ and $1 \leq N_{GR_{D_i}} \leq 10^5$ by Crawford and Lemlich [19]. Their results

are in accordance with the appropriate qualitative flow patterns obtained experimentally by Liu et al [18] at a diameter ratio D_o/D_i = 2.0.

Grigull and Hauf [20] presented numerous photographs, taken by introducing smoke to make the flow visible in a normal incident light plane, and sketches of flows. The annulus was filled with air at atmospheric pressure. Various gap width-to-inner diameter ratios ($0.15 \leq L/D_i \leq 2.65$) were selected in their study. Three different types of convective flow phenomena as the Grashof number was changed were postulated. These are (1) a two dimensional pseudo-conductive regime for $N_{GR_L} < 24{,}000$, (2) a regime of transition with a three dimensional convective motion for $24{,}000 \leq N_{GR_L} \leq 30{,}000$, and (3) a regime of fully developed two dimensional laminar convective motion for $30{,}000 \leq N_{GR_L} \leq 716{,}000$.

An experimental investigation of the flow behavior for natural convection in simple and obstructed horizontal cylindrical annuli was performed by Lis [21] using the Schlieren technique. A few photographs and verbal descriptions of the flow patterns were presented in his report for various diameter ratios and Grashof numbers.

Bishop and Carley [22] carried out a photographic experimental study of natural convective flows of air between concentric horizontal cylinders. Photographs and qualitative descriptions of

the flow patterns were obtained for various operating conditions at diameter ratios ranging from 1.23 to 3.69, with temperature differences of 5°F to 100°F between the cylinders. They found two types of stable flow and one unstable flow within their range of diameter ratios. Under all temperature differences studied for diameter ratios of 1.23, 1.85, and 2.46, the first stable flow, termed a "crescent eddy" type, existed at low Grashof numbers. Another stable flow pattern, the "kidney-shaped eddy" type, was found to appear for a diameter ratio 3.69 at Grashof numbers above that at which the crescent eddy flow pattern disappeared. For higher Grashof numbers, this pattern became an unstable oscillation of the fluid in the upper region of the gap. They also found that both frequency and amplitude of oscillation were increased at increasing temperature difference.

Employing the technique set forth by Batchelor [13] to expand the stream function and temperature in an infinite series of Rayleigh number, an analytic solution, limited to low values of Rayleigh number, was reported by Mack and Bishop [23]. They found that increasing the Prandtl number above 0.70 had very little effect upon the qualitative appearance of the stream lines at low Rayleigh number, except for very small Prandtl number fluids such as liquid metals.

An extensive study of the three dimensional oscillatory flow in cylindrical annuli, observed by Bishop and Carley [22], was carried

out by Bishop, Carley, and Powe [24]. Correlation equations were given to allow estimation of the inception of this oscillatory flow and its subsequent amplitude, period, and wave length. Detailed descriptions of this particular flow phenomenon supported by photography and motion pictures also can be found in Powe [27].

Bishop and Carley [22] compared their results with these of Liu et al [18] and pointed out the very interesting possibility of obtaining different types of flows for a given diameter ratio while using different cylinder sizes. Powe [27] investigated this possibility experimentally for air within the gap as reported by Powe, Carley, and Bishop [25]. Using six different cylinder sets, two of them yielding the same diameter ratio with different cylinder sizes, and varying both the annulus pressure and temperature difference between the cylinder surfaces, they observed one steady and three unsteady flow patterns in the range of Grashof number (based on annulus width) from 300 to 3.4×10^6. They pointed out that radius of curvature, though not affecting the general type of the flow pattern, did affect the specific value of Grashof number at which transition from a steady to an unsteady pattern occurred. A plot categorizing the flow patterns in horizontal concentric cylindrical annuli filled with air was presented showing the transition Grashof number versus ratio of inner-cylinder diameter-to-annulus width by combining their data and several existing previous

experimental results.

The results of a numerical investigation, utilizing finite-difference techniques, to this problem were presented by Powe, Carley, and Carruth [26]. The results were compared with the existing data and excellent agreement was found. This numerical solution can also be used to predict the Rayleigh numbers where the flow will go from a stable condition to an unstable condition for a wide range of inverse relative gap widths (D_i/L) from 2.8 to 12.5. This is due to the occurence of steady secondary flows immediately preceding the unsteady flow, which has been observed in experimental investigations within the above specified inverse relative gap widths. It was found that a pronounced increase in magnitude of temperature and velocity components heralded the appearance of secondary flow in the large inverse relative gap widths.

SPHERICAL ANNULI

An initial investigation of the natural convection process in the annulus between concentric spheres was carried out by Bishop, Scanlan, and their colleagues in 1964. Since that time a series of papers have been published.

The first investigation was carried out by Bishop, Kolflat, Mack, and Scanlan [1] for air as the working medium within the gap. Using

the flow visualization techniques described in [2], they observed three different flow behaviors for diameter ratios of 1.19, 1.72, and 3.14 at various temperature differences ($5°F \leq \Delta T \leq 60°F$). The most common pattern, the crescent-eddy type, occurred for the intermediate diameter ratio (1.72) at all temperature differences, while for the largest (3.14) and the smallest (1.19) diameter ratios it occurred only at small temperature differences. The second flow pattern, the kidney-shaped eddy type, occurred for the largest diameter ratio (3.14), i.e., the largest gap, at moderate to large temperature differences. The main difference between the first two patterns was the shape of the central-eddy region. The third flow pattern, the "falling-vortices" type, occurred at moderate to high temperature differences for the smallest diameter ratio (1.19). This flow type was unsteady and was characterized by the formation and shedding of vortex cells. Detailed descriptions and photographs concerning these three different flow patterns were also presented. Further details of this study were given by Bishop [28]. The results of an investigation of heat transfer rates and a detailed discussion of temperature distributions correlated to the observed flow patterns were presented by Bishop *et al* [3].

An analytical solution to this problem was carried out by Mack and Hardee [4] in the same manner as that of Mack and Bishop [23] for concentric cylinders. This solution is limited to low values of

Rayleigh number. Their highest value of Rayleigh number was considerably below the lowest value obtained experimentally by Bishop et al [3].

The two most recent reports were contributed by Scanlan, Bishop, and Powe [5] and Weber, Powe, Bishop, and Scanlan [6]. Scanlan et al [5] extended the existing heat transfer data and temperature profiles of Bishop et al [3] ($N_{PR} \sim 0.70$) to include Prandtl numbers up to 4184 by introducing water and two different silicone fluids into the gap. The first investigation concerning natural convection between eccentric spheres was performed by Weber et al [6]. They introduced a conformal mapping technique to present the results of heat transfer rates between eccentric spheres to enable a comparison with the existing data for concentric spheres. A single correlation equation of heat transfer rates was obtained for an extremely wide range of diameter ratios, eccentricities, Rayleigh numbers, and Prandtl numbers. They also pointed out that the effect of a negative eccentricity (inner sphere below the center of the outer sphere) on the temperature distribution was basically an enhancement of the convective motion, while a positive eccentricity tended to stabilize the flow field and promote conduction rather than convection. The multicellular flow pattern, which has previously been postulated by Bishop et al [3] to explain the temperature distribution between concentric spheres with small gap spacing, was

also found to yield a plausible explanation for the thermal field obtained using the largest inner sphere (D_i = 9") considered in their investigation.

In addition, natural convection heat transfer between isothermal centrally located vertical cylinders and their isothermal spherical enclosure was experimentally investigated by Weber [29]. Various diameters of cylinders and aspect ratios, defined as the ratio of length of straight cylindrical section to radius of cylinder, were used in his study with the gap filled with water. Based upon his measured heat transfer rates and temperature distributions, he noted that the larger aspect ratios for all diameter ratios seemed to curtail the convective activity while the smaller aspect ratios for all diameter ratios seemed to promote convective activity. A multicellular flow regime was also postulated for the smallest diameter ratio cylinder investigated.

CHAPTER III

EXPERIMENTAL APPARATUS AND PROCEDURE

EXPERIMENTAL APPARATUS

The apparatus used in this investigation was designed to provide the capability to study the characteristics of natural convective flow between isothermal concentric spheres with different diameter ratios using both air and water as the gap media. A photograph of the assembled apparatus, utilizing water as the gap fluid, is shown in Figure 1. Figure 2 and Figure 3 present schematics of the entire operating system for water and air as the gap working fluid respectively. An equipment list is provided in Appendix II for reference purposes.

The same inner spheres, 9.00, 7.00, 5.50 and 4.50 inches in diameter, used in the heat transfer study by Scanlan et al [5] were also used in the current study. All of the inner spheres were fabricated from copper with an approximate wall thickness of 0.025 inch. In order to establish the flow visualization, a glass outer sphere was fabricated from two hemispheres with an inner diameter of 9.77 inches. The combination yielded diameter ratios (D_o/D_i) of 1.09, 1.40, 1.78, and 2.17 which are close to the values used in the heat transfer study of Scanlan et al [5]. This arrangement will allow convenient correlation between thermal and flow phenomena for this geometry.

The inner spheres were supported in the outer sphere by a

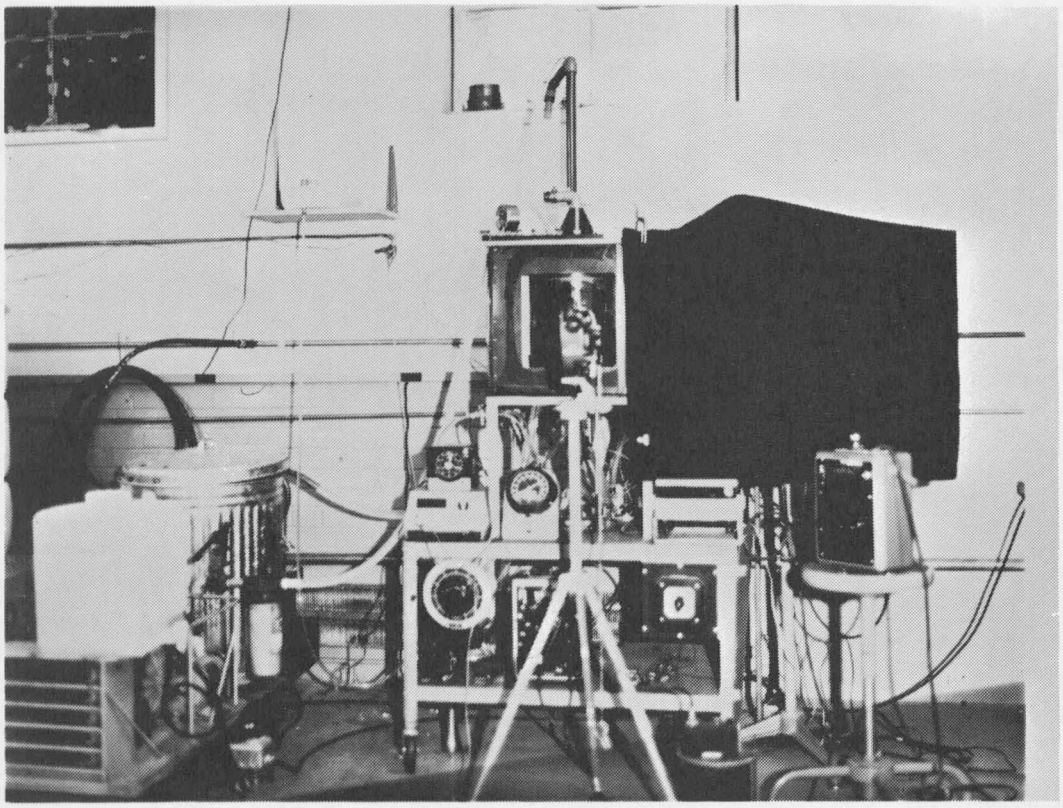


Figure 1. Assembled Apparatus with Water Cooling System

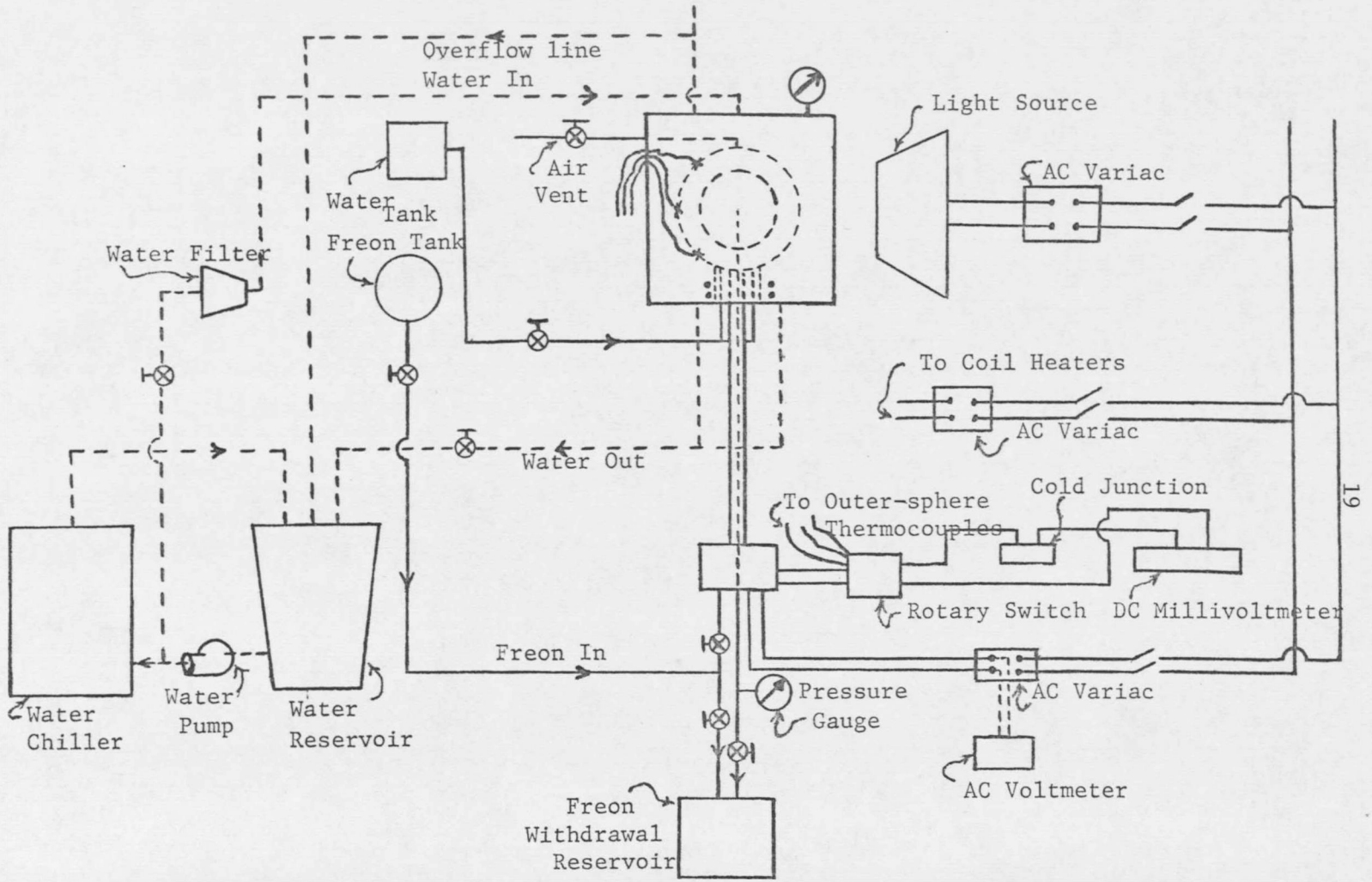


Figure 2. Schematic Diagram of Experimental System (Water as Gap Fluid)

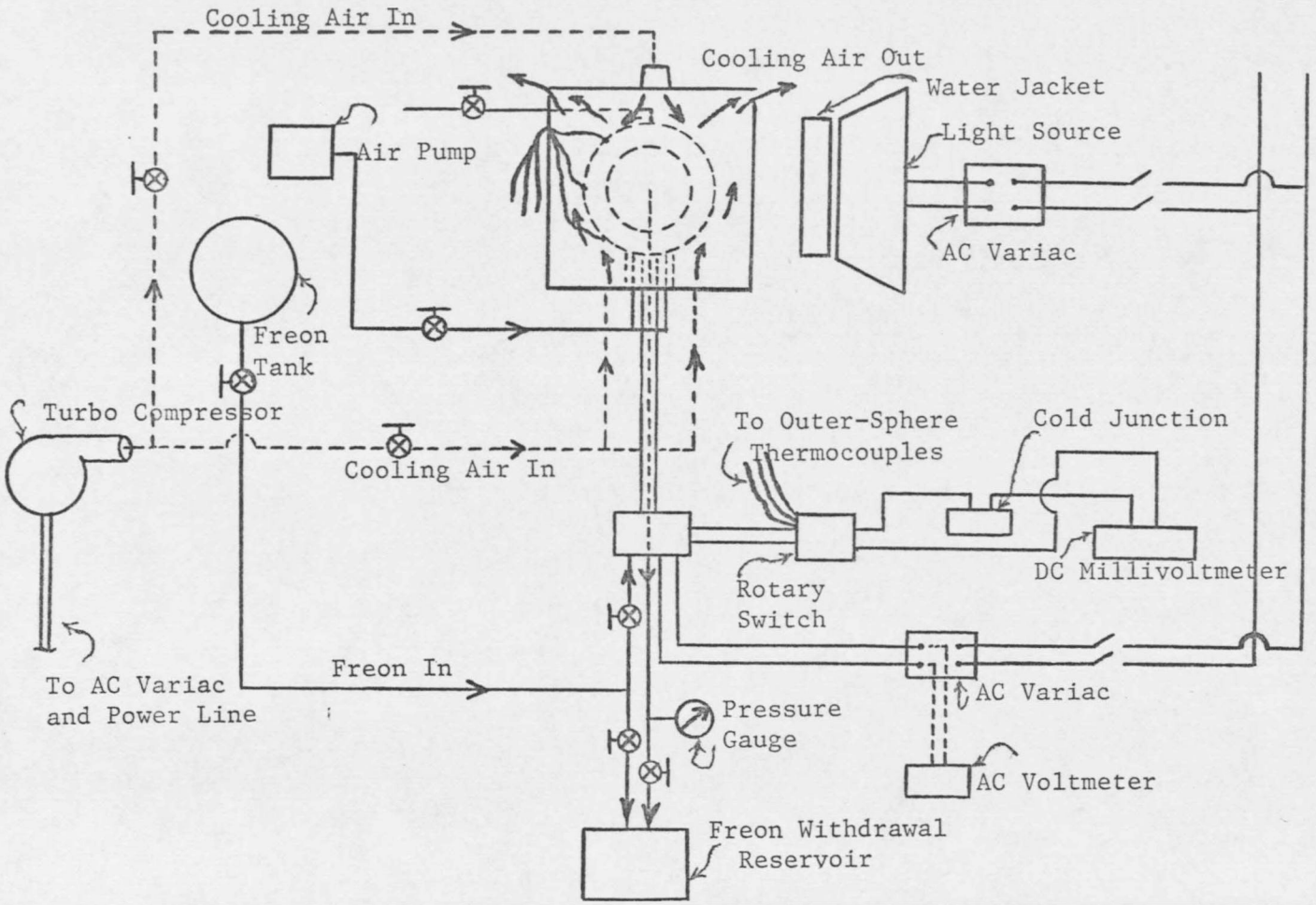


Figure 3. Schematic Diagram of Experimental System (Air as Gap Fluid)

stainless steel stem of 0.05 inch diameter and 0.065 inch wall thickness. The stem was insulated by using a plastic shrink tube to minimize lateral heat conduction through the tube. The stem, in addition to providing support for the sphere, served as a support for the electrical disk heaters and as a transfer tube for the power leads, thermocouples, and liquid Freon-11. Initially, the inner sphere was approximately half filled with Freon liquid and half with Freon vapor. The level of the Freon liquid could be controlled by a small stainless steel tube which acted as both a stand pipe for venting during the Freon-11 charging and as a means of measuring pressure within the inner sphere. The isothermal inner-sphere temperature was achieved by passing an electric current through the heater, which was located below the liquid level, causing a continuous Freon vaporization-condensation cycle. By varying the setting on an AC Variac located in the heater circuit, various inner sphere temperatures could be obtained. Figure 4 shows the arrangement of power leads, heaters, thermocouples, etc. inside the inner sphere.

The outer sphere consisted of two glass hemispheres with the separating plane located at an angle of 30 degrees with respect to the vertical axis. The hemispheres were joined together using a silicone sealant which yielded leak-proof sealing and ease of disassembly for changing the inner sphere. The inner diameter and

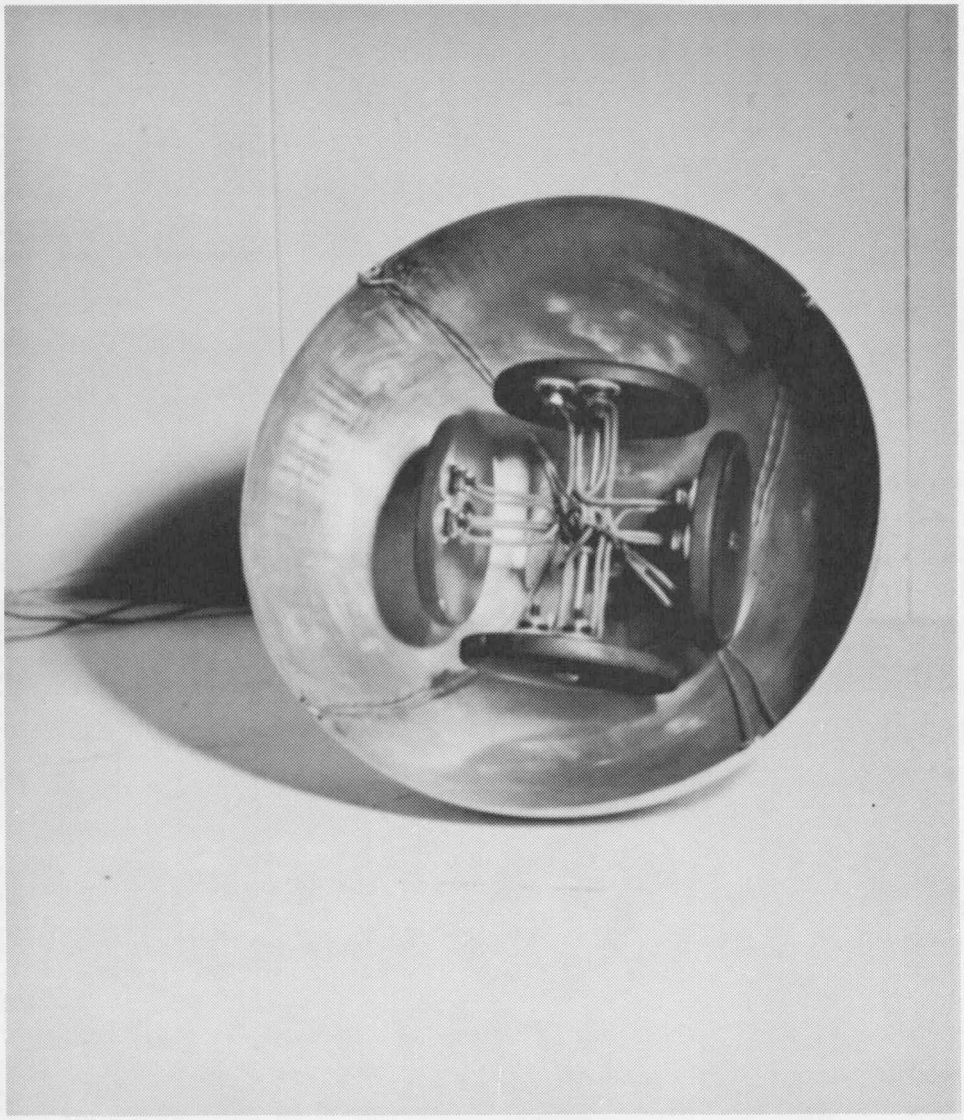


Figure 4. Interior of inner sphere

thickness of the glass sphere were 9.77 inches and 0.21 inch respectively. A 0.20 inch hole at the top served as an air vent while filling the gap with water. Another hole, 1.50 inches in diameter and located at the bottom, provided space for the stem of the inner body and a means of injecting the gap fluids. A 3.5 inch by 3.5 inch cylinder made of plexiglass was attached to the bottom of the glass sphere using epoxy cement. A tapered hole through the cylinder provided angular deflection of the stem permitting installation of the larger diameter inner-bodies. Figure 5 shows the two glass hemispheres. The installation of the inner sphere is illustrated schematically in Figure 6. The separating plane of the two hemispheres was rotated through an angle of 45° with respect to a front view before attaching the sphere to its plexiglass cubical enclosure. This prevented the plane from obstructing the flow visualization.

The cubical enclosure was made of plexiglass and has a characteristic length of 18 inches with a wall thickness of 0.5 inch. The enclosure was designed with a removable top cover for changing the spheres. The supporting cylinder of the glass sphere was mounted to the bottom of the enclosure using screws. In order to minimize optical reflections, the inner surfaces of the cubical enclosure were lined with thin phenolic sheets painted flat black with the exception of the viewing angle and a 0.2 inch lighting slit. The

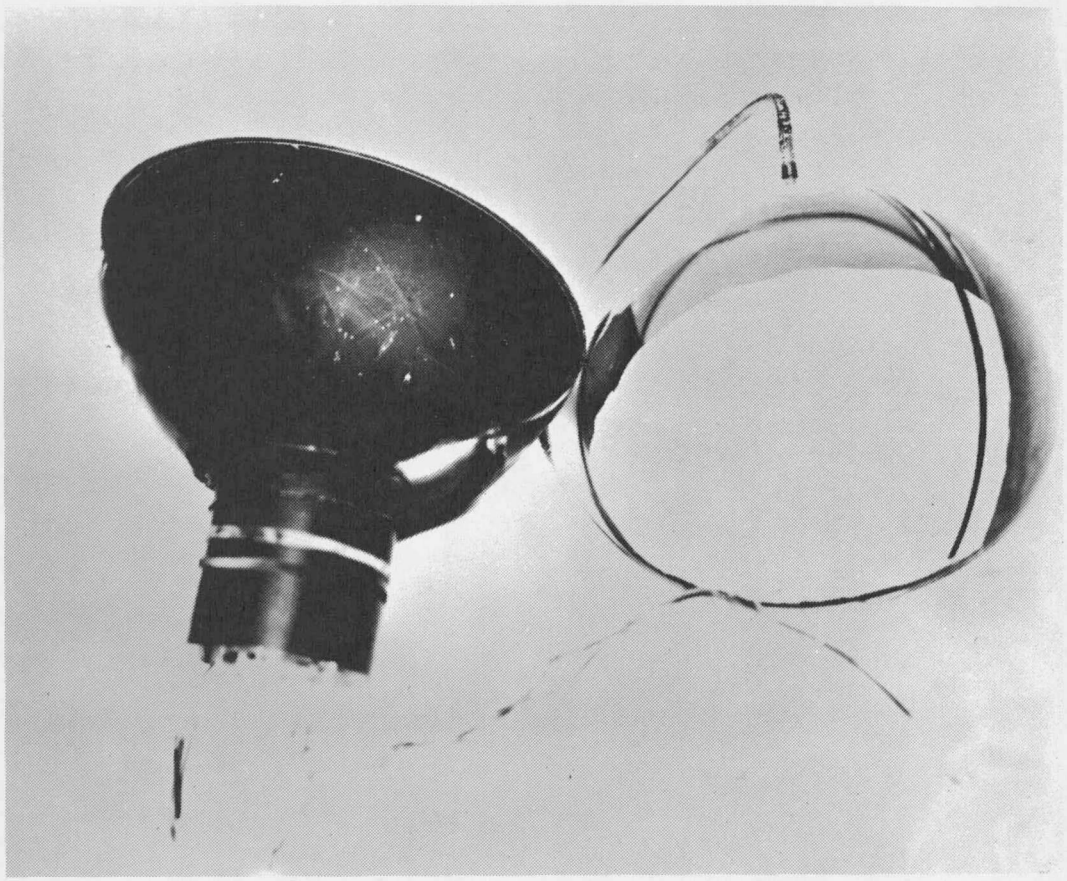


Figure 5. Glass Hemispheres

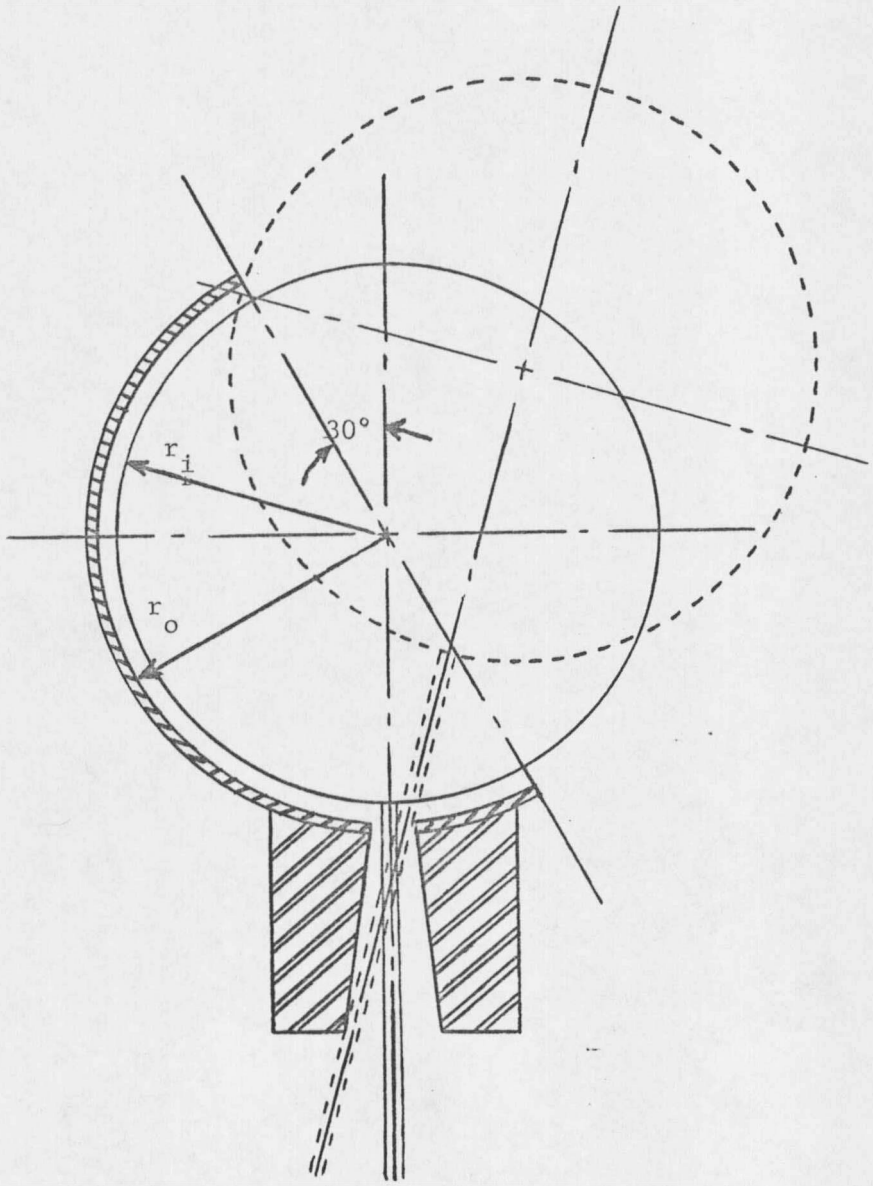


Figure 6. Installation of Inner-Sphere in the Glass Sphere

outer surface of the inner sphere and the majority of the inner and outer surfaces of the glass sphere were also sprayed with a thin black layer for the same purpose.

Both inner and outer sphere temperatures were monitored using copper-constantan thermocouples placed at various locations on the sphere surfaces. The thermocouples for the inner sphere were placed in the seam of the two hemispheres prior to final assembly. Six thermocouples, imbedded the depth of the wall thickness, were attached to the glass sphere with expoxy cement. The arrangement of the thermocouple locations was chosen such that during testing, it could be determined whether the sphere was being isothermally maintained. The surface temperature of the outer sphere was taken to be the average of these six thermocouple readings.

The cooling system used to maintain the isothermal condition of the glass sphere was determined by the gap fluid used. For air as the gap working fluid, a forced air draft was introduced into the cubical enclosure and was passed over the glass sphere from both the top and the bottom of the enclosure. It was withdrawn through a narrow gap underneath the edges of the top cover. The air draft was supplied by a turbo-compressor whose speed was regulated by an AC Variac. The flow rates of the top and the bottom manifolds were adjusted by metering valves on each air line. This arrangement

eliminated the problem of flow separation of the cooling air while passing over the glass sphere. The isothermal condition was then achieved by proper adjustment of the compressor speed and flow rates from each air line.

For water as the gap working fluid, a closed cooling system which included a reservoir, pump, water filter, chiller, and an overflow discharge line was used and operated with a flow rate of 5 GPM. The cooling water was introduced into the enclosure from the top and withdrawn from the bottom through a manifold system. A thin plexiglass cylinder, 12 inches in diameter, was placed inside the cubical enclosure surrounding the glass sphere. This resulted in achieving an increased velocity of the cooling fluid passing over the sphere.

It was necessary to fill the remaining space in the enclosure with water for flow observation to remove geometric optical distortion. This provided a plane surface through which the flow could be observed without the distortion caused by refraction at the curved water-glass-air interfaces. The supporting cylinder of the glass sphere was surrounded by two coil heaters connected to an AC Variac. During the operation of the cooling system, a certain amount of energy was supplied to these coil heaters. By doing this a cooling problem caused by a large variation of local heat transfer

rates along the inner surface of the glass sphere, caused by poor thermal conductance of the glass sphere, was minimized

The inner-sphere support stem passed through the outer sphere, a tapered hole and plug sealing device, and the cubical enclosure to connect to a small reservoir made of stainless steel. For sealing purposes, two O-rings were placed between the inner-sphere support tube and tapered plug, and two were placed between the tapered plug and the tapered hole in the outer-sphere support cylinder. The small stainless steel reservoir permitted the emergence of power leads, thermocouples, and standpipe by means of Conax fittings to provide leak-free integrity of the system. The reservoir also housed the Freon-11 fill port and the junction of the Freon-11 pressure gage. The reservoir rested on a threaded rod that allowed vertical adjustment of the inner sphere. The inner sphere could be accurately positioned within the outer sphere by utilizing a scale located beside the reservoir.

A light-tight box containing two 650 watt, air cooled, high intensity, quartz-iodine lamps provided a thin collimated plane of light for illumination of the annulus to enable flow visualization and photography. In conjunction with the use of tracers, this allowed the observation of the flow patterns occurring in a plane by viewing the spheres at right angles to the collimated light beam.

The tracers were introduced into the illuminated plane through four small tubes positioned beside the inner-sphere support-stem. For air as the gap medium, a preliminary observation indicated there was an effect on the flow patterns due to the radiant energy from the light beam. The same observation was also noted by Bishop and Carley [22] and Powe [27]. This effect was eliminated by passing the light through a 0.75-inch thick water plane when air was the working fluid. The circulating cooling water in the cubical enclosure served this same purpose during the studies using water as the gap fluid.

The introduction of tobacco (cigar) smoke into the spherical annulus was the flow visualization technique employed for air as the working fluid. For water as the working fluid, however, satisfactory tracers were unavailable. The ideal tracers for use in water should have the following characteristics:

(1) The tracer element must be neutrally buoyant with time and temperature variation,

(2) The tracer element must be visible and photographable,

(3) The tracer element must follow and indicate the actual physical flow phenomena.

In order to study the flow phenomena with water in the annulus, a special visualization technique was developed in the current study. The working fluid with the tracer was prepared in the following

manner:

(1) The needed quantity of distilled water was boiled. The purpose of this was to deaerate the water in order to minimize bubble collection on the inner surface of the glass sphere. Previously, these air bubbles caused the view of the flow to be partially obstructed.

(2) The boiled water was cooled to approximately 80°F.

(3) This water was then siphoned into a storage container to which was added a very minute amount of liquid detergent (3 gallons of water to approximately 15 drops of "Ajax"). Gentle shaking of the container was necessary to form a homogeneous mixture without introducing any air bubbles.

(4) After sitting several hours, numerous very small neutrally buoyant particles were observed in a lighted plane. Having obtained this condition, the mixture was introduced into the gap. Figure 7 shows these particles at rest within the spherical annulus before heating.

It was found that the concentration of particles was affected by the quantity of detergent added. Too much detergent caused the water to appear milky grey which reduced the contrast significantly.

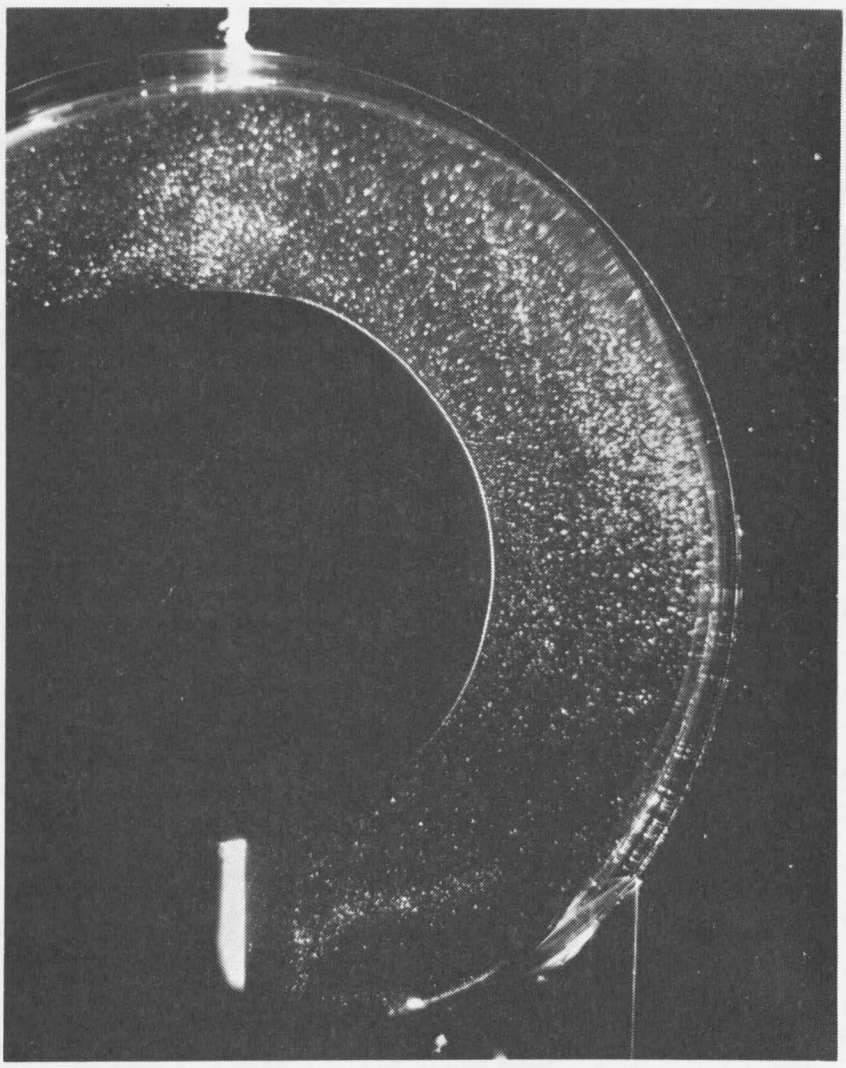


Figure 7. Particles in Water Within the Spherical Annulus Before Heating

It was also discovered that when the temperature of the mixture exceeded 120°F, the number of particles observed was considerably reduced. This visualization technique could very well prove useful for flow studies in other fields where water is the working medium.

Several different kinds of solid particles used by previous investigators were evaluated in the current study. Some of these were aluminum powders, polyethylene, polystyrene, and a type of small, hollow glass spheres called Eccospheres. All of these particles revealed the following disadvantages.

(1) They were not neutrally buoyant for a long period of time under the necessary variation of water temperature.

(2) Since the spherical annulus was an enclosed space, many particles were found to adhere to the inner surface of the glass sphere causing visual obstruction.

(3) In comparison to the detergent particles, most of the particles had poorer optical reflectivity and therefore were much more difficult to photograph.

Another flow visualization technique described by Baker [30] was also evaluated. A solution, prepared by adding a small amount of thymol blue PH indicator to distilled water, was introduced into the annulus. A blue dye was created in the gap upon impressing a small DC voltage between two electrodes within the solution.This method

proved unsuccessful because the contrast between the blue dye and the red solution was rather difficult to distinguish.

Still photographs of the flow patterns were obtained using a tripod-mounted 4"x5" Calumet Camera, and motion pictures were taken by use of a Beaulieu R 16mm "Automatic" photographic recorder. Fast film was selected due to the adverse lighting conditions. Kodak 4-X Reversal, 7277 16mm movie film was used for the motion pictures. All of the still photographs were taken with either Kodak Tri-X Pan Professional Film or Polaroid Black & White 3,000 speed Land film. In order to achieve good contrast, kodabromide F·4 print paper was used for enlargement and printing.

EXPERIMENTAL PROCEDURE

The desired inner sphere was selected and painted black before placing it within the glass outer sphere. A single-component, air-curing silicone sealant was used to join the two glass hemispheres. A leak-proof seal was obtained by allowing approximately 24 hours for the sealant to cure. The spheres were then installed within the cubical enclosure, followed by connection of the electrical power, thermocouples, and plumbing. The concentric location of the inner-sphere was ensured by the following simple procedure:

(1) Raising the inner sphere to its extreme upper location and recording the reading of the scale indicated by a needle mounted on the stem;

(2) Lowering the inner sphere to its extreme lower location and recording its corresponding reading; and

(3) Setting the inner sphere at the middle position between these two marks.

The Freon-11 fill and vent valves were opened. Both valves were then closed when a steady Freon-11 stream emerged from the vent line, which indicated the inner sphere was half full.

The following procedures were followed for water as the gap working fluid:

(1) The prepared working fluid was introduced into the

annulus from the container by gravity flow.

(2) As soon as the annulus was completely filled, the inlet valve was closed. The air vent was kept open to allow for thermal expansion of the fluid.

(3) The cooling system and AC Variac connected to the heaters in the inner sphere were turned on. The voltage was adjusted to yield the desired temperature.

(4) Power supplied to the coil heaters was then varied such that the inner surface of the enclosing sphere approached an isothermal condition.

(5) Allowing sufficient time for thermal equilibrium to be reached, the gap-flow phenomena were then investigated.

The following procedures were followed for air as the gap working fluid:

(1) The annulus was opened to the atmosphere through a smoke introducing valve.

(2) The AC Variac was adjusted to give the desired inner sphere temperature.

(3) The cooling fan was turned on and adjusted in speed. The upper and lower air flow rates were regulated by valves in the air lines to obtain the desired outer

sphere temperature,

(4) When thermal equilibrium was reached, cigar smoke was gently introduced into the gap. Before the flow pattern investigation, sufficient time was allowed to insure that the flow field was fully developed. It was found that the smoke density in the annulus affected only the pattern contrast and did not affect the flow pattern itself. Therefore the amount of smoke introduced into the annulus depended upon visual and photographic considerations.

Visual observation and photographs were made for each temperature difference achieved. A written description and motion pictures were also recorded for each type of flow pattern. In addition, the following data were recorded with each observation, photograph, and motion picture taken:

(1) Gap fluid,

(2) Gap pressure (for air only),

(3) Inner-sphere temperature,

(4) Outer-sphere temperature,

(5) Inner and outer sphere diameters,

(6) Heater voltage, and

(7) Run number.

The gap working media and associated geometric combinations in

the present investigation are shown in Table 1.

TABLE 1

GAP WORKING FLUID AND ASSOCIATED GEOMETRIC COMBINATIONS

Gap Working Fluid	Air			Water			
D_o (in)	9.77			9.77			
D_i (in)	4.50	5.50	7.00	4.50	5.50	7.00	9.00
D_o/D_i	2.17	1.78	1.40	2.17	1.78	1.40	1.09
L/D_i	0.59	0.39	0.20	0.59	0.39	0.20	0.04

CHAPTER IV

EXPERIMENTAL RESULTS AND DISCUSSION

From the data recorded, as stated in the previous chapter, for each of the flow patterns, the appropriate dimensionless parameters such as diameter ratio, relative gap thickness (L/D_i), Grashof number, Prandtl number, and Rayleigh number were calculated. The gap thickness, inner diameter, and inner radius were selected as the characteristic dimensions in the calculation of certain dimensionless parameters. Since a large amount of data was involved in this investigation, a data reduction program, written for the Xerox Data Systems Sigma 7 digital computer, was utilized to calculate thermocouple temperatures and properties of the gap working fluid and then to obtain the dimensionless parameters. A complete listing of this program for water as the gap working fluid and sample results from this program are found in Appendix III. For air as the gap working fluid, a listing of the data reduction program can be found in Powe [27]. In this data reduction process, all fluid properties, being temperature dependent, had to be evaluated at some suitable reference temperature. Previous investigations [5, 28] have demonstrated satisfactory results by utilizing the volume weighted mean temperature, T_{vm}, which is defined as:

$$T_{vm} = \frac{\left[(r_{avg}^3 - r_i^3)T_i + (r_o^3 - r_{avg}^3)\right] T_o}{r_o^3 - r_i^3} \qquad (4\text{-}1)$$

The physical interpretation of this mean temperature can be explained in the following manner: This temperature is determined by treating the fluid contained between the inner sphere and an imaginary sphere, of diameter equal to the arithmetic mean diameter of the inner and outer spheres, as being at the inner sphere temperature and the fluid contained between the imaginary sphere and the outer sphere as being at outer sphere temperature. An additional reference temperature was also employed. This was an arithmetic mean temperature defined as:

$$T_{am} = \frac{T_i + T_o}{2} \qquad (4\text{-}2)$$

For clarity, this chapter is presented in three sections; the flow pattern descriptions, the summary of experimental results, and the discussion of results. All those dimensionless parameters employed in this chapter are based upon gap thickness (L) as the characteristic dimension, and the fluid properties, being temperature dependent, are evaluated at the volume weighted mean temperature (T_{vm}) except when otherwise indicated. The term minimum observable value of Grashof

number used in this chapter is defined as the value corresponding to the smallest temperature difference ($\Delta T \sim 5°F$) for a given fluid and diameter ratio. The limiting value of the temperature difference was chosen such that any error introduced due to slight temperature variation on the spheres would be negligible.

FLOW PATTERN DESCRIPTIONS

This section is presented in such a manner as to give a detailed description of each flow pattern which was observed in the spherical annulus for increasing temperature differences with each diameter ratio. These descriptions are also supported by still photographs, motion pictures, and sketches. The results for both air and water as the gap working fluid are treated in two sub-sections.

AIR AS THE GAP WORKING FLUID:

The first spherical configuration utilized in this investigation consisted of a 4.50 inch diameter inner sphere and 9.77 inch diameter outer sphere, yielding a diameter ratio of 2.17 and a relative gap thickness (L/D_i) of 0.59. For a Grashof number (N_{GR_L}) above a minimum observable value of 72,000 (N_{RA_L} = 51,000) and below approximately 166,500 (N_{RA_L} = 118,000), a steady "crescent eddy" pattern was observed in the annulus. In the crescent eddy pattern, shown in Figure 8, the fluid immediately adjacent to the

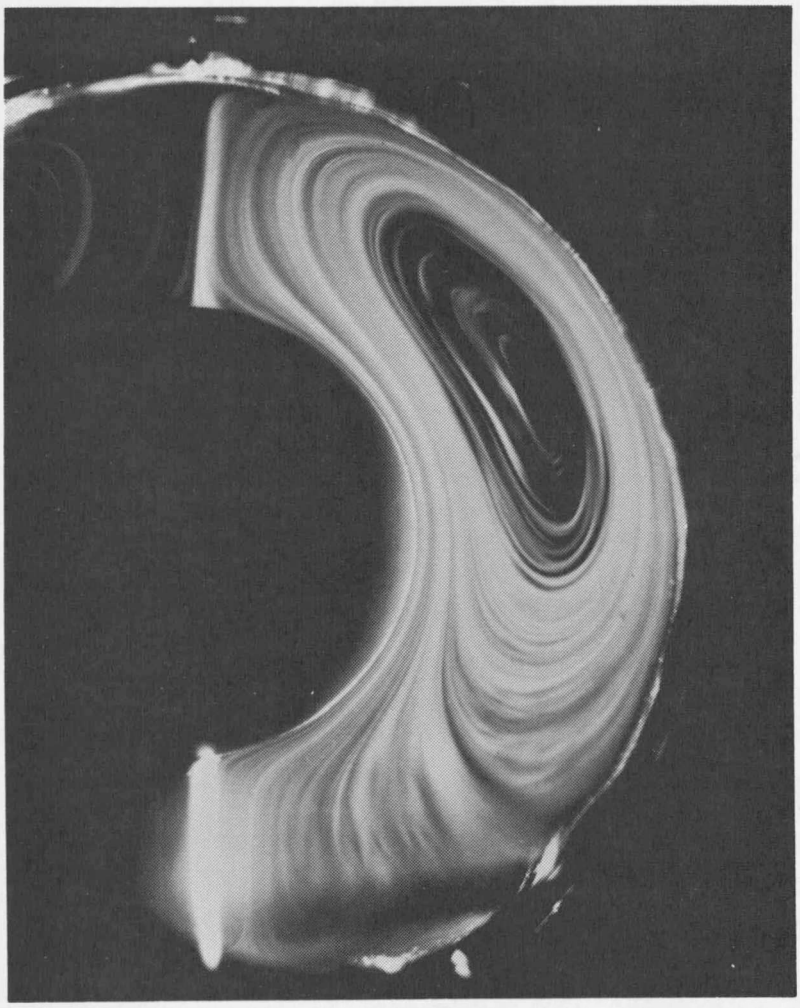


Figure 8. Steady Crescent Eddy Pattern for

$D_o/D_i = 2.17$ $L/D_i = 0.59$

$N_{GR_L} = 72{,}000$ $N_{GR_L} = 51{,}000$

spheres flows with a relatively large speed compared to that in the central and major part of the gap. Flow was upward along the inner sphere and downward along the outer sphere. The upward flow region was slightly thicker than the downward flow region. A distinct center of the crescent eddy was seen to be located above the horizontal and near the outer sphere. In the upper region of the gap, there was a distinct vertical dividing line, or chimney, between the two halves of the pattern. The flow did not extend completely into the lower region of the annulus, and this resulted in a relatively stagnant region. The downward flow along the outer sphere partially entered and expanded into this stagnant region. Meanwhile the fluid was also withdrawn from this region and converged into a thin layer as it moved upward along the inner sphere. This stagnant region appeared to decrease slightly in size as the Grashof number was increased. It was also observed that the location of eddy center moved radially outward and upward in angular position for an increase in Grashof number.

As shown in Figure 9 for a Grashof number of 166,500 (N_{RA_L} = 118,000), a small distortion emerges at the lower portion of the central low-speed region. The central flow region, shown in Figure 10 has become distorted into a kidney shape, as the value of Grashof number was increased. This kind of flow pattern was named

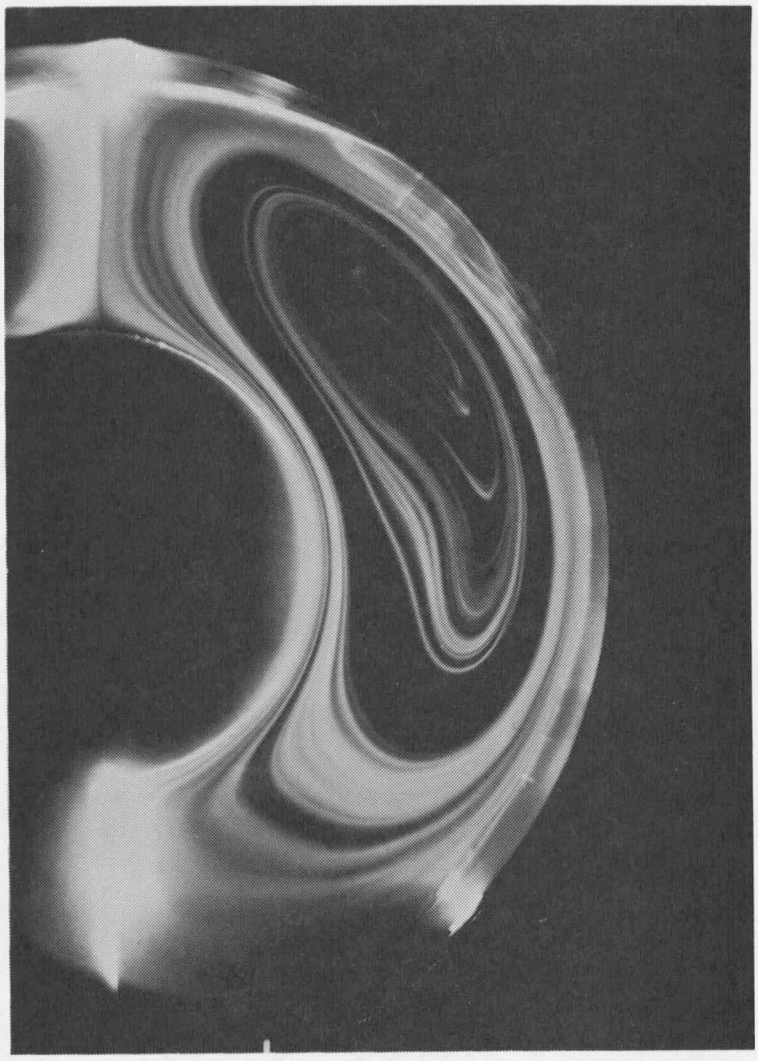


Figure 9. Photograph Showing Onset of Steady Kidney-Shaped Eddy Pattern for

$D_o/D_i = 2.17$ $L/D_i = 0.59$

$N_{GR_L} = 166,500$ $N_{RA_L} = 118,000$

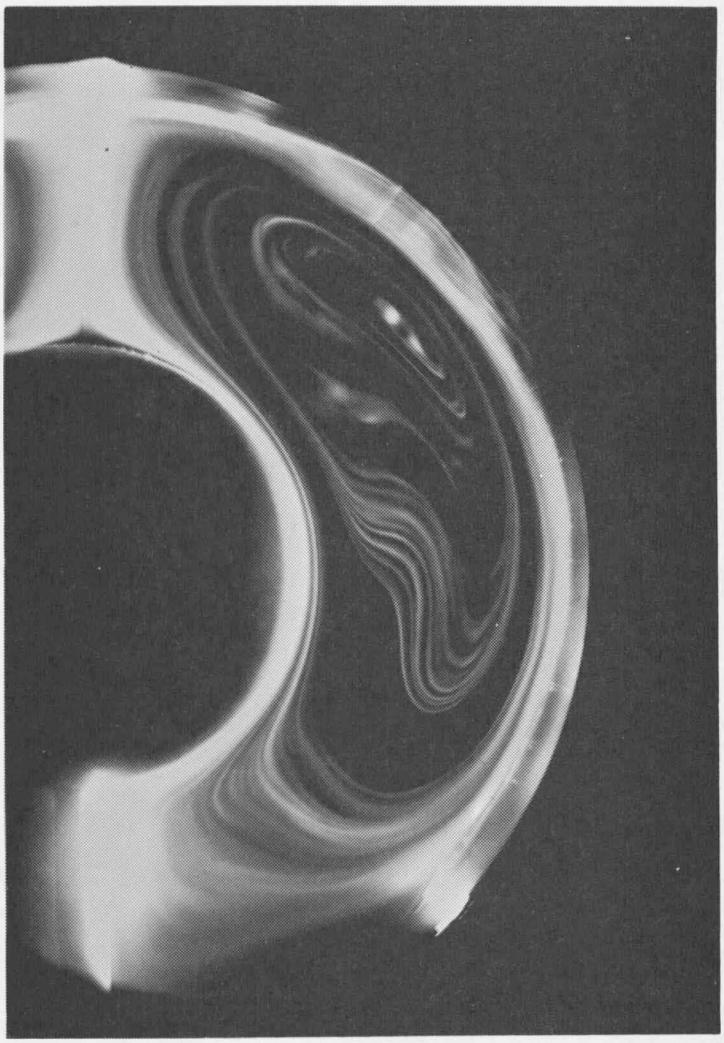


Figure 10. Steady Kidney-Shaped Eddy Pattern for

$D_o/D_i = 2.17$ $L/D_i = 0.59$

$N_{GR_L} = 295,800$ $N_{RA_L} = 209,600$

the "kidney-shaped-eddy" type due primarily to the shape of the central flow region. In the central low-speed flow region, the downward flow velocity at the outer boundary was significantly greater than the upward flow velocity on the inside of the region. This phenomenon was enhanced as the eddy center was shifted toward the outer sphere for a higher Grashof number, thereby indicating that continuity was satisfied. The distortion of the central low-speed region becomes more pronounced when associated with the Grashof number increasing as shown in Figure 11.

As the Grashof number was increased above the value of about 760,000 (N_{RA_L} = 535,000), a continuous radial wave motion was observed in the central low-speed flow region. This wave motion was characterized by continuous shifting of the flowlines in the radial direction from the vicinity of the eddy center toward the inner sphere. Consequently, this radially inward propagating flow combined with part of the low speed upward flow and then returned to the lower portion of the low speed central region through the region immediately adjacent to outer sphere high-speed layer, thereby indicating that continuity was satisfied in this low speed central region. During these occurrences, both the eddy center and the vertical chimney remained distinct and stationary in the flow field. Figure 12 shows a photograph of this flow pattern. This

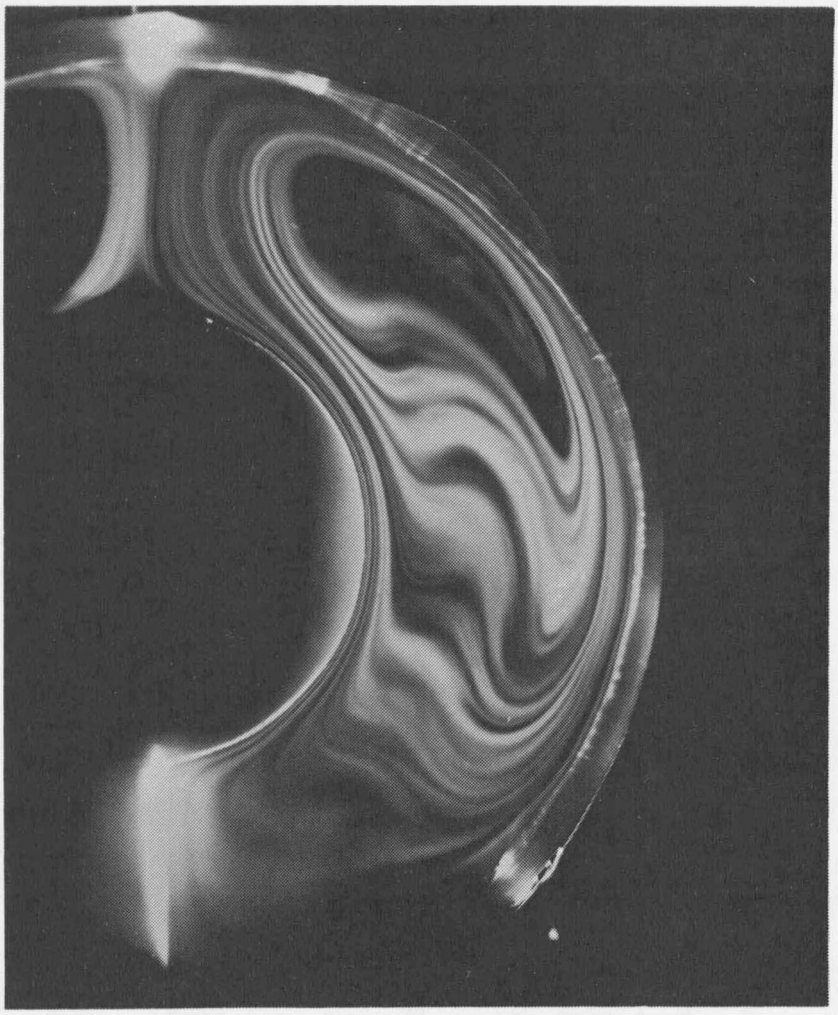


Figure 11. Steady Kidney-Shaped Eddy Pattern

$D_o/D_i = 2.17$ $L/D_i = 0.59$

$N_{GR_L} = 555{,}000$ $N_{RA_L} = 393{,}000$

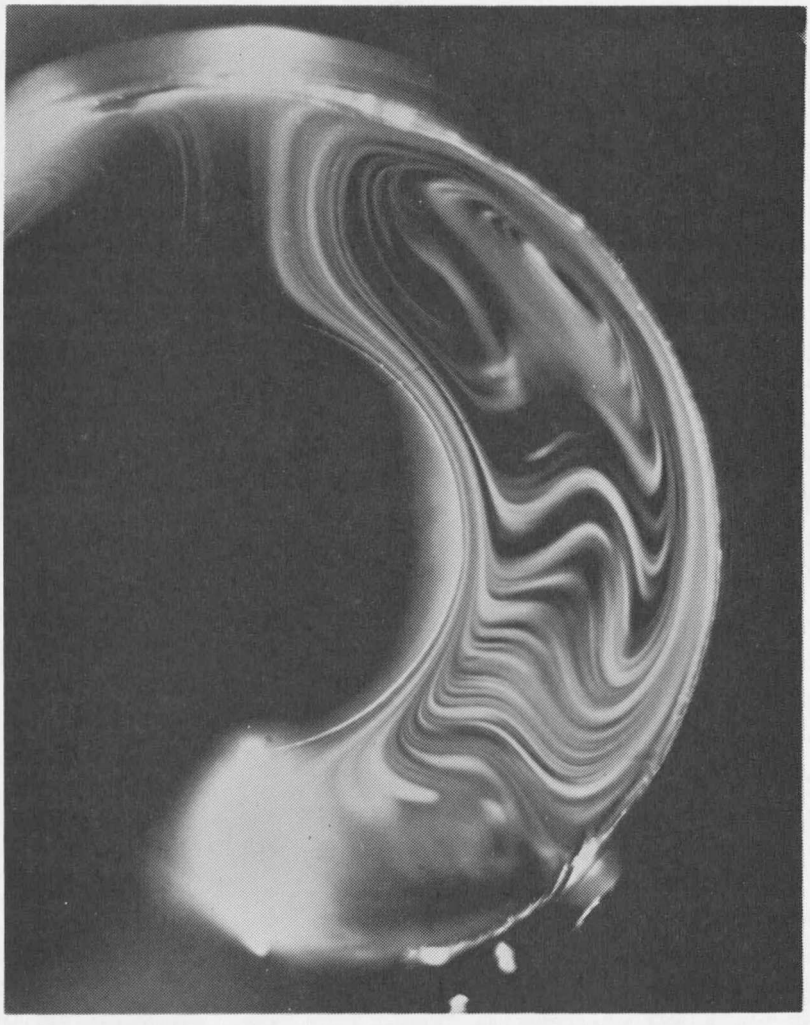


Figure 12. Steady Modified Kidney-Shaped Eddy Pattern for

$D_O/D_i = 2.17$ $L/D_i = 0.59$

$N_{GR_L} = 1{,}056{,}000$ $N_{RA_L} = 746{,}000$

same type of flow pattern continued to exist for Grashof numbers up to the value of 1,156,000 (N_{RA_L} = 816,000) which was the maximum value obtainable using this spherical combination in the current experimental apparatus.

The second spherical configuration to be studied consisted of a 5.50 inch diameter inner sphere and a 9.77 inch diameter outer sphere resulting in a relative gap thickness of 0.39 and a diameter ratio of 1.78. For Grashof numbers below about 165,000 (N_{RA_L} = 117,000), a steady crescent eddy pattern was again found to occur. This pattern, as before, was characterized by the relatively thin high-speed layers near the inner and outer spheres, with the flow being directed upward and downward along inner sphere and outer sphere respectively. As seen in Figure 13, the center of flow pattern was also located above the horizontal and nearer to the outer sphere. The position of the eddy center again appeared to have a tendency to move radially toward the outer sphere and upward in angular position as the Grashof number was increased. As before, a small stagnant region was observed in the lower portion of the annulus and a definite separation line was formed between two halves of the pattern at the extreme upper region. The minimum Grashof number which was obtained in this case was 42,700 (N_{RA_L} = 30,300).

As shown in Figure 14, a steady kidney-shaped eddy pattern, as previously described, was again obtained for Grashof numbers slightly

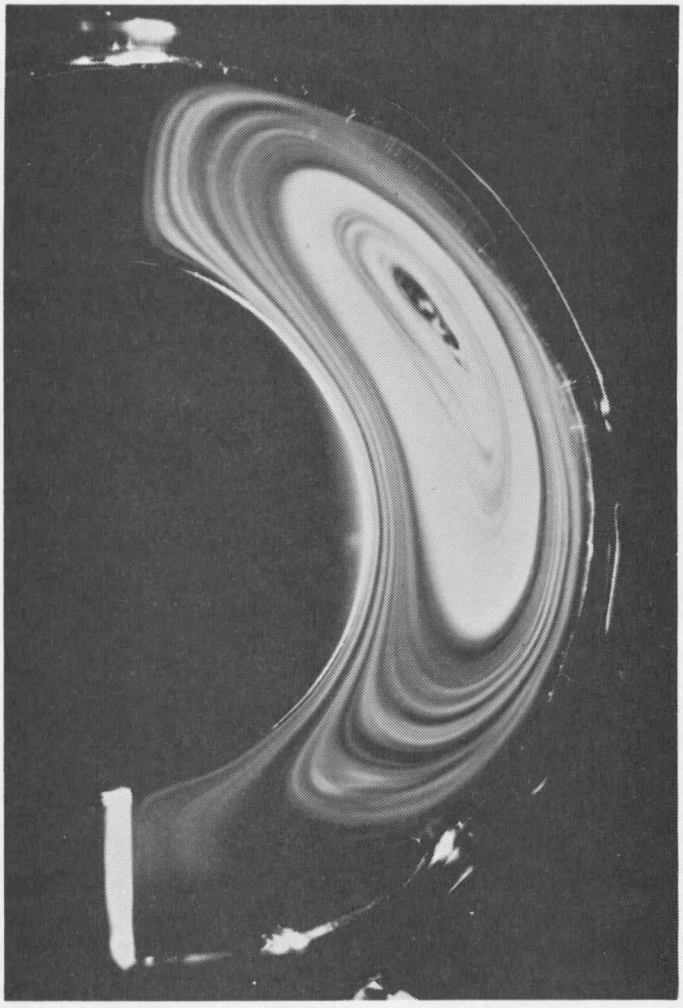


Figure 13. Steady Crescent Eddy Pattern for

$D_o/D_i = 1.78$ $L/D_i = 0.39$

$N_{GR_L} = 93,100$ $N_{RA_L} = 66,000$

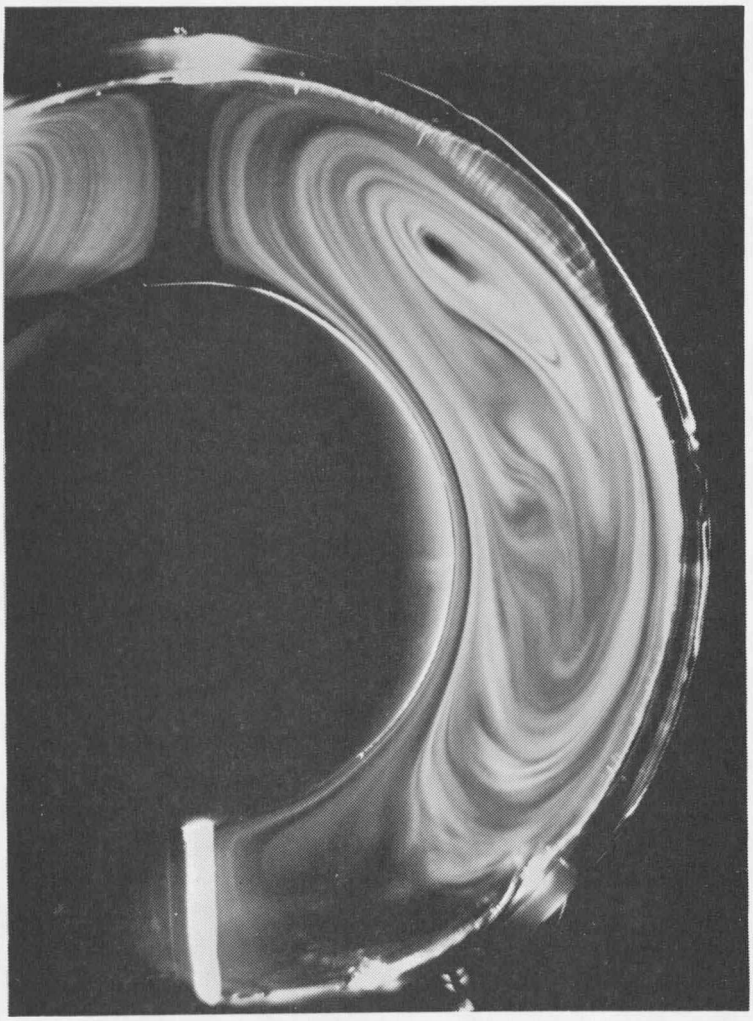


Figure 14. Steady Kidney-Shaped Eddy Pattern for

$D_o/D_i = 1.78$ $L/D_i = 0.39$

$N_{GR_L} = 194,000$ $N_{RA_L} = 137,400$

above the value of 165,000. Again the distortion of the low speed flow region was observed to become more pronounced for an increasing Grashof number. This steady pattern existed undisturbed until a Grashof number of about 246,000 (N_{RA_L} = 174,000) was reached. At this point, a periodic contraction with an irregular period of occurrence was found in the lower portion of the central flow region as shown in Figure 15. For a value of the Grashof number of about 275,000 (N_{RA_L} = 194,600), as illustrated in Figure 16, this interior contraction motion becomes more violent, and a radial shifting motion of the flowlines in the central flow region appeared. The center of the eddy, at this point, still remained visible; however, when the Grashof number was increased above approximately 317,000 (N_{RA_L} = 224,000), the center of the eddy was no longer distinct, and a very slight tangential oscillation of the chimney occurred due to the violent motion in the central region. This type of flow pattern is illustrated in Figure 17. It was noted that the rate of occurrence of the interior contraction increased for increasing Grashof number.

The above described unsteady flow pattern continued to exist in the annulus as the Grashof number was increased, although the contraction motion became more violent in the central flow region. The maximum observable Grashof number for this spherical configuration was 614,000 (N_{RA_L} = 434,000).

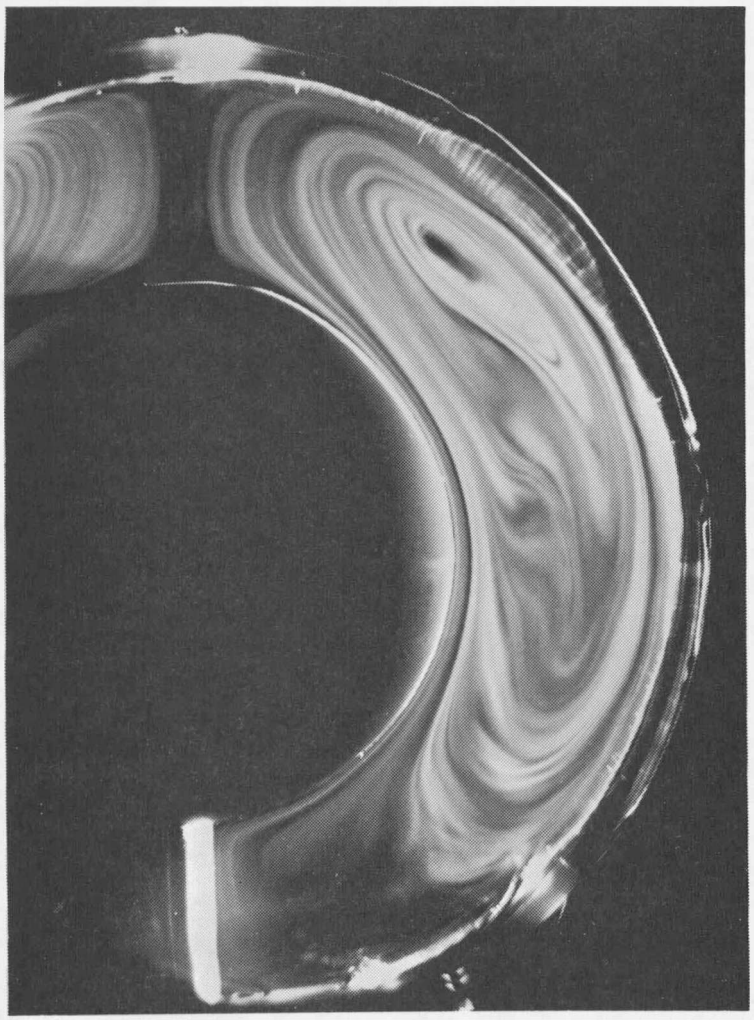


Figure 15. Photograph of Flow Pattern for

$D_o/D_i = 1.78$ $L/D_i = 0.39$

$N_{GR_L} = 246,700$ $N_{RA_L} = 174,600$

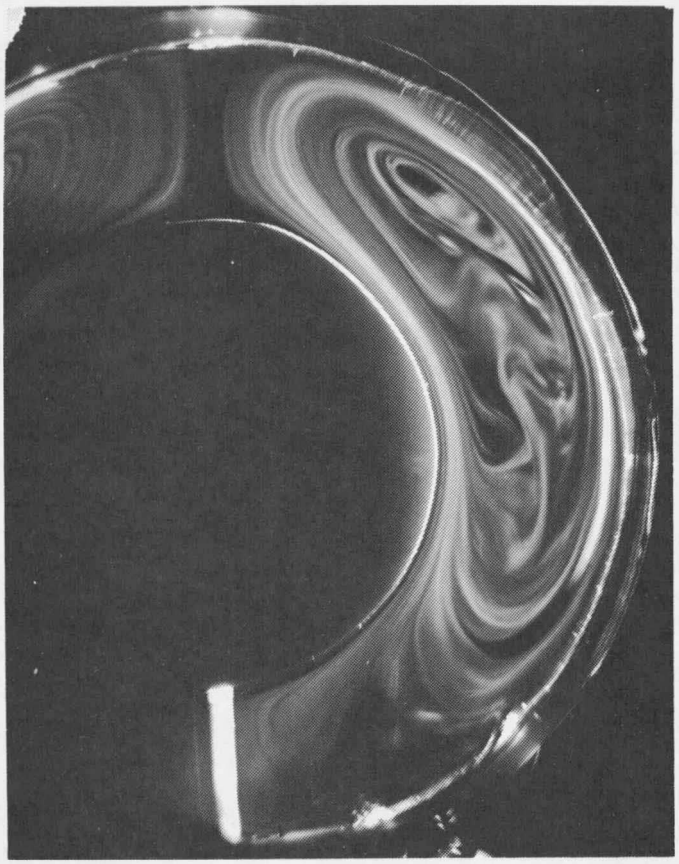


Figure 16. Photograph of Flow Pattern for

$D_o/D_i = 1.78$ $L/D_i = 0.39$

$N_{GR_L} = 275{,}000$ $N_{RA_L} = 194{,}600$

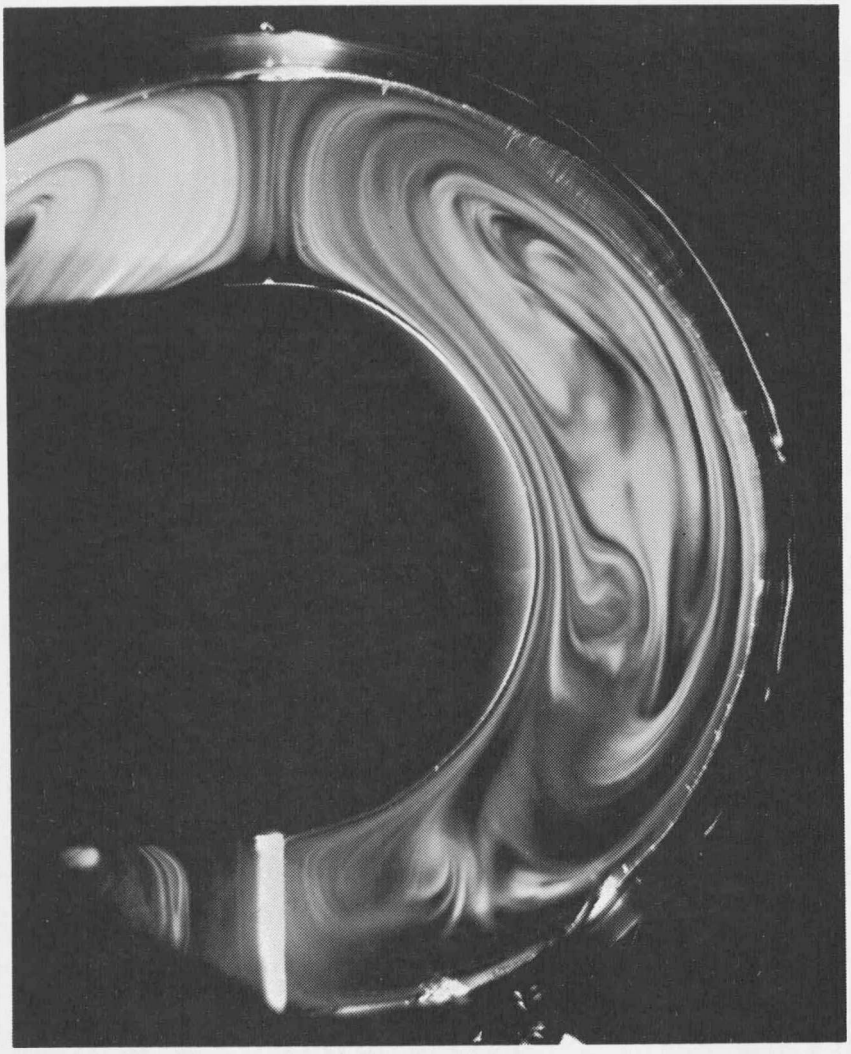


Figure 17. Periodic Interior Contraction Flow for

$D_o/D_i = 1.78$ $L/D_i = 0.39$

$N_{GR_L} = 323,000$ $N_{RA_L} = 228,400$

The final set of spheres to be considered in this portion of the investigation consisted of a 7.00 inch diameter inner sphere and a 9.77 inch diameter outer sphere. A diameter ratio of 1.40 and a relative gap thickness of 0.20 were obtained from this combination. For Grashof numbers between 7,000 (N_{RA_L} = 4,950) and 96,000 (N_{RA_L} = 68,000), the flow in the annulus was again characterized by a steady crescent eddy pattern. Before the value of Grashof number of 17,000 (N_{RA_L} = 12,000) was reached, the main flow did not extend completely into the upper portion of the annulus resulting in two small secondary cells forming in the extreme upper portion of the annulus--one to either side of the sphere's vertical axis. For this case, these cells were completely stationary and rotated in opposite directions. Each of them also rotated counter to the large eddy adjacent to it. Since the flow extended completely into the lower portion of the annulus, no stagnant condition was found in this region. The center of the pattern, in this case, was seen to be located slightly above the horizontal. This flow pattern described above is presented schematically in Figure 18 and photographically in Figure 19. When the Grashof number was slightly increased, the main eddy extended completely into the upper portion of the annulus, and at this point no distinct cells were observed in this extreme upper region as illustrated in Figure 20. This same type of flow pattern continued to exist for Grashof numbers up to

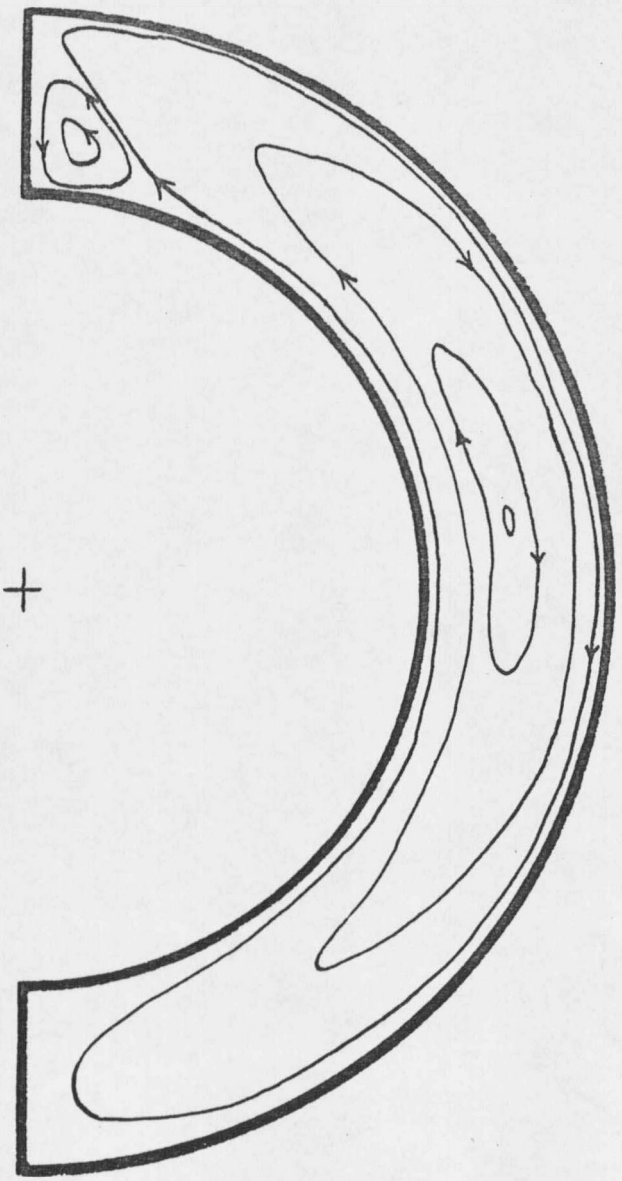


Figure 18. Sketch of Flow Pattern for $D_o/D_i = 1.40$ $L/D_i = 0.20$, $N_{GR_L} = 8{,}400$, $N_{RA_L} = 5{,}950$

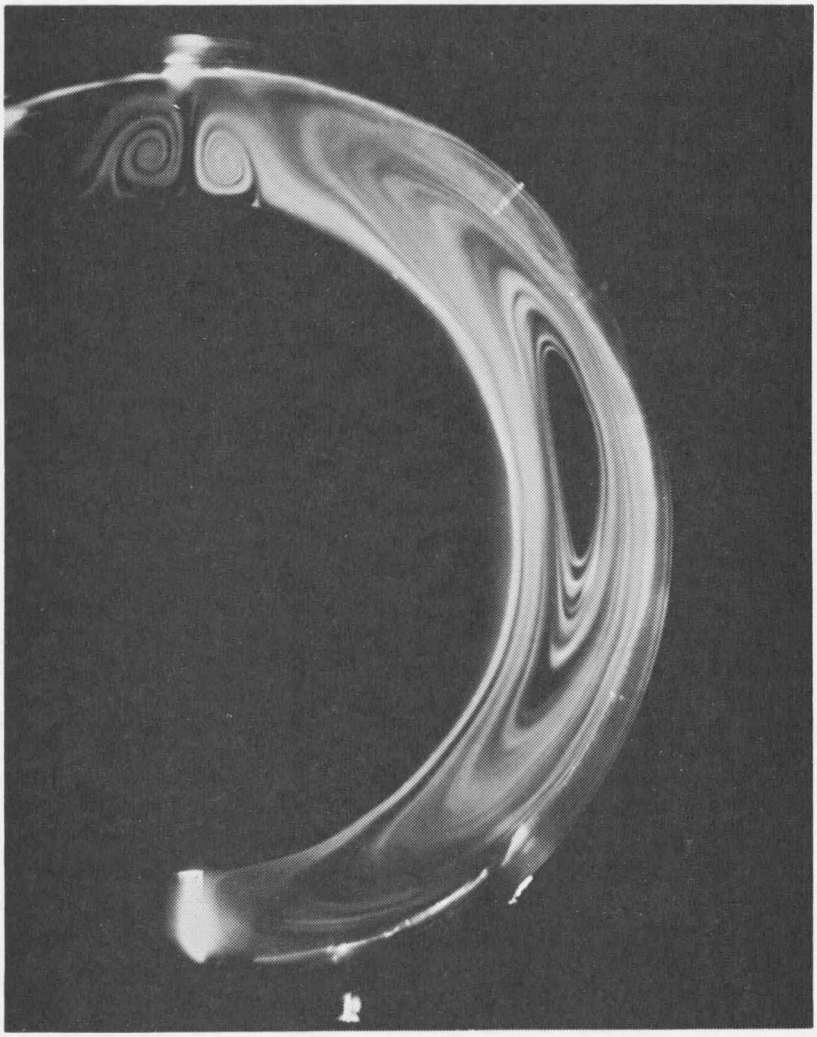


Figure 19. Photograph of Flow Pattern for

$D_o/D_i = 1.40$ $L/D_i = 0.20$

$N_{GR_L} = 8,400$ $N_{RA_L} = 5,950$

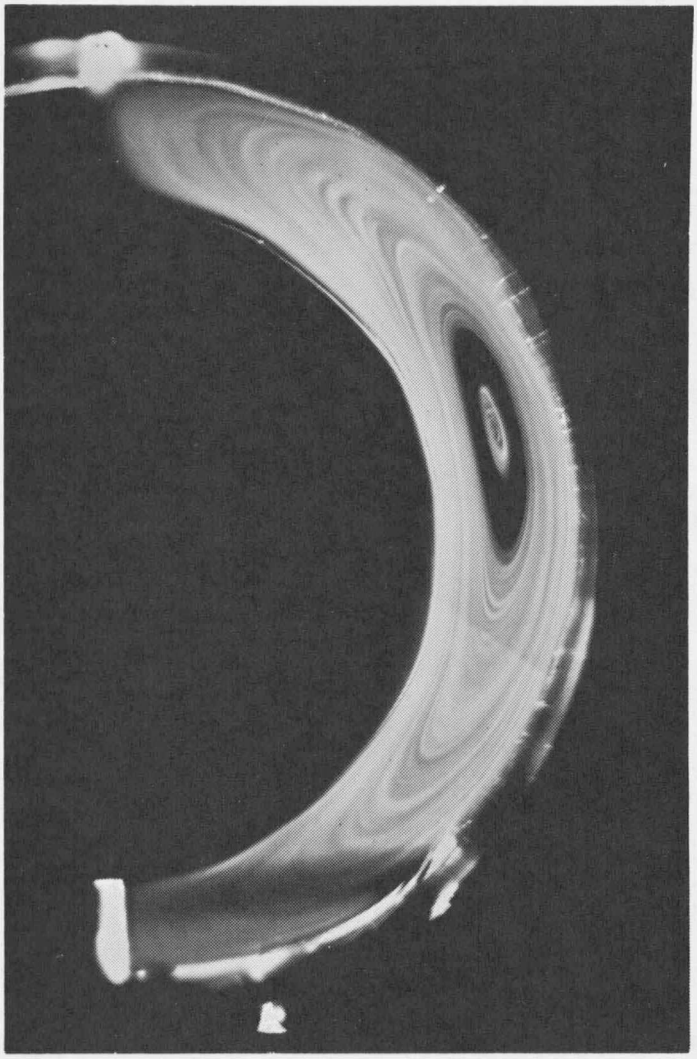


Figure 20. Steady Crescent Eddy Pattern for

$D_o/D_i = 1.40$ $L/D_i = 0.20$

$N_{GR_L} = 25,000$ $N_{RA_L} = 17,700$

96,000, although the eddy-center location was shifted upward in angular position along the same radius with increasing Grashof number.

As the Grashof number was increased slightly over a value of 96,000, the high speed upward flow adjacent to the inner sphere started to separate from the inner sphere at about an angle of 40° measured from the upward vertical axis, and a slight distortion of the separation flowline was observed to occur, although the chimney was still distinguishable (Figure 21). When the Grashof number reached the value of 99,000 (N_{RA_L} = 70,000), the flow field in the annulus was unsteady. This flow pattern was characterized by the following motions: The high-speed flow along the surface of inner sphere shot into the upper portion of the annulus resulting in rolling vortices, usually one or more pairs, in counter-rotation with each other. Those cells were associated with sideways oscillations about the vertical, and periodically, the cells might disrupt but were immediately reformed. Due to this sideways oscillation in the upper region, a slight tangential motion was impressed on the main cell. It should be pointed out that the chimney no longer existed in this upper region. The fluid in the upper portion then flowed downward via the inner surface of the outer sphere, returning to the lower portion of the annulus with a three-dimensional

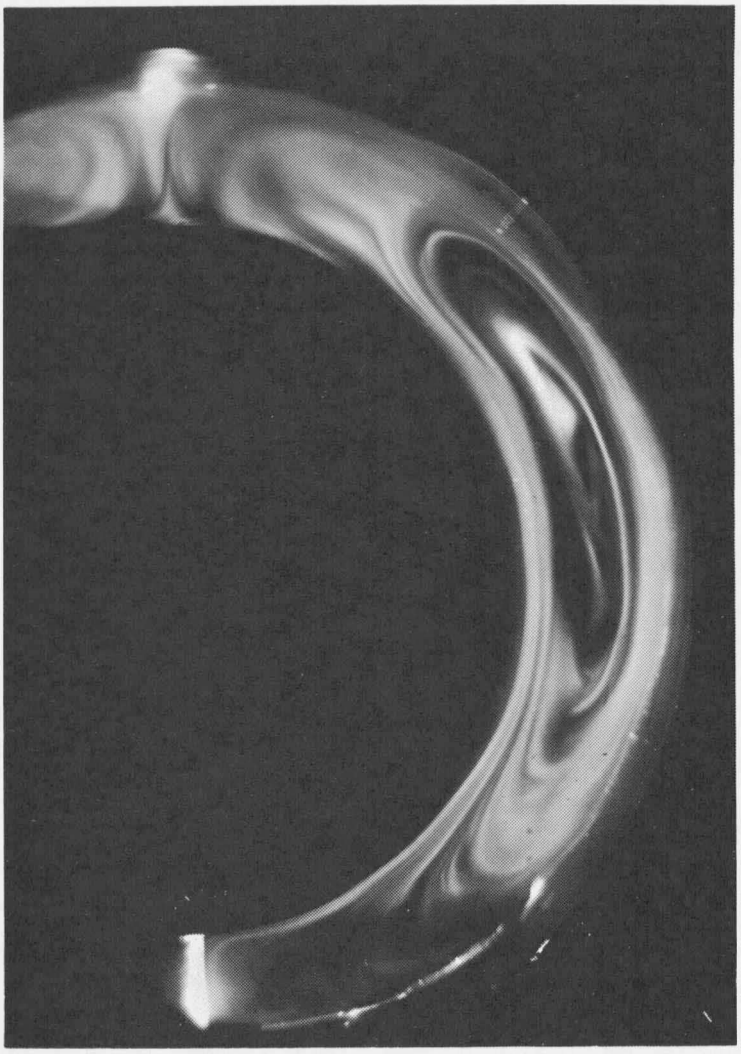


Figure 21. Photograph of Flow Pattern for

$D_o/D_i = 1.40$ $L/D_i = 0.20$

$N_{GR_L} = 99,300$ $N_{RA_L} = 70,000$

spiral motion. There was no distinct center of this pattern, and flowlines appeared not to maintain a constant position but were shifted in the radial direction. This appeared to be caused by large slugs of fluid flowing from the upper region of the annulus to the lower portion, resulting in a relatively thick downflow region adjacent to the outer sphere. Following this action, the up-flow region adjacent to the inner sphere would expand to a relatively large thickness to throw the fluid into the upper portion, thereby maintaining continuity. There was no definite period of occurrence for the above described sequence of motion, and again the frequency of occurrence increased with Grashof number. Figures 22, 23, and 24 show this type of flow pattern sequentially.

The above unsteady oscillating three-dimensional spiral flow continued to be seen up to the maximum observed Grashof number 120,000 (N_{RA_L} = 85,100).

WATER AS THE GAP WORKING FLUID

The first spherical configuration utilized in this investigation was exactly the same as the first configuration used for the air. This corresponded to a diameter ratio of 2.17 and a relative gap thickness of 0.59. A steady "dog-face" type pattern occurred in the annulus for Grashof numbers (N_{GR_L}) above a minimum observable value of 156,000 (N_{RA_L} = 1,785,000) and below approximately 3,600,000



Figure 22. Photograph Showing Counter Rotating Cells in Upper Region of Annulus for $D_o/D_i = 1.40$ $L/D_i = 0.20$ $N_{GR_L} = 103,800$ $N_{RA_L} = 73,200$

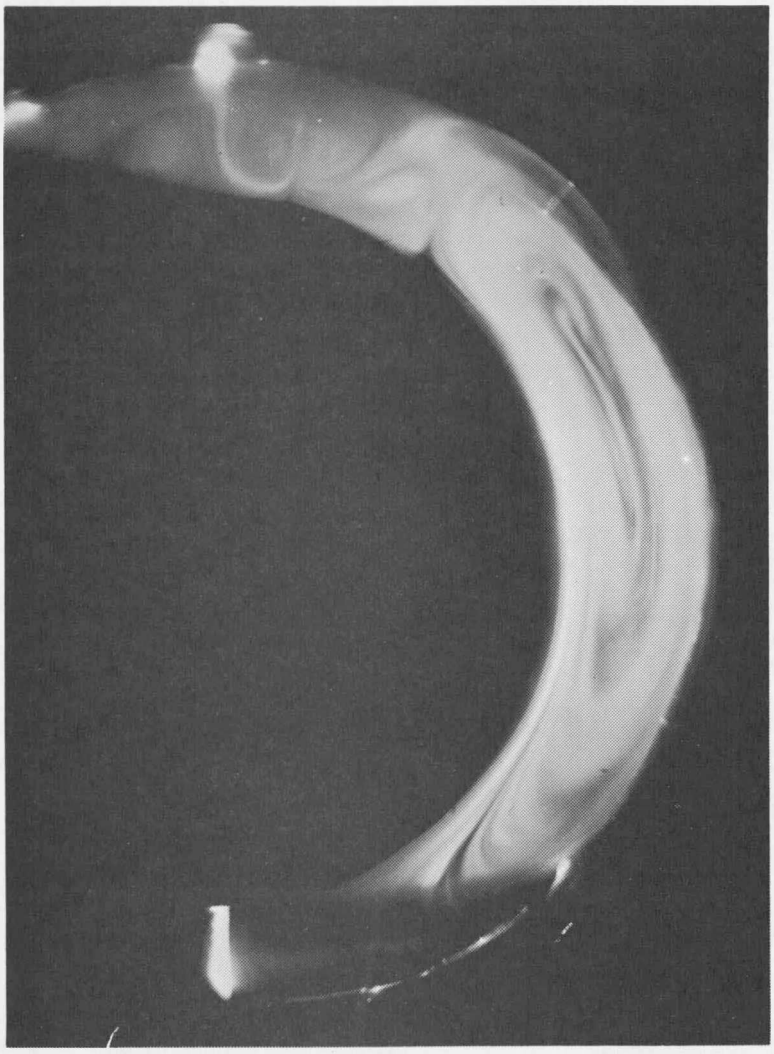


Figure 23. Photograph Showing Counter Rotating Cells in Upper Region of Annulus for

$D_o/D_i = 1.40$ $L/D_i = 0.20$

$N_{GR_L} = 103,800$ $N_{RA_L} = 73,200$

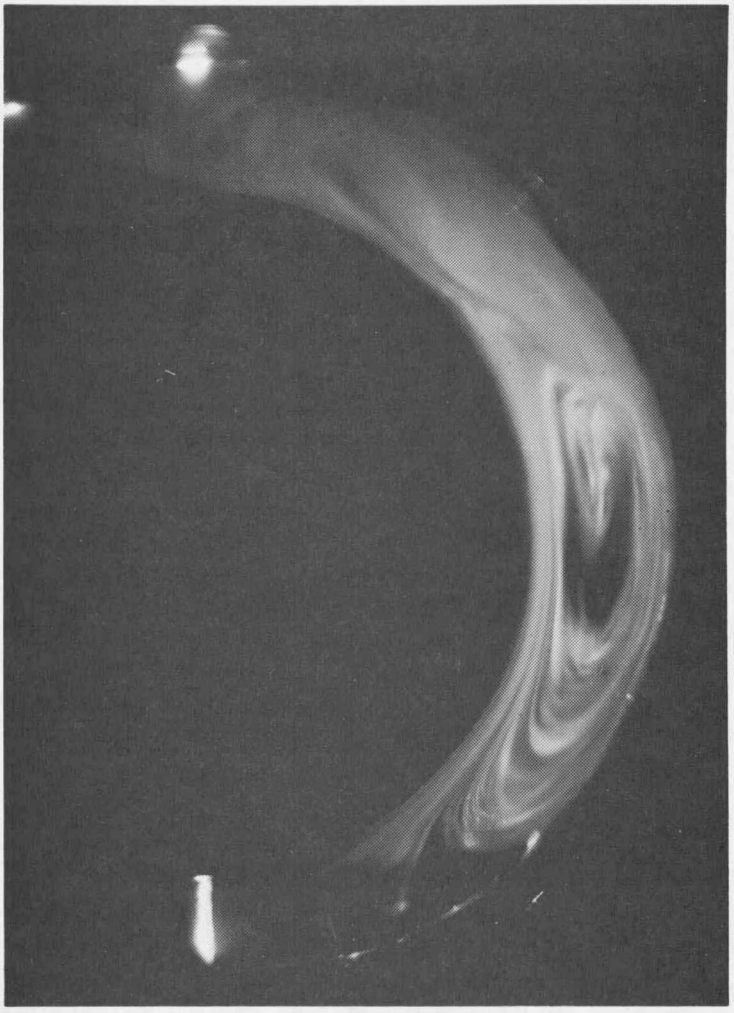


Figure 24. Three-Dimensional Spiral Motion in Upper Gap Region for $D_o/D_i = 1.40$, $L/D_i = 0.20$

$N_{GR_L} = 103,800$ $N_{RA_L} = 73,200$

(N_{RA_L} = 29,400,000). A representative sketch and photographs of this pattern are shown in Figures 25, 26, and 27. Three distinct regions can be seen in this pattern. (1) A thin high speed primary-flow region is observed in the vicinity of each sphere. The fluid in this region moves upward along the inner sphere, resulting in a vertical dividing line in the upper portion of the annulus, and downward along the outer sphere with relatively high speed compared to the fluid in other regions. The maximum velocity appeared to be near the top of the inner sphere. (2) An interior low speed secondary-flow region is observed in the upper portion of the annulus. Here there were two secondary flows circulating in the same direction as the primary flow. One of them was attached to the inner sphere producing a weak return flow to the near vicinity of the inner sphere. The other appeared at the extreme top and adjacent to the chimney. Evidently, a weak shear layer occurred between these two cells. It should be noted that a weak flow from the lower cell was observed to migrate toward the outer sphere boundary layer. (3) The major part of the annulus consisted of a central stagnant region in which no detectable flow could be observed. More detailed discussion of this typical flow phenomenon will be presented in the next section.

The steady dog-face pattern described above continued to be

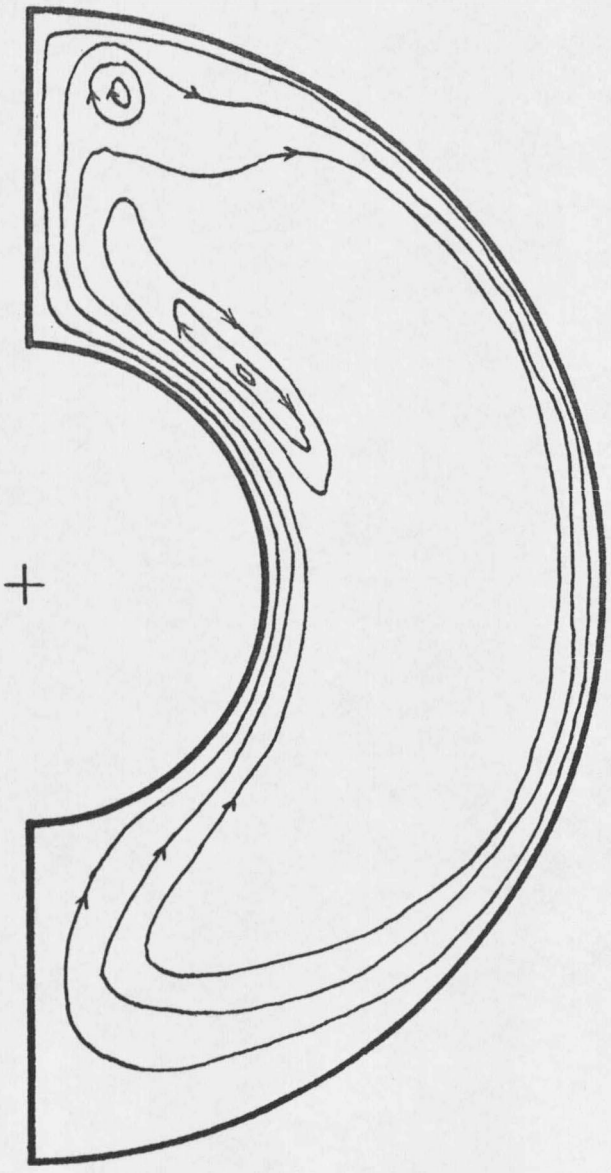


Figure 25. Sketch of Steady Dog-Face Pattern for
$D_o/D_i = 2.17$, $L/D_i = 0.59$
$N_{GR_L} = 248{,}800$, $N_{RA_L} = 2{,}812{,}000$

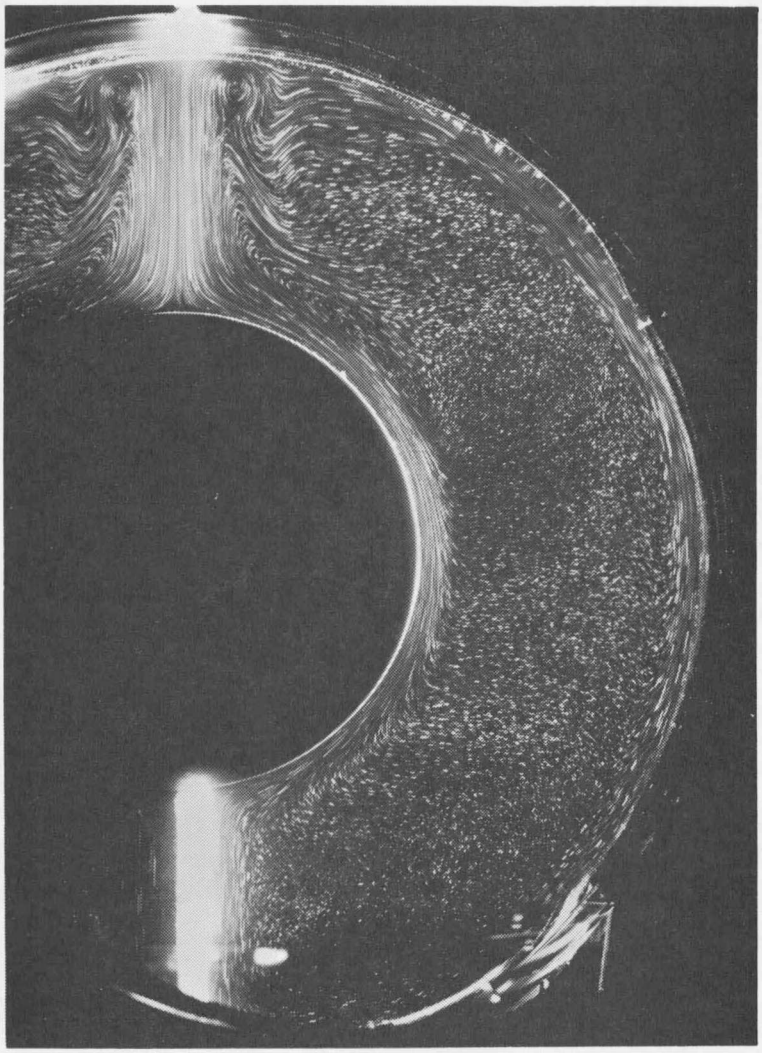


Figure 26. Steady Dog-Face Pattern for

$D_o/D_i = 2.17$ $L/D_i = 0.59$

$N_{GR_L} = 248,800$ $N_{RA_L} = 2,812,000$

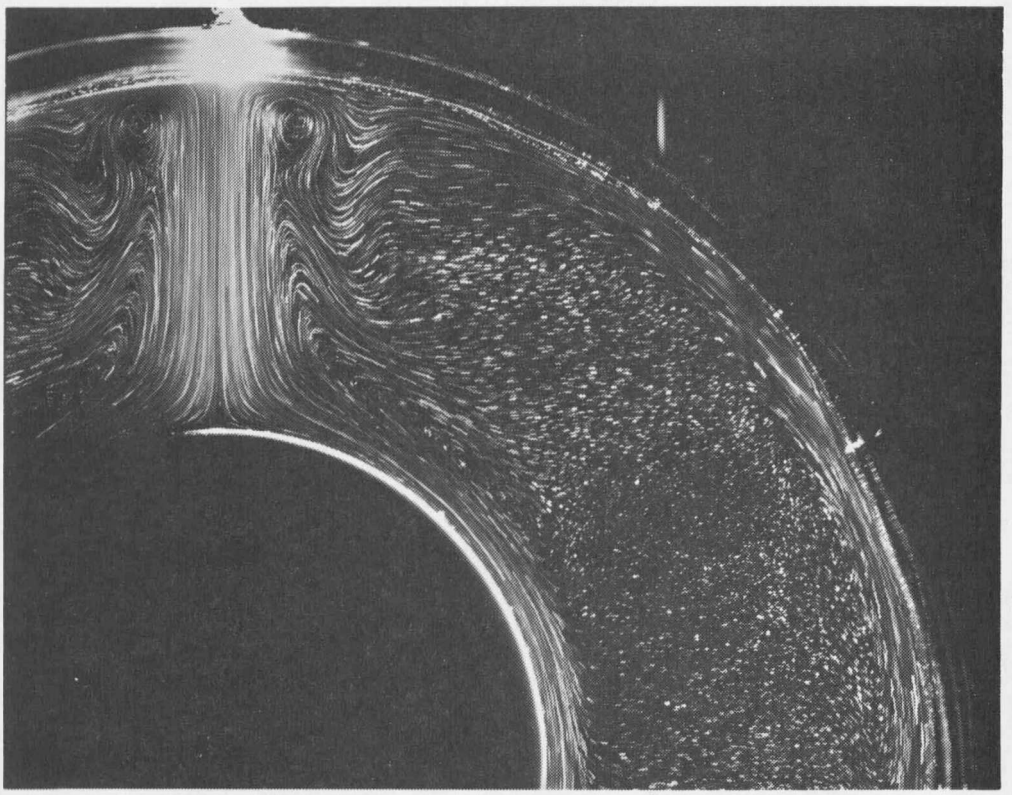


Figure 27. Steady Dog-Face Pattern (Upper Portion) for

$D_o/D_i = 2.17$ $L/D_i = 0.59$

$N_{GR_L} = 248,800$ $N_{RA_L} = 2,812,000$

observed until a Grashof number of 3,600,000 (N_{RA_L} = 29,400,000) was reached. The following minor changes in the flow field were observed as the Grashof number was increased; (1) the flow speed in the high-speed primary flow region increased and caused a considerable decrease of the wall-layer thickness, (2) the upper secondary cell increased in size, and the position of this cell center appeared to shift away from the chimney due to an increase of the chimney area, and (3) a slightly random motion occurred in the upper interior region of the annulus. These minor changes of flow pattern can be seen by comparing Figure 26 with Figure 28.

When the Grashof number was increased above a value of 3,600,000, the upper secondary cell was no longer stationary. At this point, the upper secondary cell was formed and appeared to submerge into the relatively stagnant region of the upper interior portion of the annulus causing a somewhat random motion to occur. Meanwhile, the fluid also discharged from this region along the inner surface of the outer sphere with a rolling vortex motion, thereby indicating that continuity was satisfied. The occurrence of the flow phenomena was repeated with an indefinite period, although the frequency appeared to increase with Grashof number. The majority of the fluid in the annulus still remained in the stagnant condition, and no detectable motion was found at this point.

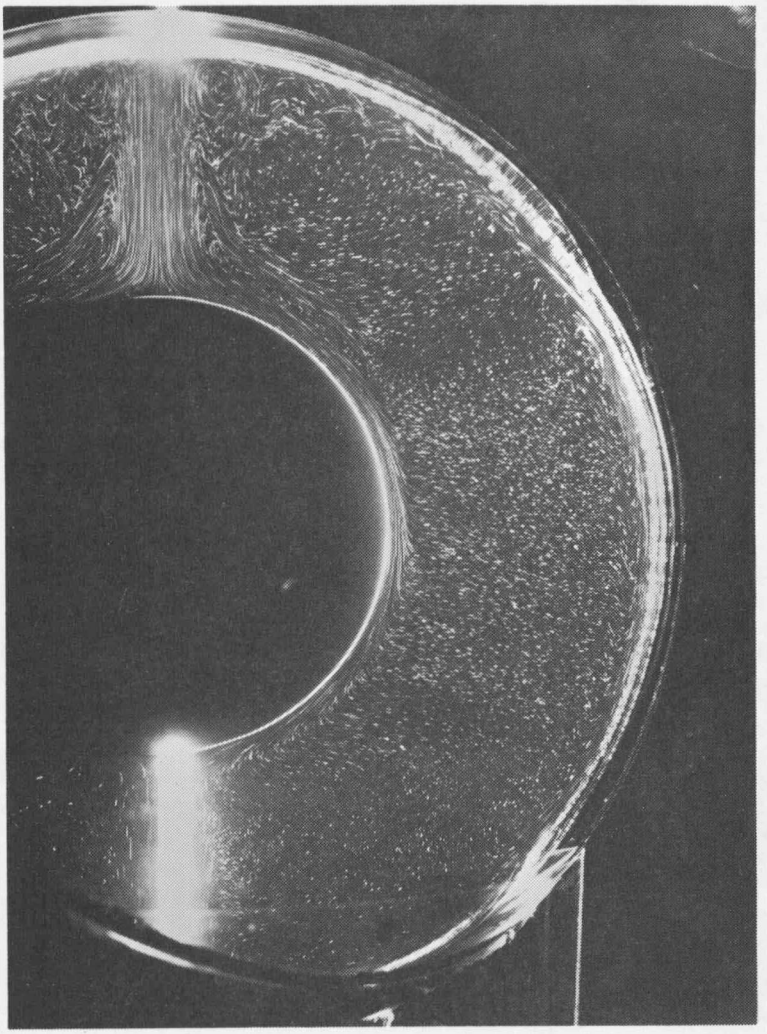


Figure 28. Photograph of Flow Pattern for

$D_o/D_i = 2.17$ $L/D_i = 0.59$

$N_{GR_L} = 1,345,000$ $N_{RA_L} = 12,554,000$

The above described pattern continued to exist in the annulus up to the maximum observable Grashof number of 14,200,000 (N_{RA_L} = 92,830,000) for this spherical configuration.

As shown in Figure 29, a steady dog-face pattern, as previously described, was again obtained for Grashof numbers less than 1,184,000 (N_{RA_L} = 10,350,000) while using an inner sphere of 5.50 inch diameter and an outer sphere of 9.77 inch diameter to yield a relative gap thickness of 0.39 and a diameter ratio of 1.78. This pattern, as before, consisted of three distinct regions: (1) a high speed primary-flow region, (2) an interior low speed secondary-flow region, and (3) a central stagnant region. The minor changes, as previously described, associated with increasing Grashof number again occurred in this case. The smallest observable Grashof number was 150,000 (N_{RA_L} = 1,600,000).

The steady dog-face type flow pattern existed undisturbed until a Grashof number of 1,184,000 was reached. At this point, a weak tertiary cellular motion was generated in the weak shear region between the secondary cells. The upper secondary cell grew in size and changed in shape. On the other hand, the lower secondary cell was reduced in size, and most of the flow in this region returned to the outer sphere high-speed layer instead of to the inner-sphere layer as before. Also, a considerable amount of random motion was

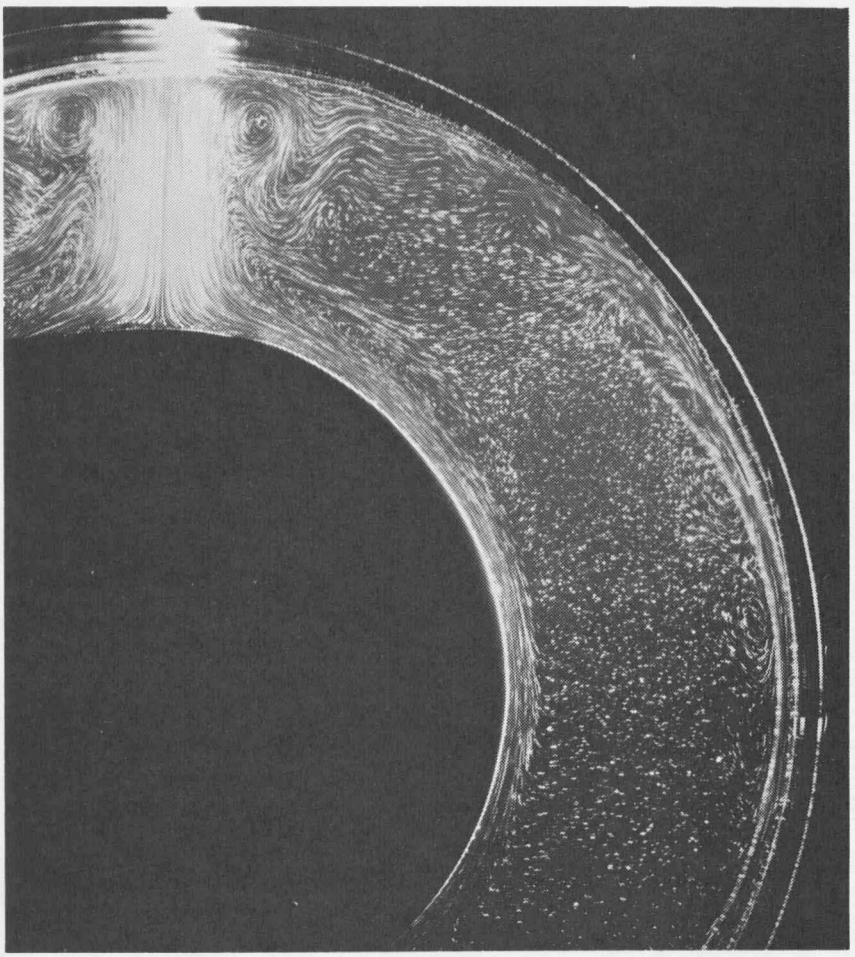


Figure 29. Steady Dog-Face Pattern for

$D_o/D_i = 1.78$ $L/D_i = 0.39$

$N_{GR_L} = 404{,}000$ $N_{RA_L} = 3{,}992{,}000$

observed in the interior low speed secondary-flow region. Figures 30, 31, and 32 show sketches and photographs of this flow pattern for increased Grashof numbers. The maximum number at which observations were made was 5,530,000 (N_{RA_L} = 37,530,000).

The next spherical configuration to be studied in this portion of the investigation consisted of an inner sphere 7.00 inches in diameter and an outer sphere 9.77 inches in diameter yielding a relative gap thickness and a diameter ratio of 0.20 and 1.40 respectively. For Grashof numbers below about 1,224,000 (N_{RA_L} = 8,322,000) a steady dog-face pattern was again found to occur in the annulus. In this case, the locations of the interior secondary cells were tangentially shifted away from the chimney compared to the two previous configurations. A region of interior low speed secondary-flow occupied most of the upper portion of the annulus. The minimum value of Grashof number utilized for this configuration was 58,500 (N_{RA_L} = 579,000). A photograph of this pattern is shown in Figure 33. An interesting phenomenon, flow reversal, was seen in the annulus along the major portion of the central stagnant region adjacent to the high-speed wall layers at higher Grashof numbers.

As the Grashof number was increased above a value of about 1,224,000, the flow did not extend into the entire upper portion of the annulus thus leaving two small secondary cells--one to either

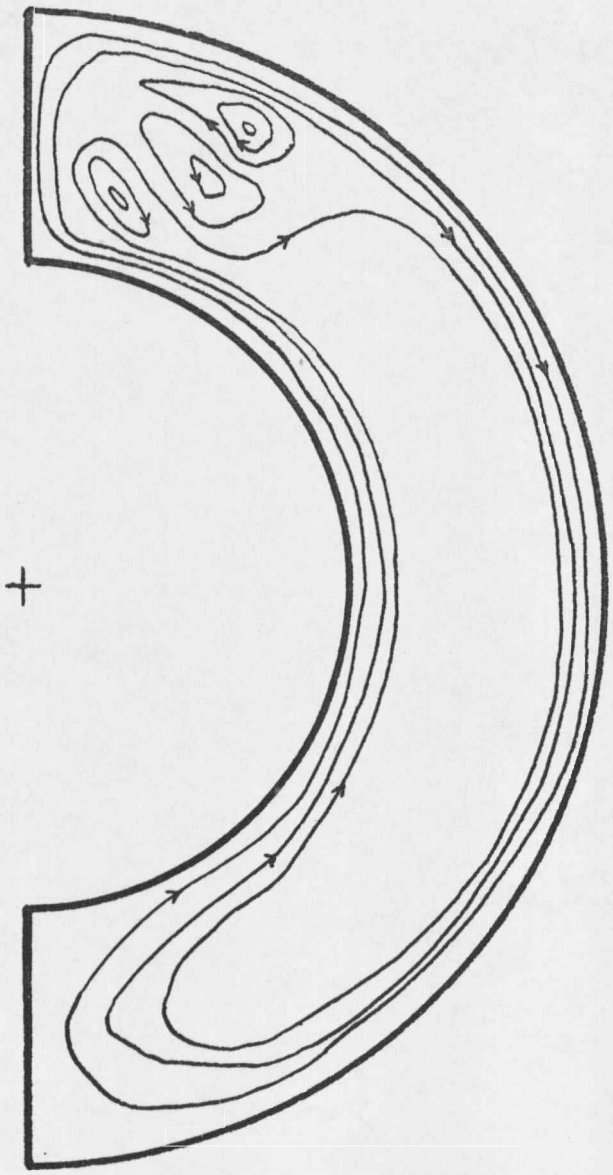


Figure 30. Sketch of Tertiary Flow Pattern for
$D_o/D_i = 1.78$, $L/D_i = 0.39$
$N_{GR_L} = 1{,}688{,}000$, $N_{RA_L} = 14{,}170{,}000$

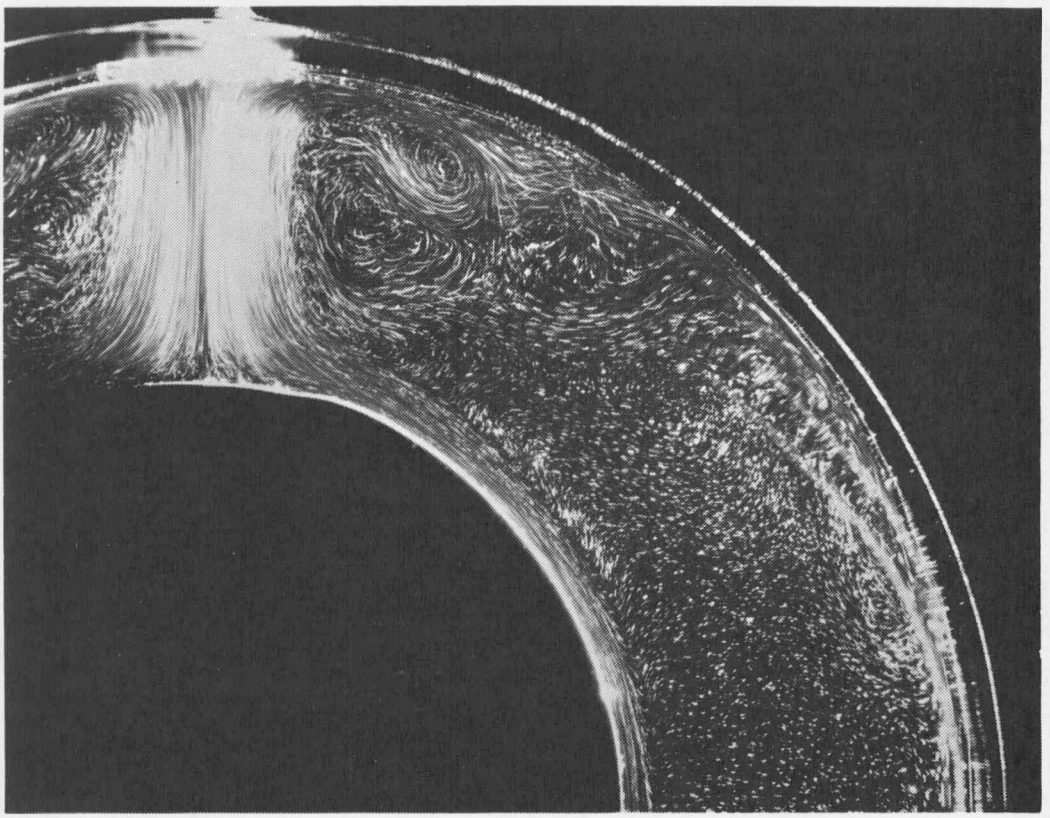


Figure 31. Tertiary Flow Pattern (Upper Portion) for

$D_o/D_i = 1.78$ $L/D_i = 0.39$

$N_{GR_L} = 1{,}688{,}000$ $N_{RA_L} = 14{,}170{,}000$

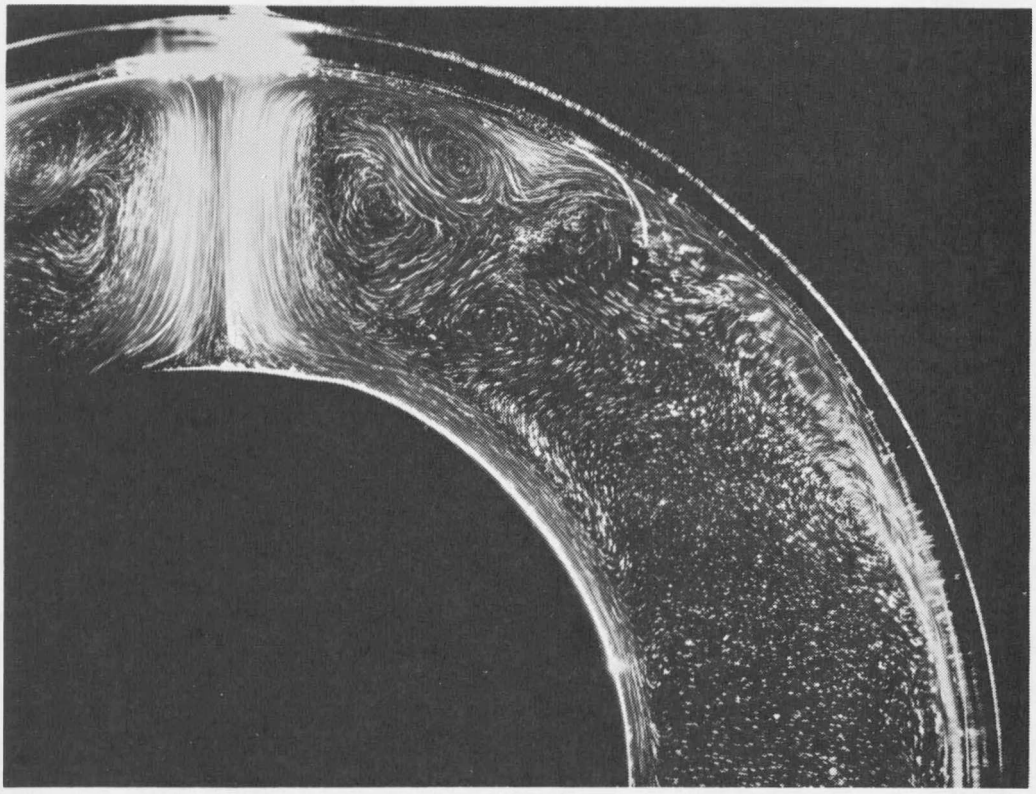


Figure 32. Tertiary Flow Pattern (Upper Portion) for

$D_o/D_i = 1.78$ $L/D_i = 0.39$

$N_{GR_L} = 1{,}688{,}000$ $N_{RA_L} = 14{,}170{,}000$

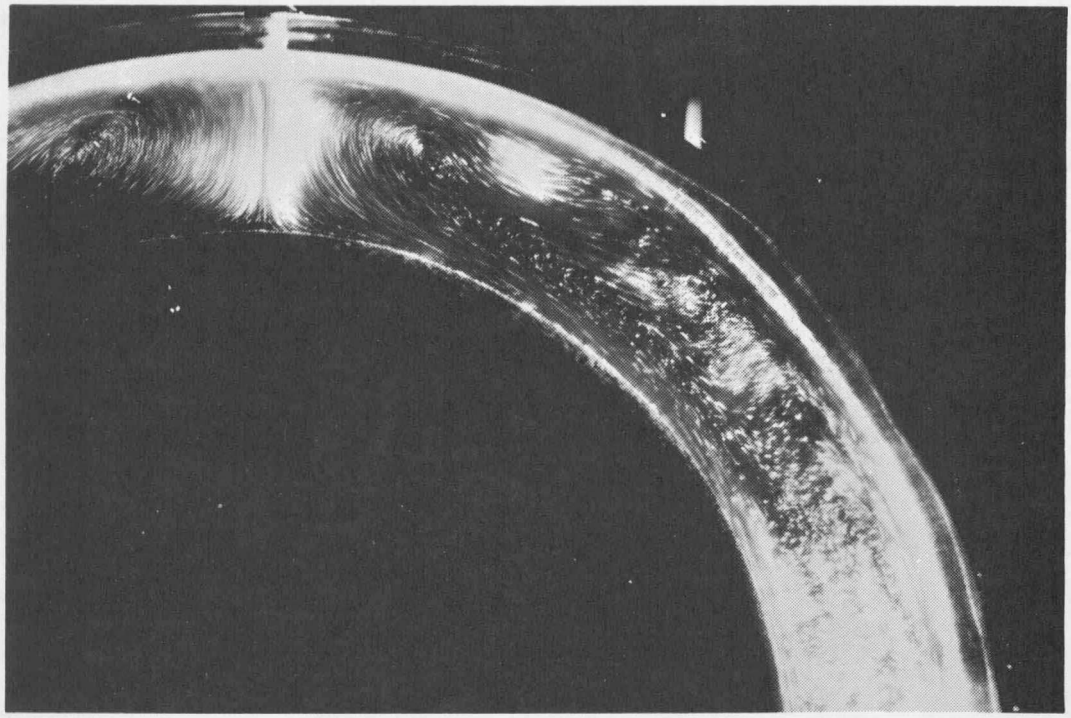


Figure 33. Steady Dog-Face Pattern (Upper Portion) for

$D_o/D_i = 1.40$ $L/D_i = 0.20$

$N_{GR_L} = 117{,}000$ $N_{RA_L} = 1{,}115{,}000$

side of the vertical axis. These two cells circulated in opposite directions, and each of them circulated in a direction opposite to the adjacent primary flow as shown in Figure 34. At this point, the major flow field of the annulus was still dominated by the dog-face pattern. The region of the opposite rotating secondary cells expanded considerably with increasing values of Grashof number. When the value of Grashof number reached 2,230,000 (N_{RA_L} = 12,850,000), a three dimensional spiral motion replaced the counter rotating secondary cells in the upper region of the gap. The fluid in this region was continually supplied by the flow separated from the upward primary flow along in the inner sphere. Meanwhile, it was observed that a continuous withdrawal of fluid from this region occurred through the portion nearest the outer sphere, and this withdrawn fluid combined with the primary flow to return to the lower portion of the annulus. This again indicated that continuity was satisfied. Only a very slight sideways oscillation in the upper region was found, and occasionally, the continuous withdrawal of fluid from the upper region was enhanced by a slug of fluid generated in the upper region. There was no definite period of occurrence for this phenomenon. The interior secondary-flow region (that is the one inside the primary flow region) was no longer stationary and a rather violent random motion was observed

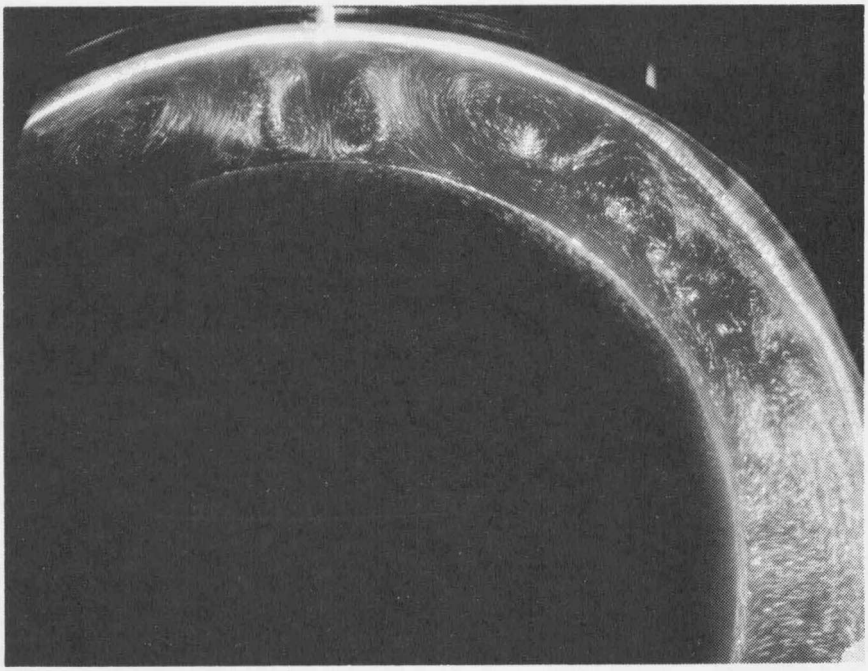


Figure 34. Photograph of Flow Pattern (Upper Portion) for

$D_o/D_i = 1.40$ $L/D_i = 0.20$

$N_{GR_L} = 1,224,000$ $N_{RA_L} = 8,322,000$

at this time. The flow reversal still appeared in the region between the high speed wall layer and the central stagnant region. No distinct dividing line could be seen in the flow field. Figure 35 illustrates the flow pattern described above. This flow pattern continued to be observed up to the maximum Grashof number of 5,455,000 (N_{RA_L} = 26,260,000) obtained using this configuration.

The last spherical configuration to be considered consisted of a 9.00 inch diameter inner sphere and a 9.77 inch diameter outer sphere resulting in a diameter ratio of 1.09 and a relative gap thickness of 0.04. No dog-face flow pattern was observed throughout the range of Grashof number obtained using this configuration, 1,720 (N_{RA_L} = 16,800) to 77,200 (N_{RA_L} = 429,200). Over this range, of Grashof number, an unsteady type of flow was found in the annulus. This unsteady flow pattern could be characterized as follows. First, the upward flow along the inner sphere was broken into two parts at an angle of about 60° measured from the upward vertical axis. Part of the fluid returned to the lower portion of the annulus along the outer sphere. The rest of the fluid flowed into the upper region with a three-dimensional spiral motion at the extreme top of the inner sphere. This entire phenomenon may occur for several minutes. Following this action, the direction of the three dimensional spiral flow in the upper portion of annulus was reversed, and then the fluid in upper portion of the annulus flowed along the inner surface

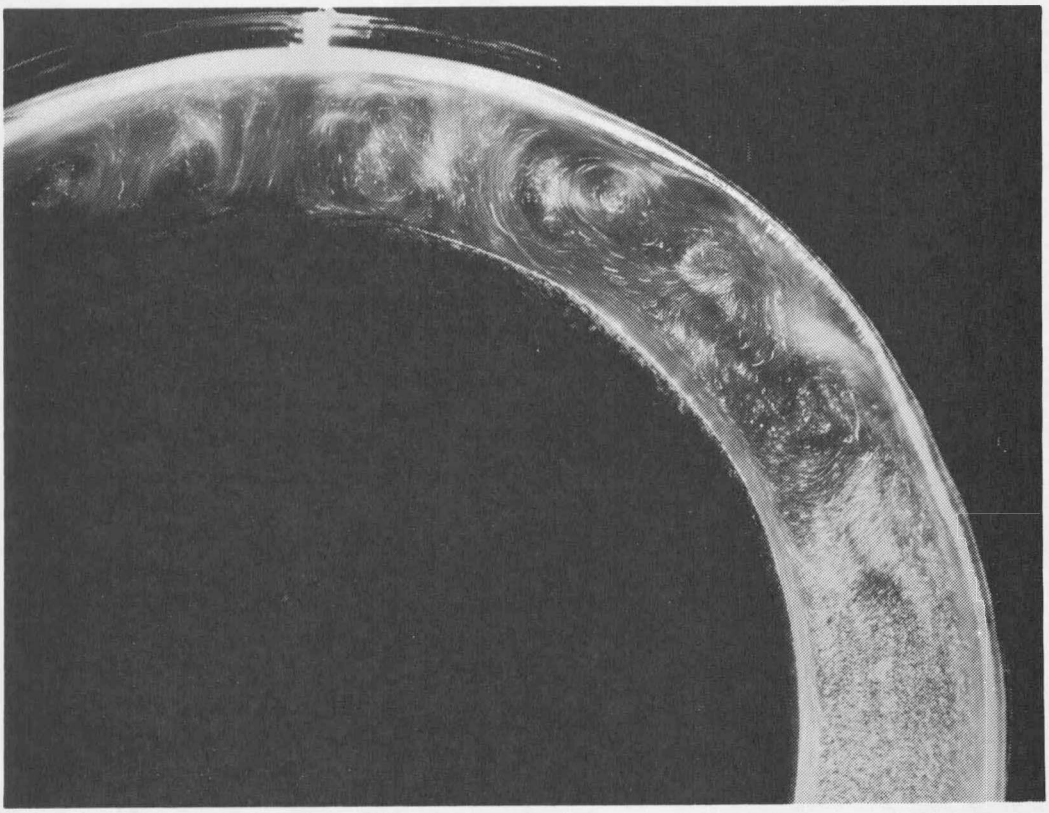


Figure 35. Three-dimensional Spiral Motion in Upper Gap Region for $D_o/D_i = 1.40$, $L/D_i = 0.20$, $N_{GR_L} = 2,497,000$ $N_{RA_L} = 14,946,000$

of the outer sphere to return to the lower portion of the annulus. During the time of changing flow direction, the extreme upper portion of the annulus appeared rather stagnant. Again, no definite period of this occurrence was observed. The period, however, did appear to be a function of the Grashof number. Usually a decreasing Grashof number led to an increasing period. The lower portion of the annulus consisted of the high speed upflow and downflow layers with a narrow interior low-speed region. A series of secondary circulations might be postulated in the thin shear layer region. Figures 36 and 37 show this flow pattern, and the particle accumulation shown in Figure 36 was due to the change of flow direction in the upper region.

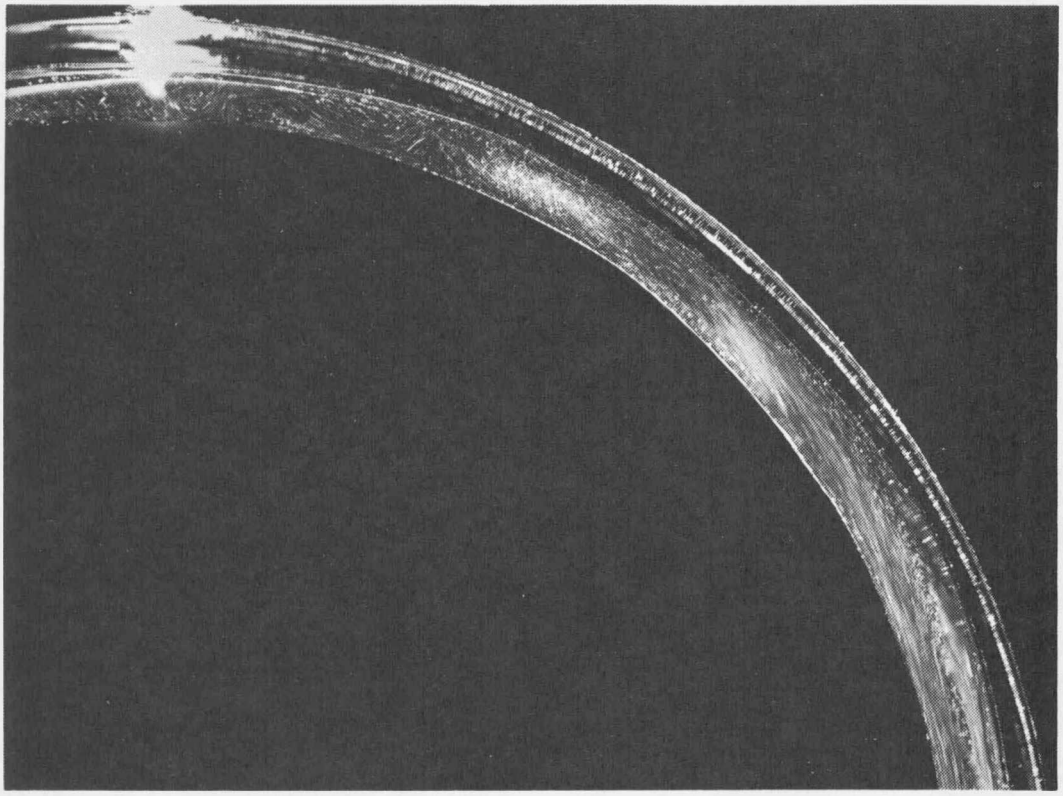


Figure 36. Photograph of Flow Pattern (Upper Portion) for

$D_o/D_i = 1.09$ $L/D_i = 0.04$

$N_{GR_L} = 1,840$ $N_{RA_L} = 18,300$

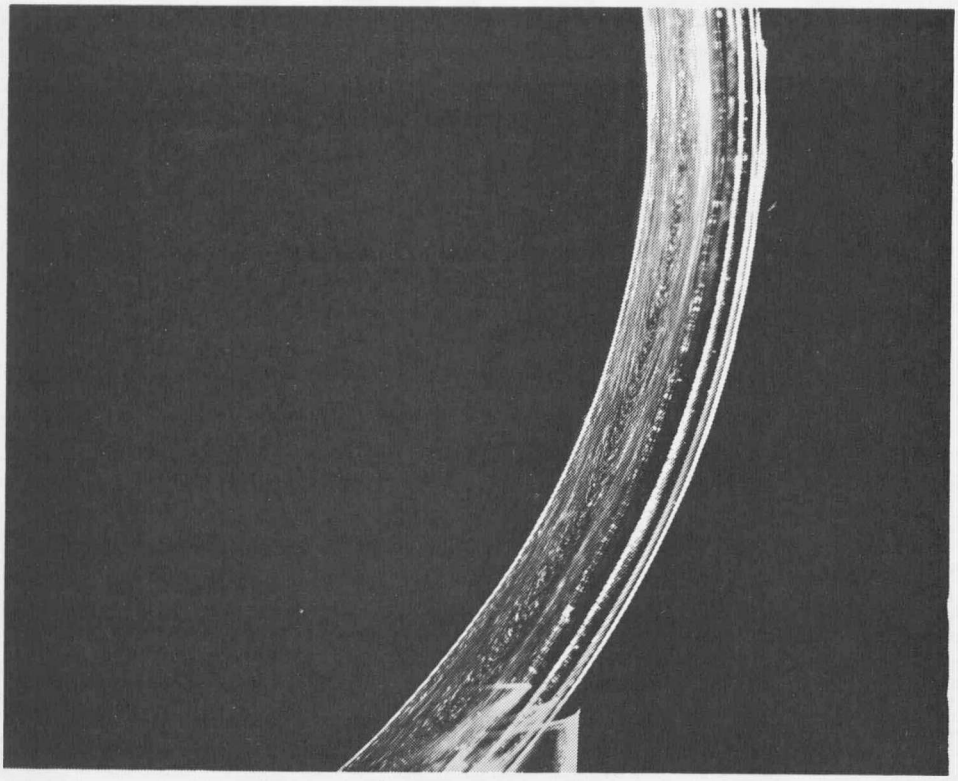


Figure 37. Photogrpah of Flow Pattern (Lower Portion) for

$D_o/D_i = 1.09$ $L/D_i = 0.04$

$N_{GR_L} = 1,840$ $N_{RA_L} = 18,300$

SUMMARY OF EXPERIMENTAL RESULTS

A brief summary of the foregoing pattern descriptions will be presented at this time. All the flow patterns observed in the current study for air as the gap working fluid can be generally classified into three distinct types of steady patterns and two types of unsteady patterns. The most common pattern, the steady crescent eddy type, occurred in all of the three tested spherical configurations with diameter ratios of 2.17 ($L/D_i = 0.59$), 1.78 ($L/D_i = 0.39$), and 1.40 ($L/D_i = 0.20$) at low Grashof numbers. This pattern was characterized by rather thin high-speed layers near the inner and outer spheres, with the flow being directed upward and downward along the inner and outer sphere respectively. The fluid in the central and major portion of this pattern moved with low speed compared to that of the above mentioned up-flow and down-flow layers. A distinct dividing line and an eddy center appeared in this pattern. The location of the pattern center was found to be a function of the spherical configuration used and the value of Grashof number. Generally speaking, the center was located above the horizontal and moved radially outward and upward in angular position for an increase in Grashof number. The second steady pattern was of the kidney-shaped eddy type. This pattern was found to appear for diameter ratios of 2.17 ($L/D_i = 0.59$) and 1.78 ($L/D_i = 0.39$)

at Grashof numbers above that at which the crescent eddy flow pattern disappeared. The primary difference between this pattern and the crescent-eddy type was the distorted shape of the central low-speed region. The last steady pattern observed was called the modified kidney-shaped eddy type and only appeared in the largest diameter ratio of 2.17 ($L/D_i = 0.59$) at high Grashof numbers. In addition to the distortion in the central low-speed reginn, a radial wave motion was also observed in this region for the modified kidney-shaped eddy pattern.

No unsteady pattern was obtained for the largest diameter ratio of 2.17 in the present study. For the diameter ratio of 1.78, an unsteady, periodic interior-contraction flow occurred as the Grashof number was increased above the transition point, N_{GR_L} = 246,000 (N_{RA_L} = 174,000). In this pattern, no distinct eddy center could be seen due to violent interior contraction motion which also caused a very slight sideways oscillation of the chimney. Another unsteady pattern, a type of three-dimensional spiral flow, was observed above the transition point, N_{GR_L} = 96,000 (N_{RA_L} = 68,000), for a diameter ratio of 1.40. The onset of the instability appeared to be near a position of about 40° measured from the upward vertical axis. In this pattern, oscillation of counter rotating cells was found to appear in the upper portion of the annulus in conjunction with a three dimensional spiral motion. The foregoing results for air as

the gap working fluid are shown in tabular form in Table 2.

For water as the gap working fluid, four distinct flow patterns, two steady and two unsteady, were observed in the present investigation. At low Grashof numbers, a common basic flow pattern, a "dog-face" type, occurred in all the spherical combinations tested except for the smallest diameter ratio. This type of flow was steady, and the flow field in the annulus was also divided into two symmetrical portions about the sphere's vertical axis. This pattern could be characterized by three distinct flow regions, namely (1) a high-speed primary-flow region, (2) an interior low-speed secondary-flow region, and (3) a central stagnant region. Certain minor changes appeared for increasing Grashof numbers. An "interior tertiary flow" pattern, in which a tertiary flow formed in the weak shear layer of two secondary cells, occurred for the diameter ratio of 1.78 ($L/D_i = 0.39$) at high Grashof numbers. The flow in this pattern was still considered to be steady.

The first unsteady pattern, an "unsteady dog-face" type, was observed at high Grashof numbers for the largest diameter ratio 2.17 ($L/D_i = 0.59$). The flow was characterized by the formation and shedding of cells in the interior secondary-flow region. Essentially the same type of unsteady pattern, the three-dimensional spiral flow, was obtained for the two smallest diameter ratios of 1.40 and 1.09 at

Table 2* Summary of Results for Air as the Gap Working Fluid

D_o		9.77"	
D_i	4.50"	5.50"	7.00"
D_o/D_i (L/D_i)	2.17 (0.59)	1.78 (0.39)	1.40 (0.20)
Type of Flow Below	$72{,}000 \leq N_{GR_L} < 166{,}500$ $51{,}000 \leq N_{RA_L} < 118{,}000$ CRESCENT EDDY	$42{,}700 \leq N_{GR_L} < 165{,}000$ $30{,}300 \leq N_{RA_L} < 117{,}000$ CRESCENT EDDY	
Transition Point	$166{,}500 \leq N_{GR_L} \leq 760{,}000$ $118{,}000 \leq N_{RA_L} \leq 535{,}000$ KIDNEY-SHAPED EDDY	$7{,}000 \leq N_{GR_L} < 96{,}000$ $4{,}950 \leq N_{RA_L} < 68{,}000$ CRESCENT EDDY	
	$165{,}000 \leq N_{GR_L} < 246{,}000$ $117{,}000 \leq N_{RA_L} < 174{,}000$ KIDNEY-SHAPED EDDY		
	$760{,}000 < N_{GR_L} \leq 1{,}156{,}000$ $535{,}000 < N_{RA_L} \leq 816{,}000$ MODIFIED KIDNEY-SHAPED EDDY		

*Continued on the following page.

Table 2. Continued

D_o/D_i (L/D_i)	2.17 (0.59)	1.78 (0.39)	1.40 (0.20)
Transition Point	No data available	N_{GR_L} = 246,000 N_{RA_L} = 174,000	N_{GR_L} = 96,000 N_{RA_L} = 68,000
Type of Flow Above Transition Point	No data available	$246,000 \leq N_{GR_L} \leq 614,000$ $174,000 \leq N_{RA_L} \leq 434,000$ PERIODIC INTERIOR CONTRACTION FLOW	$96,000 \leq N_{GR_L} \leq 120,000$ $68,000 \leq N_{RA_L} \leq 85,100$ THREE-DIMENSIONAL SPIRAL FLOW

Note: The minimum and maximum value of N_{GR_L} and N_{RA_L} in each configuration are the limiting observed values of the present investigation.

high Grashof numbers. A three-dimensional spiral type of flow instability dominated the upper portion of the annulus for this pattern. The foregoing results for water as the gap working fluid are shown in tabular form in Table 3.

Table 3.* Summary of Results for Water as the Gap Working Fluid

D_o	9.77"			
D_i	4.50"	5.50"	7.00"	9.00"
D_o/D_i (L/D_i)	2.17 (0.59)	1.78 (0.39)	1.40 (0.20)	1.09 (0.04)
Type of Flow Below Transition Point	$156{,}000 \leq N_{GR_L} < 3{,}600{,}000$ DOG-FACE TYPE $1{,}785{,}000 \leq N_{RA_L} \leq 29{,}400{,}000$ DOG-FACE TYPE	$150{,}000 \leq N_{GR_L} \leq 1{,}184{,}000$ $1{,}600{,}000 \leq N_{RA_L} \leq 10{,}350{,}000$ DOG-FACE TYPE $1{,}184{,}000 \leq N_{GR_L} \leq 5{,}530{,}000$ $10{,}350{,}000 \leq N_{RA_L} < 37{,}530{,}000$ INTERIOR TERTIARY FLOW	$58{,}500 \leq N_{GR_L} < 1{,}224{,}000$ $579{,}000 \leq N_{RA_L} \leq 8{,}322{,}000$ DOG-FACE TYPE	No data available

* Continued on the following page.

Table 3. Continued

D_o/D_i (L/D_i)	2.17 (0.59)	1.78 (0.39)	1.40 (0.20)	1.09 (0.04)
Transition point	N_{GR_L} = 3,600,000 N_{RA_L} = 29,400,000	No data available	N_{GR_L} = 1,224,000 N_{RA_L} = 8,322,000	No data available
Type of Flow Aboye Transition Point	3,600,000 $\leq N_{GR_L} \leq$ 14,200,000 29,400,000 $\leq N_{RA_L} \leq$ 92,830,000 UNSTEADY DOG-FACE TYPE	No data available	1,224,000 $\leq N_{GR_L} \leq$ 5,455,000 8,322,000 $\leq N_{RA_L} \leq$ 26,260,000 THREE-DIMENSIONAL SPIRAL FLOW	1,720 $\leq N_{GR_L} \leq$ 77,200 16,800 $\leq N_{RA_L} \leq$ 429,200 THREE-DIMENSIONAL SPIRAL FLOW

Note: The minimum and maximum value of N_{GR_L} and N_{RA_L} in each configuration are the limiting observed values of the present investigation.

DISCUSSION OF RESULTS

A comparison of the current results of flow phenomena with the existing results is presented in this section. A correlation of temperature distributions measured for water as the gap working fluid to the observed flow pattern is also presented.

Comparing the results for air as the gap working fluid with those obtained by Bishop, Mack, Kolflat, and Scanlan [1], and Bishop [28], several similarities in the flow patterns are found. Two basic steady patterns, the crescent eddy and the kidney-shaped eddy, reported by them were also observed in the present investigation. The kidney-shaped flow pattern which occurred for their largest diameter ratios of 2.53 (L/D_i = 0.77) and 3.14 (L/D_i = 1.07) was observed in the present study for diameter ratios of 2.17 (L/D_i = 0.59) and 1.78 (L/D_i = 0.39) at moderate Grashof numbers. In this pattern, a pronounced distortion of the central low-speed region occurred for an increasing Grashof number. For Grashof numbers below that at which this distortion developed sufficiently to cause a division of the central low-speed region, a continuous radial wave motion was observed in this region for the diameter ratio of 2.17 at N_{GR_L} = 760,000 (N_{RA_L} = 535,000) in the current study.

For the diameter ratio of 1.78, as the Grashof number increased above 246,000 (N_{RA_L} = 174,000), the flow was no longer steady, and a radial wave motion in conjunction with a periodic contraction motion

appeared in the central low-speed region. This might suggest that the distortion in the central low-speed region of the kidney - shaped eddy will result in the inception of an instability rather than causing a division of the pattern. In the annular configuration, the upper portion would probably be expected to be more unstable than the other regions. It is reasonable to consider the upper portion being the location of the onset of instability. However, this is not the case in the spherical annulus with a diameter ratio of 1.78 ($L/D_i = 0.39$). This might be explained in the following manner. A two-dimensional oscillating flow was obtained in concentric cylindrical annuli for diameter ratios of 1.85 ($L/D_i = 0.42$) and 2.00 ($L/D_i = 0.50$) for $N_{GR_{D_i}} = 6.6 \times 10^5$ and $N_{GR_L} = 10^5$ respectively by Powe [27] and Bishop et al [24]. In this pattern, in addition to the violent interior motion, the chimneys in adjacent vertical planes normal to the cylinder axis were observed to oscillate out of phase with each other, forming a wave motion similar to a longitudinal traveling wave. This longitudinal traveling wave motion could not occur in the spherical geometry and thus the result was the inception of instability in the central-low speed region rather than an oscillation of the chimney in the upper region of the annulus. There might be a possibility of obtaining a conical circular motion of the chimney about the sphere's vertical axis with the apex located on the inner sphere.

For low Grashof numbers, the crescent eddy pattern was observed in all tested configurations used by Bishop et al [1], Bishop [28], and the present study. No kidney-shaped eddy pattern was observed in their study for diameter ratios of 1.72 and 1.37, and this was also true for the diameter ratio of 1.40 in the current investigation. A formation of secondary cells in the extreme upper portion of the annulus was seen in this study for a diameter ratio of 1.40 at very low Grashof numbers. A bicellular flow pattern was postulated to explain the particular temperature profiles obtained for the diameter ratio of 1.25 by Bishop, Mack, and Scanlan [3]. The formation of upper secondary cells observed in the current study might suggest that there is a strong possibility of forming the bicellular flow pattern by means of an expansion of this upper secondary cell as the diameter ratio was reduced to 1.25.

The flow pattern characterized by its three-dimensional spiral nature was reported in this investigation at high Grashof numbers for the diameter ratio of 1.40 ($L/D_i = 0.4$). This pattern appears to be equivalent to the patterns described by Powe [27] in horizontal cylindrical annuli with diameter ratios of 1.4. ($L/D_i = 0.21$) and 1.6 ($L/D_i = 0.3$) at high Grashof numbers. However, the inception phenomena of the three-dimensional spiral motion was different in both studies. In his report, the formation of small secondary cells in the extreme upper portion of the annulus heralded the instability

in the form of a three-dimensional spiral motion. An earlier separation of the high speed upward flow along the inner sphere occurred in this study at $\phi = 40°$. This different inception phenomena may be considered to be due to the effect of geometrical difference. A falling-vortices type instability was reported by Bishop et al [1] and Bishop [28] for a diameter ratio of 1.19 starting at N_{RA_L} = 3,600, but this flow was two-dimensional. For the present study, the pattern center was seen to move radially outward and upward in angular position as the Grashof number was increased. The same report was given by Powe [27] in his results of an analytical method.

For water as the gap working fluid, the basic flow pattern, the steady dog-face type, was observed in the present study for all of the three largest diameter ratios of 2.17 ($L/D_i = 0.59$), 1.78 ($L/D_i = 0.39$), and 1.40 ($L/D_i = 0.20$) at low Grashof numbers. This kind of pattern has never been observed before, and it appeared to agree very well with the temperature profiles presented by Scanlan, Bishop and Powe [5]. They reported that the behavior of the temperature profiles was found to follow consistent general trends for the four largest diameter ratios of 2.81 ($L/D_i = 0.91$), 21.8 ($L/D_i = 0.59$), 1.79 ($L/D_i = 0.40$), and 1.40 ($L/D_i = 0.20$). They also pointed out that the form of the dimensionless temperature profiles was found to be independent of ΔT for a given diameter ratio and test fluid when the Prandtl number remained essentially constant, or the

variations of Prandtl number were less than the order of 15 percent. A typical temperature profile for water as the gap fluid at N_{GR_L} = 1,215,000 (N_{RA_L} = 7,923,000) for a diameter ratio of 1.40 was presented by them and is shown in Figure 38. The corresponding flow pattern under this condition is the steady dog-face type. A schematic sketch of this pattern is given in Figure 39, and a photograph of this pattern can also be found in Figure 33.

Each temperature profile has five characteristic regions defined in the same manner as in Bishop *et al* [3] and Scanlan *et al* [5]. The first region is characterized by a very steep temperature gradient in the region very near to the wall of the inner sphere. This region corresponds to the high-speed primary flow region along the inner sphere resulting in a high rate of heat convection through this thin layer. The second region, an inner-sphere curvature region, joins this steep gradient region to one with a very flat gradient. This region is considered as the transition region between the high-speed layer along the inner-sphere and the central stagnant region. The third region is one of a very flat temperature gradient. However, this is true only at ϕ = 0°, 120° and 160° and an inversion appears in this region for ϕ = 40° and 80°. For ϕ = 120° and 160°, this flat temperature gradient region is due to the effect of the central stagnant region in which conduction dominates the heat transfer rate. The unique shape of the profile in this region at ϕ = 0° can be

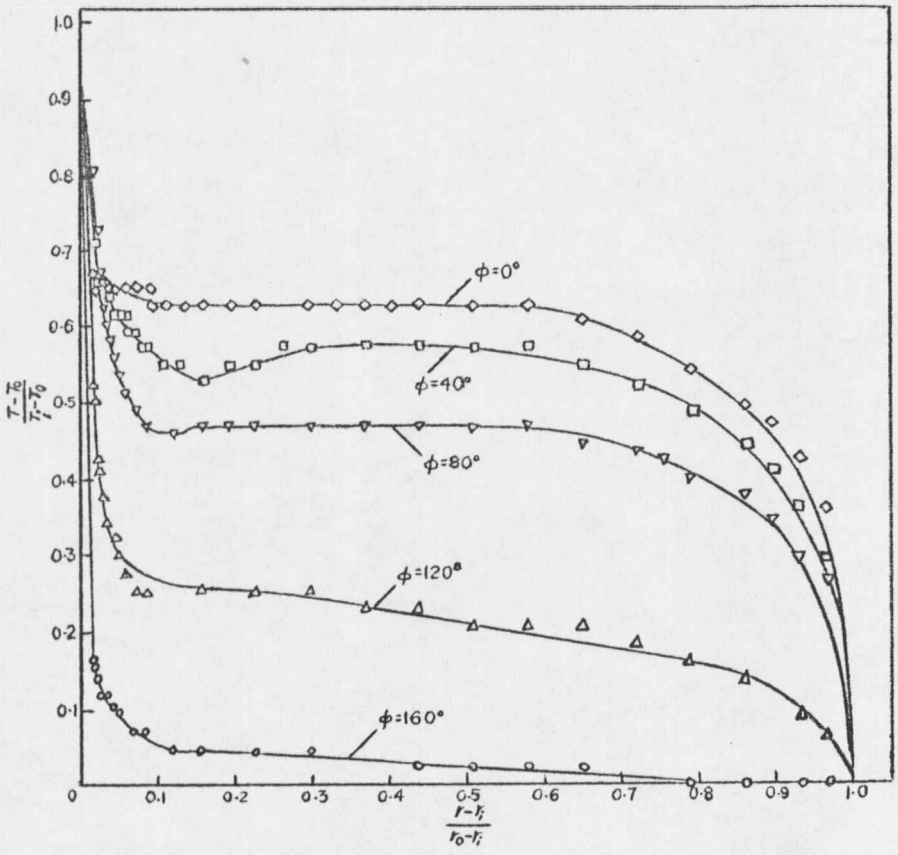


Figure 38. Temperature Profiles for Water, D_o/D_i = 1.40, L/D_i = 0.20, N_{GR_L} = 1,217,000, N_{RA_L} = 7,923,000

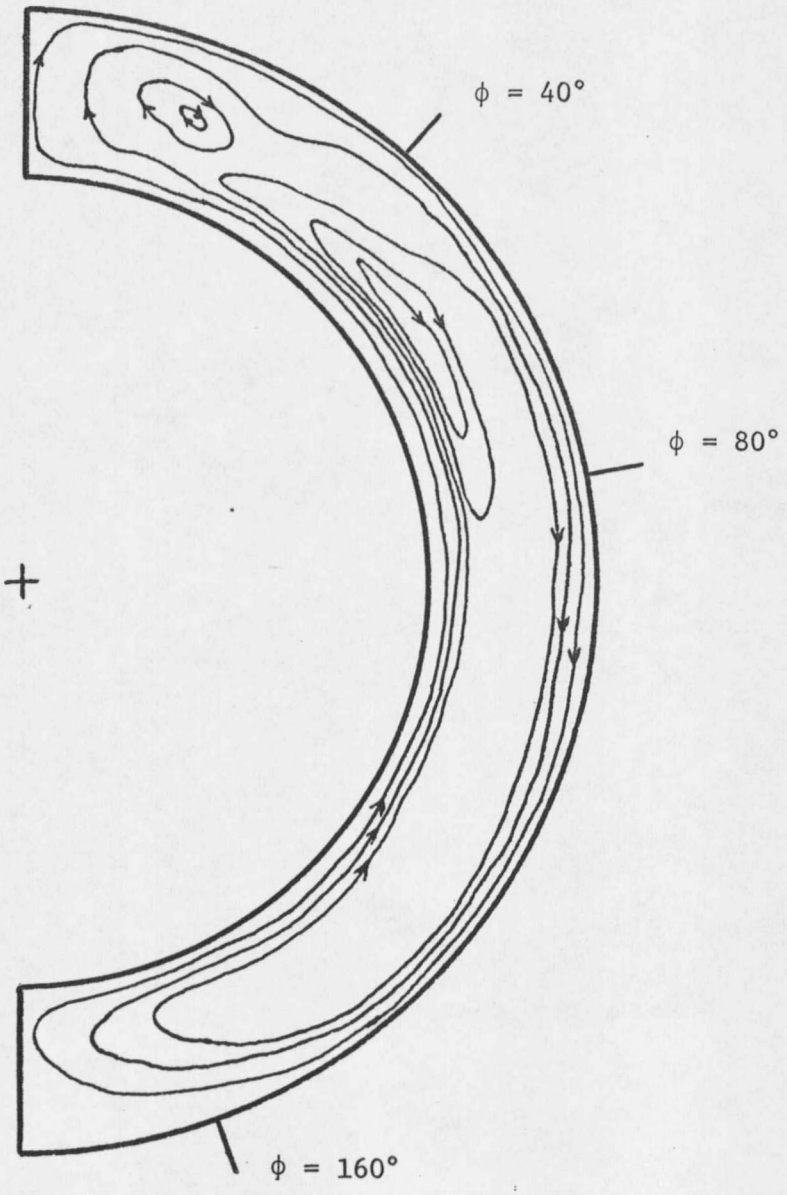


Figure 39. Sketch of Steady Dog-Face Pattern
For $D_o/D_i = 1.40$, $L/D_i = 0.20$
$N_{GR_L} = 1{,}217{,}000$, $N_{RA_L} = 7{,}923{,}000$

explained by postulating the existence of a corner eddy as described by Bishop et al [3]. The inversion regions in the temperature profile at $\phi = 40°$ and $80°$ can be explained in the following manner. By referring to Figure 39, the inversion regions appear to be in the interior secondary flow region of the flow field. The heat transfer rate in these inversion regions is dominated by the high rate of angular convection of heat due to the secondary circulation motion relative to conduction of heat in the radial direction. The secondary flow is more prevalent at $\phi = 40°$ than at $\phi = 80°$ and this causes a more pronounced inversion at $\phi = 40°$ than at $80°$. Another transition region between the central stagnant region and the high-speed downward primary-flow region adjacent to the outer sphere yields the fourth region, the outer-sphere curvature region, in the temperature profile. The fifth and final region of the temperature profile is another steep temperature gradient adjacent to the outer sphere. This indicates that heat convection again becomes more prevalent in this region due to the high-speed primary flow along the outer sphere.

No interior secondary flow was obtained by Liu, Mueller, and Landis [18] for concentric cylinders using water as the gap fluid. However, a similar secondary flow was observed by Elder [14] in his study of a vertical slot utilizing both medicinal paraffin and silicone oil MS 200/100 centistoke as the gap fluid. He reported

that the steady secondary flow was generated in the interior region of the flow near $N_{RA_L} = 10^5$ and near $N_{RA_L} = 10^6$ when the secondary cell amplitude was large. A further steady cellular motion, to be called tertiary flow, was generated in the weak shear region between each cell. In the present study, a tertiary flow was first obtained at $N_{RA_L} = 10^7$ for a diameter ratio of 1.78. Furthermore, a small flow reversal in the region adjacent to the vertical high-speed wall layers was observed by Elder for H/L = 7.16 at $N_{RA_L} = 3.61 \times 10^5$. A similar phenomenon of a small flow reversal appearing in the region between the high-speed wall layer and the central stagnant region was seen in this study for a diameter ratio of 1.40 ($D_o/L = 9.77$) above the minimum observable value of $N_{RA_L} = 579{,}000$.

In the current investigation, no steady pattern was observed for the smallest diameter ratio of 1.09 even at the minimum observable value of $N_{GR_L} = 1{,}720$ ($N_{RA_L} = 16{,}800$). This is thought to be due to the small gap thickness geometrical effects which become predominant. Here the top section acts like a "fluid heated from below" between parallel plates where cellular instabilities arise at values of N_{RA_L} between 1,600 and 2,000 which are much lower than the value of $N_{RA_L} = 16{,}800$.

CHAPTER V

CONCLUSIONS AND RECOMMENDATIONS

An apparatus for studying the characteristics of natural convective flows between isothermal concentric spheres with different diameter ratios and using different test fluids was designed and constructed. In this investigation, the existing data of Bishop et al [1] was extended to a higher impressed temperature difference with air as the working fluid, and an initial study with water as the gap fluid was also established. The objectives of this experimental investigation were (1) to obtain criteria for prediction of the fluid-flow behavior, (2) to study the mechanism which determines when and how the onset of instability in the flow field occurs, and (3) to correlate the existing temperature profiles with the flow phenomena obtained.

In order to obtain the visualization of the flow patterns, a different visualization technique was utilized for each test fluid. A special visualization technique was developed for water as the working fluid in the current investigation. The visualization of the flow pattern in this case was accomplished by introducing a well mixed and prepared solution of distilled water with a very minute amount of liquid "Ajax" detergent into the annulus and transversely illuminating the major diameter. For air in the gap an injection of tobacco (cigar) smoke into the annulus was employed. A qualitative description of the flow patterns obtained for each set of spherical

combinations studied is presented. These descriptions are supported by still photographs and a few sketches. Motion pictures of each distinctive type of flow pattern found to occur in this investigation were also obtained, and since they could not be presented in this dissertation, they are being placed on file with the Aerospace and Mechanical Engineering Department at Montana State University for reference purposes.

All the flow patterns observed in the current study for air as the working fluid were generally classified into three distinct types of steady patterns and two types of unsteady patterns. The flow patterns at lower Grashof numbers qualitatively agree with those obtained by Bishop et al [1] and Bishop [28]. The inception of the instabilities characterized by periodic interior contractions or three-dimensional spiral flow in the spherical annuli was compared to the case of horizontal cylindrical annuli.

The most common basic flow pattern with water as the gap fluid, the steady dog-face type, appeared in the three largest diameter ratios investigated. This flow pattern is characterized by three distinct regions: (1) a high speed primary-flow region, (2) an interior low speed secondary-flow region, and (3) a central stagnant region. This kind of pattern had never previously been observed. The temperature profiles obtained in the heat transfer study of Scanlan, Bishop, and Powe [5] correlate quite well with this basic flow pattern from visual

observation of the flow. In addition to the appearence of interior secondary cells, a formation of tertiary flow in the weak shear layer between two secondary cells occurred for the diameter ratio of 1.78 ($L/D_i = 0.39$) at high Grashof numbers. This tertiary type flow might be thought of as the herald of the unsteady disturbances and the subsequent expected turbulent flow for those spherical configurations with larger diameter ratios. As the Grashof number was increased over certain transition points, an unsteady dog-face type flow, or a three-dimensional spiral flow, was obtained.

No attempt was made to reach any generalized conclusions regarding the effects of Prandtl number on the flow phenomena in the spherical configuration. However, the values of Rayleigh number leading to the flow instabilities for water appeared to be higher than those obtained for air.

RECOMMENDATIONS FOR FUTURE WORK

Before a complete plot which allows prediction of the type of unsteady flow that will occur for a wide range of spherical combinations and annulus operating conditions can be obtained for each test fluid, more sets of spherical configurations should be investigated.

It is also recommended that the range of Prandtl number for each D_o/D_i studied in this investigation be extended, resulting in a

greater understanding of the effect of Prandtl number on the flow phenomena.

APPENDIX I

GOVERNING DIFFERENTIAL EQUATIONS

Under appropriate assumptions, the mathematical model for the flow process resulting from the density change caused by a temperature gradient within the gravitational force field between concentric isothermal spheres can be obtained.

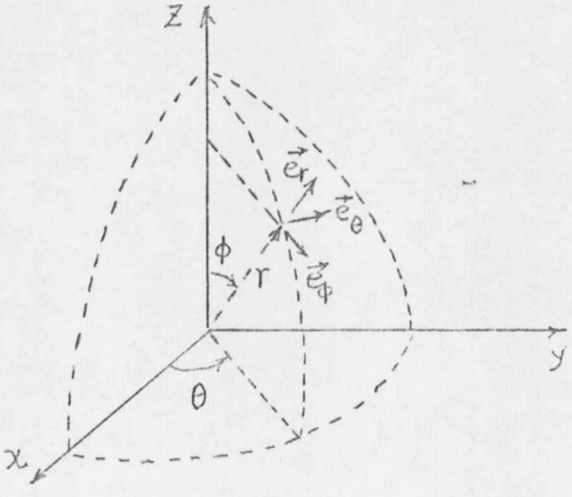
Assumptions:

(1) Constant fluid properties except in the formation of the buoyancy term. This is based on the assumption that the temperature difference ΔT is small compared with the absolute temperature of the cold boundary.

(2) Compressibility effects and viscous dissipation can be neglected. This is due to the fact that the fluid velocities associated with this flow process are generally low.

(3) The flow is Newtonian. (Note: air and water were used as gap working fluid in the present investigation. This assumption is also acceptable.)

Coordinate System:



Mathematical Model:

(1) Continuity Equation:

$$\frac{1}{r^2}\frac{\partial}{\partial r}(\rho r^2 V_r) + \frac{1}{r\sin\phi}\frac{\partial}{\partial \phi}(\rho V_\phi \sin\phi) + \frac{1}{r\sin\phi}\frac{\partial}{\partial \theta}(\rho V_\theta) = 0 \qquad (1)$$

(2) Conservation of Momentum Equations:

r - direction

$$\rho\left(\frac{\partial V_r}{\partial t} + V_r\frac{\partial V_r}{\partial r} + \frac{V_\phi}{r}\frac{\partial V_r}{\partial \phi} + \frac{V_\theta}{r\sin\phi}\frac{\partial V_r}{\partial \theta} - \frac{V_\phi^2 + V_\theta^2}{r}\right) = -\frac{\partial P}{\partial r} + \mu\left[\nabla^2 V_r - \frac{2}{r^2}V_r - \frac{2}{r^2}\frac{\partial V_\phi}{\partial \phi} - \frac{2}{r^2}V_\phi\cot\phi - \frac{2}{r^2\sin\phi}\frac{\partial V_\theta}{\partial \theta}\right] - [\rho - \rho\beta(T - \bar{T})]g\cos\phi \qquad (2)$$

ϕ - direction

$$\rho\left(\frac{\partial V_\phi}{\partial t} + V_r\frac{\partial V_\phi}{\partial r} + \frac{V_\phi}{r}\frac{\partial V_\phi}{\partial \phi} + \frac{V_\theta}{r\sin\phi}\frac{\partial V_\phi}{\partial \theta} + \frac{V_r V_\phi}{r} - \frac{V_\theta^2\cot\phi}{r}\right) = -\frac{1}{r}\frac{\partial P}{\partial \phi} + \mu\left[\nabla^2 V_\phi + \frac{2}{r^2}\frac{\partial V_r}{\partial \phi} - \frac{V_\phi}{r^2\sin^2\phi} - \frac{2\cos\phi}{r^2\sin^2\phi}\frac{\partial V_\theta}{\partial \theta}\right] + [\rho - \rho\beta(T - \bar{T})]\,g\sin\phi \qquad (3)$$

θ - direction

$$\rho\left(\frac{\partial V_\theta}{\partial t} + V_r\frac{\partial V_\theta}{\partial r} + \frac{V_\phi}{r}\frac{\partial V_\phi}{\partial \phi} + \frac{V_\theta}{r\sin\phi}\frac{\partial V_\theta}{\partial \theta} + \frac{V_\theta V_r}{r} + \frac{V_\phi V_\theta}{r}\cot\phi\right) = -\frac{1}{r\sin\phi}\frac{\partial P}{\partial \theta} + \mu\left[\nabla^2 V_\theta - \frac{V_\theta}{r^2\sin^2\phi} + \frac{2}{r^2\sin\phi}\frac{\partial V_r}{\partial \theta} + \frac{2\cos\phi}{r^2\sin^2\phi}\frac{\partial V_\phi}{\partial \theta}\right] \quad (4)$$

where

$$\nabla^2 = \frac{1}{r^2}\frac{\partial}{\partial r}\left(r^2\frac{\partial}{\partial r}\right) + \frac{1}{r^2\sin\phi}\frac{\partial}{\partial \phi}\left(\sin\phi\frac{\partial}{\partial \phi}\right) + \frac{1}{r^2\sin^2\phi}\left(\frac{\partial^2}{\partial \theta^2}\right)$$

$\overline{T}$ = an unspecified mean temperature

(3) Conservation of Energy Equation

$$\rho C_p\left(\frac{\partial T}{\partial t} + V_r\frac{\partial T}{\partial r} + \frac{V_\phi}{r}\frac{\partial T}{\partial \phi} + \frac{V_\theta}{r\sin\phi}\frac{\partial T}{\partial \theta}\right) = k\left[\frac{1}{r^2}\frac{\partial}{\partial r}\left(r^2\frac{\partial T}{\partial r}\right) + \frac{1}{r^2\sin\phi}\frac{\partial}{\partial \phi}\left(\sin\phi\frac{\partial T}{\partial \phi}\right) + \frac{1}{r^2\sin^2\phi}\frac{\partial^2 T}{\partial \theta^2}\right] \quad (5)$$

Subject to

(i) Fixed boundary conditions of T, V_r, V_ϕ and V_θ.

$T = T_i$, $V_r = V_\phi = V_\theta = 0$, at $r = r_i$

$$T = T_o, \quad V_r = V_\phi = V_\theta = 0, \quad \text{at } r = r_o$$

(ii) Undetermined boundary conditions of T, V_r, V_ϕ and V_θ associated with ϕ - direction, θ - direction, and time (t).

(iii) Undetermined boundary conditions of Pressure (P) associated with r - direction, ϕ - direction and θ - direction.

APPENDIX II

EQUIPMENT LIST

1. DC Millivoltmeter – Model No. 251-3, Serial No. 9493; Manufactured by United System Corporation; Dayton, Ohio.
2. Digitest – Model 333, Serial 7299; manufactured by Honeywell; Denver, Colorado.
3. Variac Autotransformer – Type W 20 MT 3; 120 Volt, 50-60 cycle line; 0-140 Volt, 20 Amps load; manufactured by General Radio Company; Concord, Massachusetts.
4. Powerstate Variable Autotransformer – Model GP 58004; 0-100 Volt; manufactured by the Superior Electric Corporation; Bristol, Connecticut.
5. Freon Pressure Gauge – 0-30 inches Mercury, 0-300 psig; manufactured by Ashcroft Corporation.
6. Water Pressure Gauge – 0-20 psig, 1/4 psi/div; manufactured by U. S. Gauge Corporation.
7. ISD Thermocouple Reference Junction – Model No. BRJ 18-24-TT, Serial No. 525044, Ref. Temp. 32°F, 115 Volt; manufactured by Whittaker Corporation.
8. Spencer Turbo-Compressor – Lot No. 24980, Serial No. 51021; 12 CFM, 115 Volt, 9 Amp 7,000 RPM; manufactured by the Spencer Turbine Company.
9. Dehydrating Compressor Unit – Type CPD-10137, Serial 306; Input 115/1/60, 7.7 Amp; manufactured by Communication Products Corporation.

10. Thermocouple Selector Switch - Manufactured by Honeywell Regulator Corporation; Minneapolis, Minnesota.
11. Water Chiller unit - Manufactured by Watts Manufacturing Company; Ronceverte, West Virginia.
12. Pioneer Pump - Model H10 FE, 115 Volt, Single Phase, 60 cycle; manufactured by Detroit Harvester Corporation.
13. Water Filter - Model P 10-1, Catalog No. 55310-01 Max. pressure 125 psi, Max. Temp. 100°F; Manufactured by American Machine & Foundry Company.
14. Light Source - Cameralit Model No. 91, use with DWA 92 lamp; 120 volt, 650 Watts; Manufactured by ACME-LITE Manufacturing Corporation; Chicago, Illinois.
15. Fans - Service No. 5062369; 115 Volt, 0.5 Amps, Manufactured by General Motor Corporation.
16. Timer - Model SC-100, 115 Volt; manufactured by Industrial Timer Corporation; Parsippang, New Jersey.
17. 4x5" View Camera - Serial 20630; manufactured by Calumet Photographic Inc.; Elk Grov Village, Illinois.
18. Movie Camera - Beaulieu R 16 "Automatic", Serial No. 665-180, 16 mm; Manufactured by Cinema.

APPENDIX III

COMPUTER PROGRAMS

The computer program presented herein was written for calculating the required dimensionless parameters from the recorded data for both concentric spheres and eccentric spheres. This program included function subprograms for the reduction of thermocouple data and determination of thermal and physical properties of water as the gap working fluid. A sample of its results is also given. The input variables for this program are defined in the following manner.

O	Observation number
DS	Diameter of inner sphere, inches
DL	Diameter of outer sphere, inches
EC	Eccentricity, inches
E(I)	Voltage reading of i th thermocouple, millivolts

This computer program has the following function subprograms:

(1) FUNCTION T(E) Convert millivolt readings for thermocouples to temperature (°R)

(2) FUNCTION U(T) Calculates the absolute viscosity (lb_m/hr-ft) of water as a function of temperature (°R)

(3) FUNCTION CP(T) Calculates the specific heat (BTU/lb_m-°R) at a constant pressure for water as a function of temperature (°R)

(4) FUNCTION CON(T) Calculates the thermal conductivity (BTU/ft-hr-°R) of water as a function of temperature (°R)

(5) FUNCTION RHOA(T) Calculates the density (lb_m/ft^3) of water as function of temperature (°R)

(6) FUNCTION BETAA(T) Calculates the expansion coefficient (1/°R) for water as a function of temperature (°R)

```
      DIMENSION E(15), TE(15)
   25 READ (105,1),θ,DS, DL, EC
    1 FORMAT (4F10.4)
      IF (θ) 5, 5, 6
    6 WRITE (108,2) θ,EC
    2 FORMAT ('1 θBSERVATIθN Nθ,' F4.2,12X, 'ECCENTRICITY=' E15.8)
      WRITE (108,111)
  111 FORMAT ('0'16X,'FLUID IN GAP IS WATER')
      X1 = (EC + DS/2.0)/(DL/2.0)
      X2 = (EC - DS/2.0)/(DL/2.0)
      RO = (1.0 - X1*X2 +((1.0 -X1*X1)*(1.0 - X2**2))**0.5)/(X1 -X2)
      DSM = DL/RO
      GAPM = (DL - DSM)/2.0
      DRTM = DL/DSM
      GRTM = GAPM/DSM
      GAP = (DL - DS)/2.0
      DRT = DL/DS
      GRT = GAP/DS
      WRITE (108,3) DS, DL, DRT
    3 FORMAT ('0 INNER DIA = 'F8.4,', θUTER DIA = 'F8.4,', DIA RATIθ = 'F8.
     14)
      WRITE (108,4) GAP, GRT
    4 FORMAT ('0 GAP THICKNESS = 'F8.4,15X,'RELATIVE GAP ='F8.4)
      WRITE (108,50)GAPM, GRTM
   50 FORMAT ('0 MAPPED GAP =' E15.8,5X,'MAPPED RELATIVE GAP ='E15.8)
      WRITE (108,80) DRTM
   80 FORMAT ('0 MAPPED DIAMETER RATIθ='E15.8)
      READ (105,9)  (E(I), I = 1,8)
    9 FORMAT (4F10.4)
      TθT = 0.0
      Dθ 10    I = 1,2
      TE(I) = T(E(I))
   10 TθT = TθT + TE(I)
      TS = TθT/2.0
```

```
      TOT = 0.0
      DO 11   I = 3,8
      TE(I) = T(E(I))
   11 TOT = TOT + TE(I)
      TL = TOT/6.0
      WRITE (108,12)
   12 FORMAT ('0'16X,'TEMPERATURE DISTRIBUTIONS')
      WRITE (108,16)
   16 FORMAT ('0',1X,'THERMOCOUPLE'3X,'TEMPERATURE'5X,'DEVIATION'3X,'% D
     1EVIATION')
      WRITE (108,13)
   13 FORMAT ('0'21X,'INNER SPHERE')
      DO 14   I = 1,2
      DEV = TE(I) - TS
      DEVP = DEV*100.0/TS
   14 WRITE (108,15) I, TE(I), DEV, DEVP
   15 FORMAT(I14,3F14.4)
      WRITE (108,17)
   17 FORMAT ('0'21X, 'OUTER SPHERE')
      DO 18   I = 3, 8
      DEV = TE(I) - TL
      DEVP = DEV*100.0/TL
   18 WRITE (108,15) I, TE(I), DEV, DEVP
      DT = TS - TL
      LMN = 0
  100 LMN = LMN + 1
      IF (LMN - 1) 51, 51, 52
   51 TM = (TS + TL)/2.0
      WRITE (108,55)
   55 FORMAT ('0'30X,'BASED ON ARITHMETIC MEAN TEMPERATURE')
      GO TO 53
   52 RAVG = (DL + DSM)/4.0
      RAVG3 = RAVG**3
      RL3 = DL**3/8.0
```

```
      RS3 = DSM**3/8.0
      TM=((RAVG3-RS3)*TS+(RL3-RAVG3)*TL)/(RL3-RS3)
      GAP = GAPM
      DS = DSM
      WRITE (108,56)
   56 FORMAT ('0',30X,'BASED ON VOLUME WEIGHTED MEAN TEMPERATURE (MAPPED
     1)')
   53 VIS = U(TM)
      SH = CP(TM)
      COND=CON(TM)
      BETA=BETAA(TM)
      RHO=RHOA(TM)
      WRITE (108,19)  TS,TL
   19 FORMAT ('0 INNER TEMP = 'F6.2,5X,'Outer TEMP ='F6.2)
      WRITE (108,20) TM, DT
   20 FORMAT ('MEAN TEMP = 'F6.2,6X,'TEMP DIFF ='F6.2)
      WRITE (108,21) VIS, SH
   21 FORMAT ('0 VISCOSITY ='F6.4,9X,'SPECIFIC HEAT ='F6.4)
      WRITE (108,40) COND, RHO
   40 FORMAT ('CONDUCTIVITY =' F6.4,6X,'DENSITY ='F7.4)
      WRITE (108,22) BETA
   22 FORMAT ('EXPANSION COEFF = 'E15.8)
      GR= (32.174*BETA*DT*GAP/1728.0)*(RHO*GAP *3600.0/VIS)**2
      PR = VIS*SH/COND
      RA = GR*PR
      WRITE (108,41)
   41 FORMAT ('0'7X,'GRASHOF NO'8X,'PRANDTL NO'7X,'RAYLEIGH NO')
      WRITE (108,26)
   26 FORMAT ('0'17X,'BASED ON GAP THICKNESS')
      WRITE (108,23) GR, PR, RA
   23 FORMAT (3X,E15.8,3X,E15.8,3X,E15.8)
      WRITE(108,27)
   27FORMAT ('0'19X,'BASED ON INNER DIA')
      GR = (32.174*BETA*DT*DS/1728.0)*(RHO*DS*3600.0/VIS)**2
```

```
      RA=GR*PR
      WRITE (108,23) GR,PR,RA
      WRITE (108,30)
   30 FORMAT ('0'18X,'BASED ON INNER RADIUS')
      DS = DS/2.0
      GR = (32.174*BETA*DT*DS/1728.0)*(RHO*DS*3600.0/VIS)**2
      RA=GR*PR
      WRITE (108,23) GR, PR, RA
      IF (LMN - 2) 100, 101, 101
  101 GO TO 25
    5 CONTINUE
      CALL EXIT
      END
```

SUBPROGRAMS

```
      FUNCTION T(E)
      DIMENSION C(8)
      DOUBLE PRECISION TOT
      C(1) = 491.96562
      C(2) = 46.381884
      C(3) = -1.3918864
      C(4) = 0.15260798
      C(5) = -0.020201612
      C(6) = 0.0016456956
      C(7) = -6.6287090/(10.0**5)
      C(8) = 1.0241343/(10.0**6)
      TOT = 0.0
      DO 1 I = 1,8
    1 TOT = TOT + C(I)*E**(I - 1)
      T = TOT
      RETURN
      END
```

```
      FUNCTION U(T)
      TP=T-593.33203
      C1=.0071695149
      C2=.011751302
      C3=.0087791942
      C4=.81654704
      VIS=C1*TP+C2*(1.+C3*(TP**2))**.5+C4
      U=1./VIS
      RETURN
      END


      FUNCTION CP(T)
      C1=1.3757095
      C2=.0012968965
      C3=1.1110533/(10.**6)
      CP=C1-(C2-C3*T)*T
      RETURN
      END

      FUNCTION CON(T)
      C1=.23705417
      C2=.0017156797
      C3=1.1563770/(10.**6)
      CON=-C1+(C2-C3*T)*T
      RETURN
      END
```

```
      FUNCTION RHOA(T)
      C1=52.754684
      C2=.045437533
      C3=5.1832336/(10.**5)
      RHOA=C1+(C2-C3*T)*T
      RETURN
      END


      FUNCTION BETAA (T)
      TP=T/100.
      IF (T-549.59) 1,1,2
    1 C1=603.11841
      C2=-353.03882
      C3=68.297012
      C4=-4.3611460
      BP=C1+(C2+(C3+C4*TP)*TP)*TP
      GO TO  3
    2 C1=-128.44920
      C2=68.827927
      C3=-13.858489
      C4=1.2608585
      C5=-.042495236
      BP=C1+(C2+(C3+(C4+C5*TP)*TP)*TP)*TP
    3 BETAA=BP/(10.**4)
      RETURN
      END
```

SAMPLE RESULTS FROM PRECEDING PROGRAM

OBSERVATION NO,8.01 ECCENTRICITY= .00000000E+00

FLUID IN GAP IS WATER

INNER DIA = 5.50000, OUTER DIA = 9.7700, DIA RATIO = 1.7764

GAP THICKNESS = 2.1350 RELATIVE GAP = .3882

MAPPED GAP = .21349993E+01 MAPPED RELATIVE GAP = .38818157E+00

MAPPED DIAMETER RATIO= .17763634E+01

TEMPERATURE DISTRIBUTIONS

THERMOCOUPLE	TEMPERATURE	DEVIATION	%DEVIATION
	INNER SPHERE		
1	508.4895	-.2271	-.0446
2	508.9436	.2271	.0446
	OUTER SPHERE		
3	503.0190	.1526	.0303
4	503.0190	.1526	.0303
5	502.5615	-.3049	-.0606
6	503.0190	.1526	.0303
7	503.0190	.1526	.0303
8	502.5615	-.3049	-.0606

BASED ON ARITHMETIC MEAN TEMPERATURE

INNER TEMP = 508.72 OUTER TEMP =502.87
MEAN TEMP = 505.79 TEMP DIFF = 5.85

VISCOSITY =3.4962 SPECIFIC HEAT = 1.0040
CONDUCTIVITY = .3349 DENSITY =62.4766
EXPANSION COEFF = .38012688E-04

GRASHOF NO	PRANDTL NO	RAYLEIGH NO
BASED ON GAP THICKNESS		
.66766131E+06	.10481361E+02	.17478850E+07
BASED ON INNER DIA		
.28509430E+07	.10481361E+02	.29881760E+08
BASED ON INNER RADIUS		
.35636881E+06	.10481361E+02	.37352300E+07

BASED ON VOLUME WEIGHTED MEAN TEMPERATURE (MAPPED)

INNER TEMP = 508.72 OUTER TEMP =502.87
MEAN TEMP = 504.99 TEMP DIFF = 5.85

VISCOSITY =3.5564 SPECIFIC HEAT =1.0041
CONDUCTIVITY = .3345 DENSITY =62.4821
EXPANSION COEFF = .35522447E-04

GRASHOF NO	PRANDTL NO	RAYLEIGH NO
BASED ON GAP THICKNESS		
.15062825E+06	.10677341E+02	.16083090E+07
BASED ON INNER DIA		
.25751370E+07	.10677341E+02	.27495616E+08
BASED ON INNER RADIUS		
.32189300E+06	.10677341E+02	.34369610E+07

BIBLIOGRAPHY

1. Bishop, E. H., Kolflat, R. S., Mack, L. R., and Scanlan, J. A., "Convective Heat Transfer between Concentric Spheres," Proceedings of the 1964 Heat Transfer and Fluid Mechanics Institute, Stanford University Press, pp. 69-80, 1964.

2. Bishop, E. H., Kolflat, R. S., Mack, L. R., and Scanlan, J. A., "Photographic Studies of Convection Patterns between Concentric Spheres," Society of Photo-Optical Instrumentation Engineers Journal, 3, pp. 47-49, 1964-1965.

3. Bishop, E. H., Mack, L. R., and Scanlan, J. A.,"Heat Transfer by Natural Convection between Concentric Spheres," International Journal of Heat and Mass Transfer, 9, pp. 649-662, 1966.

4. Mack, L. R., and Hardee, H. C., "Natural Convection between Concentric Spheres at Low Rayleigh Numbers," International Journal of Heat and Mass Transfer, 11, pp. 387-396, 1968.

5. Scanlan, J. A., Bishop, E. H., and Powe, R. E., "Natural Convection Heat Transfer between Concentric Spheres," International Journal of Heat and Mass Transfer, 13, pp. 1857-1872, 1970.

6. Weber, N., Powe, R. E., Bishop E. H., and Scanlan, J. A., "Heat Transfer by Natural Convection between Vertically Eccentric Spheres," submitted to Journal of Heat Transfer, Transactions of ASME, Series C.

7. Jakob, M., Heat Transfer, Vol. 1, John Wiley and Sons, Inc., New York, 1949.

8. Eckert, E. R. G., and Drake, R. M. Jr., Heat and Mass Transfer, McGraw-Hill Book Company, Inc., New York, 1959.

9. Gröber, H., Erk, S., and Grigull, Fundamentals of Heat Transfer, translated by Moszynski, J. R., McGraw-Hill Book Co., Inc., New York, 1961.

10. Chandra, K., "Instability of Fluids Heated from Below," Proceedings of the Royal Society of London, Series A, 164, pp. 231-242, 1938.

11. Schmidt, R. J., and Saunders, O. A., "On the Motion of A Fluid Heated from Below," Proceedings of the Royal Society of London,

Series A, 165, pp. 216-228, 1938.

12. Leontiev, A. I., and Kirdyashkin, A. G., "Experimental S dy of Flow Patterns and Temperature Fields in Horizontal Free Convection Liquid Layers," International Journal of Heat and Mass Transfer, 11, pp. 1461-1466, 1968.

13. Batchelor, G. K., "Heat Transfer by Free Convection across A Closed Cavity between Vertical Boundaries at Different Temperatures," Quarterly of Applied Mathematics, Vol. XII, pp. 209-233, 1954.

14. Elder, J. W., "Laminar Free Convection in a Vertical Slot," Journal of Fluid Mechanics, 23, Part 1, pp. 77-98, 1965.

15. Elder, J. W., "Numerical Experiments with Free Convection in A Vertical Slot," Journal of Fluid Mechanics, 24, Part 4, pp. 823-843, 1966.

16. Eckert, E. R. G., and Carlson, W. O., "Natural Convection in An Air Layer Enclosed Between Vertical Boundaries at Different Temperatures," International Journal of Heat and Mass Transfer, 2, pp. 106-120, 1961.

17. Wilkes, J. O., and Churchill, S. W., "The Finite-Difference Computation of Natural Convection in a Rectangular Enclosure," American Institute of Chemical Engineers Journal, 12, pp. 161-166, 1966.

18. Liu, C.Y., Mueller, W. K., and Landis, F., "Natural Convection Heat Transfer in Long Horizontal Cylindrical Annuli," International Developments in Heat Transfer, Part V, ASME, pp. 976-984, 1961.

19. Crawford, L., and Lemlich, R., "Natural Convection in Horizontal Concentric Cylindrical Annuli," I & EC Fundamentals, 1, pp. 260-264, 1962.

20. Grigull, U., and Hauf, W., "Natural Convection in Horizontal Cylindrical Annuli," paper 60 in Proceedings of the Third International Heat Transfer Conference, 2, AIChE, pp. 182-195, 1966.

21. Lis, J., "Experimental Investigation of Natural Convection Transfer in Simple and Obstructed Horizontal Annuli," paper 61 in Proceedings of Third International Heat Transfer Conference, 2,

AIChE, pp. 196-204, 1966.

22. Bishop, E. H., and Carley, C. T., "Photographic Studies of Natural Convection between Concentric Cylinders," Proceedings of the 1966 Heat Transfer and Fluid Mechanics Institute, Stanford University Press, pp. 63-78, 1966.

23. Mack, L. R., and Bishop, E. H., "Natural Convection between Horizontal Concentric Cylinders for Low Rayleigh Numbers," Quarterly Journal of Mechanics and Applied Mathematics, Vol. XXI, Part 2, pp. 223-241, 1968.

24. Bishop, E. H., Carley, C. T., and Powe, R. E., "Natural Convection Oscillatory Flow in Cylindrical Annuli," International Journal of Heat and Mass Transfer, 11, pp. 1741-1752, 1968.

25. Powe, R. E., Carley, C. T., and Bishop, E. H., "Free Convective Flow Patterns in Cylindrical Annuli," Journal of Heat Transfer, Transactions of ASME, Series C, 91, 3, pp. 310-314, 1969.

26. Powe, R. E., Carley, C. T., and Carruth, S., "A Numerical Solution for Natural Convection in Cylindrical Annuli," Journal of Heat Transfer, Transactions of ASME, 89, pp. 210-220, 1971.

27. Powe, R. E., "Natural Convective Flow in Horizontal Cylindrical Annuli," M.S. Thesis, Mississippi State University, State College, 1968.

28. Bishop, E. H., "Heat Transfer by Natural Convection between Isothermal Concentric Spheres," Ph.D. Dissertation, University of Texas, 1964.

29. Weber, N., "Natural Convection Heat Transfer between A Body and Its Spherical Enclosure," Ph.D. Dissertation, Montana State University, 1971.

30. Baker, D. J., "A Technique for the Precise Measurement of Small Fluid Velocities," Journal of Fluid Mechanics, 26, Part 3, pp. 573-576, 1966.

MONTANA STATE UNIVERSITY LIBRARIES
3 1762 10011696 9

D378
Y58
cop.2
Yin, Shiu-hau
Natural convective flow between isothermal concentric spheres

NAME AND ADDRESS
Lib. use
Richard K. Liu
S. Yin
Jan-in Wu

D378
Y58
cop. 2